Ministry of Higher Education and Scientific Research

وزارة التعليم العالي والبحث العلمي

Badji Mokhtar Annaba University

Faculty of Earth Sciences

Department of Geology.

جامعة باجي مختار – عنابـــة

كـليـة علوم الأ رض

قســم الجيولوجيا

Thesis

Presented to obtain the diploma of

Doctorate (LMD)

Discipline : Geology

Option : Geology

By:

LAOUAR khaled

Theme :

Petrological and geochemical study (major, trace and rare earth elements) of phosphorites from Bled El Hadba, Djebel Onk (NE Algeria)

Thesis defended on July 10th, 2025 before the jury composed of:

Fahima HALIMI	Assoc.Prof.	Badji Mokhtar University -Annaba	President
Rabah LAOUAR	Prof.	Badji Mokhtar University -Annaba	Supervisor
Mabrouk BOUGHDIRI	Prof.	Carthage University –Tunisia	Examiner
Smaine CHELLAT	Prof.	Mentouri Brothers University - constantine	Examiner
Mohamed TLILI	Assoc.Prof.	Badji Mokhtar University -Annaba	Examiner
Ouafi AMEUR-ZAIMECHE	Assoc.Prof.	Kasdi Merbah University -Ouargla	Examiner

الحمد لله وحده

"و ما توفيقي الا بالله"

"My success is only from God"

(The Holy Quran)

"However difficult life may seem, there is always something you can do and succeed at »

Stephen hawking

"Genius is one percent inspiration, ninety-.nine percent perspiration »

Thomas Alva Edison

To my parents

To my sisters.. to the memory of my brother

To the memory of all the martyrs of Algeria

To every free people in the whole world

Acknowledgements

I would like to express my profound gratitude to my supervisor, **Pr. Rabah Laouar**, for his unwavering support and invaluable guidance throughout the various challenges of my PhD journey. His willingness to share his time and extensive scientific expertise has been instrumental in my development. Thank you for your invaluable support in cultivating my academic and scientific character.

I wish to extend my heartfelt thanks to **Dr. Olivier Bruguier** of Géosciences Montpellier (France) for his generous hospitality at the ICP-MS laboratory. The advancement of this research would not have been achievable without his invaluable help and support. I appreciate his encouragement and the promotion of a scientific mindset.

I wish to extend my sincere thanks to **Pr. Delphine Bosch** for her support and the significant help she provided during my presence in the ICP-MS laboratory (Géosciences Montpellier – France).

With deep sincere feelings, I am so happy to express my gratitude to **Pr. Sihem Salmi-Laouar** for her insightful advice availability and the genuine interest she has shown in my work. Today, I extend my heartfelt thanks, as being her student continues to serve as an endless source of motivation, propelling me toward the completion of this thesis and further exploration in the realm of scientific research, which I hope reflects my deep appreciation.

My profound gratitude goes to **Pr. Rabah Kechiched** from the University of Ouargla for his invaluable support throughout all stages of this work. I am deeply appreciative of your guidance, encouragement, and contributions to the advancement of my scientific career.

I would like to express my sincere gratitude to **Pr. Ali Tlili** from the University of Sfax (Tunisia) for his assistance in conducting chemical and mineralogical analyses in the mineralogical laboratory, Faculty of Sciences, Sfax University.

I wish to acknowledge **Pr. Chouabbi Abdelmadjid** for his steadfast support and encouragement throughout my doctoral studies. His ongoing presence has been a significant source of assistance during this academic endeavor.

It is imperative that I take this opportunity to extend my heartfelt thanks to **Dr. Tourkia Tahri** of the University of Bejaia for her significant contributions at the Bir El Ater complex in Tebessa.

Appreciation is likewise directed towards **Mr. Djafar Alem** for his efforts in sample preparation and the fabrication of thin sections in addition of his encouragements.

A heartfelt appreciation is expressed to **Badji Mokhtar University - Annaba** for its funding of this training initiative. Special thanks go to the **responsables of Geology department - Annaba-** for their support in administrative tasks.

Gratitude is also expressed to the National Company of Iron and Phosphates **(FERPHOS)** for their cordial reception at the operational and processing facilities located in Bir-el-Ater.

I wish to acknowledge **Mr. Hamza Larit** for his invaluable help and encouragement, which I greatly appreciate as both a friend and a colleague. Furthermore, I would like to thank my colleague, **Ms. Ibtissam Diab**, for her help to contribute some analysis work.

I would like to express my sincere gratitude to the members of the jury who kindly agreed to evaluate this doctoral thesis. I extend my special thanks to: **Dr. Fahima Halimi** from Badji Mokhtar University –Annaba, for serving as the chair of the jury; **Pr. Rabah Laouar** from Badji Mokhtar University –Annaba, for acting as a reviewer and for providing valuable and

constructive feedback; **Pr. Mabrouk Boughdiri** from Carthage University –Tunisia, **Pr. Smaine Chellat** from Mentouri Brothers University –Constantine, **Dr. Mohamed Tlili** from Badji Mokhtar University –Annaba, and **Dr. Ouafi Ameur-Zaimeche** from Kasdi Merbah University –Ouargla, as examiners for their relevant questions and helpful advice. Their remarks and recommendations have greatly enriched this thesis, and I am truly greatful for their contributions.

I would like to express my sincere thanks to all the professors and researchers who have played a role, whether near or far, in the development of this work. This thesis represents the result of many years of education, and I am deeply grateful to all my professors in the Department of Geology at the University of Annaba. I acknowledge their contributions to the exceptional training I received throughout my undergraduate and postgraduate education.

I extend my profound gratitude to the cornerstone of my existence and achievements, **my parents**, for their unwavering presence and the myriad of gifts they have bestowed upon me throughout my life. Additionally, I offer heartfelt appreciation to **my sisters** and the extended **family**, especially **Toufik**, **Mohamed (loucif)** and **Ramda,** for their continuous support and encouragement, which have instilled hope within me.

Khaled LAOUAR

TABLE OF CONTENTS

CHAPTER III

PETROGRAPHY AND MINERALOGY OF THE BLED EL HADBA PHOSPHORITES

CHAPTER IV

GEOCHEMISTRY OF THE BLED EL HADBA PHOSPHORITES

CHAPTER V

DEPOSITIONAL ENVIRONMENT AND REDOX CONDITIONS

CHAPTER VI

RARE EARTH ELEMENTS ECONOMY

ABSTRACT

The phosphorite deposits located in Algeria are found within the Eastern Saharan Atlas, particularly in the Tebessa area. A notable feature of these deposits is the Djebel Onk phosphorite complex, which is situated in the southern section of the Tebessa region. Additionally, the Bled El Hadba deposit is part of the extensive Djebel Onk phosphorite complex in northeastern Algeria. This deposit has been the focus of numerous geological investigations aimed at analyzing P_2O_5 concentrations for commercial viability.

Recent discussions among various authors have highlighted the enrichment of rare earth elements (REE) in Algerian phosphorites, which are regarded as some of the most abundant Paleocene-Eocene phosphorites globally. The upper Thanetian phosphorite layer measures approximately 30 meters in thickness and is categorized into three distinct sub-layers—lower, main, and upper—according to their P_2O_5 concentrations, with the main sub-layer identified as the most affluent. Nevertheless, there has been a scarcity of comprehensive geochemical studies conducted on this deposit to date.

This study involved the analysis of major, trace, and rare earth elements (REE) in phosphate particles, including pellets, coprolites, and glauconites, utilizing 'in situ' (LA-ICP MS). Whole-rock samples were analyzed using X-ray fluorescence (XRF) techniques. The findings indicate that the primary sub-layer exhibits the highest concentrations of whole-rock P_2O_5, ranging from 19.65 to 21.32 wt%, in contrast to the lower sub-layer (10.47–16.87 wt%) and the upper sub-layer (9.43–13.87 wt%). Among the phosphate particles, glauconites possess the lowest P_2O_5 levels across all three sub-layers (17.45–19.35 wt%), while pellets (21.14–24.33 wt%) and coprolites (21.75–24.12 wt%) show higher values. Additionally, glauconites contain significantly greater amounts of Al_2O_3, SiO_2, MgO, and Fe_2O_3(t). The ΣREE concentrations in glauconites (764–2050 ppm) surpass those found in pellets (221–910 ppm) and coprolites (214–909 ppm). Notably, within glauconite particles, the ΣREE, along with Al_2O_3, SiO_2, MgO, and Fe_2O_3(t), increases from the core to the rim, while P_2O_5 levels decline, indicating that glauconitization occurs after phosphatization. Furthermore, the glauconitization process intensifies from the lower to the upper sub-layer, as evidenced by positive correlations between Al_2O_3 and both MgO and SiO_2, alongside negative correlations between Al_2O_3 and P_2O_5. The anomalies of Ce, Eu, and Y, in conjunction with La/Nd ratios and Nd concentrations, suggest that phosphatization occurred under oxic conditions due to warm water upwelling, whereas

glauconitization initiated under more reduced (suboxic) conditions, particularly during early diagenesis, characterized by peak REE uptake from porewater and slow sedimentation rates.

Although the P_2O_5 concentrations in the Bled El Hadba phosphate particles are comparatively low, their ΣREE contents represent the highest levels found among all phosphorites in Algeria and North Africa. Consequently, it is advisable to conduct more comprehensive analyses of rare earth elements to thoroughly assess its economic viability concerning critical raw materials.

Keywords: Phosphorite; Pellet; Glauconite; Rare earth elements; Bled El Hadba; Tebessa

R É S U M É

Les gisements de phosphate en Algérie sont situés dans l'Atlas saharien oriental, plus précisément dans la région de Tebessa. Parmi ces gisements, on trouve l'important complexe de phosphate de Djebel Onk dans la partie sud de la région de Tebessa. Le gisement de Bled El Hadba appartient au grang complexe de Djebel Onk, dans le nord-est de l'Algérie. Le gisement a fait l'objet de nombreuses études géologiques axées sur les teneurs en P_2O_5 à des fins commerciales.

L'enrichissement en éléments de terres rares (ETR) des phosphates algériens a été évoqué récemment par un certain nombre d'auteurs et ces phosphates sont désormais considérées comme les plus riches du Paléocène-Éocène dans le monde. La couche de phosphorite du Thanétien supérieur a une épaisseur d'environ 30 m et se subdivise en trois sous-couches (sous-couche inférieure, principale et supérieure), sur la base des teneurs en P_2O_5, la sous-couche principale étant considérée comme la plus riche. Malgré cela, peu d'études géochimiques détaillées ont été menées sur ce gisement jusqu'à présent.

Dans ce travail, des analyses des éléments majeurs, traces et terres rares ont été effectuées sur des particules phosphatées (pastilles, coprolithes et glauconites) à l'aide de la technique LA-ICP MS *in situ*, et sur des échantillons de roches totales à l'aide de la technique XRF. Les résultats montrent que la sous-couche principale présente les teneurs en P_2O_5 les plus élevées de la roche totale, variant entre 19,65 et 21,32 % en poids par rapport aux sous-couches inférieure (10,47-16,87 % en poids) et supérieure (9,43-13,87 % en poids). Parmi les particules phosphatées, les glauconites présentent les plus faibles teneurs en P_2O_5 dans les trois sous-couches (17,45-19,35 % en poids) par rapport aux pellets (21,14-24,33 % en poids) et aux coprolithes (21,75-24,12 % en poids), et en grande partie les teneurs les plus élevées en Al_2O_3, SiO_2, MgO et $Fe_2O_{3(t)}$. Les glauconites présentent également des teneurs en ΣREE plus élevées (764-2050 ppm) que les pellets (221-910 ppm) et les coprolithes (214-909 ppm). Dans les glauconites, les ΣREE, ainsi que les teneurs en Al_2O_3, SiO_2, MgO et $Fe_2O_{3(t)}$, augmentent du cœur au bord, tandis que les teneurs en P_2O_5 diminuent, ce qui suggère que la glauconitisation est postérieure aux processus de phosphatisation. De plus, le processus de glauconitisation augmente de la sous-couche inférieure à la sous-couche supérieure, comme le montrent les corrélations positives entre les teneurs en Al_2O_3 et celles de MgO et SiO_2 d'une part, et les corrélations négatives entre Al_2O_3 et P_2O_5 d'autre part. Les anomalies du Ce, Eu et Y, ainsi que les rapports La/Nd et les teneurs en Nd, indiquent tous une phosphatisation dans des conditions

oxiques à la suite d'une remontée de courants chauds, tandis que la glauconitisation a commencé dans des conditions plus réduites (suboxiques), c'est-à-dire au début de la diagenèse, un taux d'absorption des terres rares le plus élevé de l'eau interstitielle, et à des taux de sédimentation lents.

Malgré leurs concentrations relativement faibles en P_2O_5, les teneurs en ΣREE des particules phosphatées de Bled El Hadba enregistrent les concentrations les plus élevées de tous les phosphates algériens et nord-africains. La sous-couche principale est considérée comme la plus riche en glauconite en Algérie. Par conséquent, des analyses plus approfondies des terres rares sont recommandées pour mieux évaluer son potentiel économique en termes de matières premières essentielles.

Mots clés : Phosphorite ; Pellet ; Glauconite ; Éléments des terres rares ; Bled El Hadba ; Tebessa

ملخص

تقع رواسب الفوسفات في الجزائر في الأطلس الصحراوي الشرقي، وتحديداً في منطقة تبسة. ومن بين هذه الرواسب، يبرز مجمع فوسفات جبل العنق الواقع في الجزء الجنوبي من منطقة تبسة. وعلى وجه الخصوص، تعتبر رواسب فوسفات بلاد الحدبة جزءًا مهمًا من منطقة جبل العنق. بينما ركزت الأبحاث السابقة بشكل رئيسي على الجوانب الجيولوجية والترسيبية و كذا التعدينية الخاصة بعنصر الفوسفور لهذه الرواسب، فإن الدراسات الجيوكيميائية نادرة. وبالتالي، تهدف هذه الدراسة إلى استكشاف الخصائص الجيوكيميائية لفوسفات بلاد الحدبة بالاضافة إلى الجوانب الجيولوجية والبترولوجية. يتميّز فوسفات بلاد الحدبة بطبقة فوسفاتية يبلغ سمكها حوالي 30 متراً. تنقسم هذه الطبقة إلى ثلاث طبقات فرعية: الطبقة الفرعية القاعدية، والطبقة الفرعية الرئيسية، والطبقة الفرعية العليا. تحتوي هذه الطبقات الفوسفاتية على حبيبات مستديرة بشكل جيد من البيليت والكوبرولايت البرازي والغلوكونايت المخضر. هذه الجسيمات تكون عموما مدعمة بواسطة الأسمنت الدولوميتي أو الكالسيتي أو الطيني. يكشف التحليل الجيوكيميائي أن الطبقة الفرعية الرئيسية تحتوي على أعلى محتوى من P_2O_5 متجاوزة الطبقتين الفرعيتين القاعدية والعلوية. ومن ناحية أخرى، تحتوي الغلوكونايت في الطبقات الفرعية الثلاث على أقل محتوى من P_2O_5 مقارنة بالبيليت والكوبرولايت. و في المقابل، تحتوي الغلوكونايت على نسبة ΣETR أعلى مما هي في البيليت والكوبرولايت. تشير الدراسة الجيوكيميائية لبعض العناصر الاساسية، بالإضافة إلى العناصر الأرضية النادرة خاصة شذوذات Ce و Eu و Y, و كذا بعض العناصر الأثرية، إلى أن العملية الفوسفاتية حدثت في بيئات متوسطة الأكسدة الى مؤكسدة بسبب ارتفاع المياه الساخنة، في حين أن العملية الغلوكونايتية بدأت في ظروف ضعيفة الأكسدة الى متوسطة الارجاع.

على الرغم من تركيزات P_2O_5 المنخفضة نسبيًا، إلا أن مجمل محتويات ΣETR لجزيئات الفوسفات (بيليت. كوبرولايت و غلوكونايت) ببلاد الحدبة تسجل أعلى تركيزات من جميع الفوسفات الجزائري والشمال إفريقي. وبالتالي، يوصى بإجراء المزيد من التحاليل المتعمقة و التي تستهدف العناصر الأرضية النادرة من أجل تقييم أفضل و دقيق لإمكاناته الاقتصادية.

الكلمات المفتاحية: فوسفات ، بيليت ، غلوكونايت ، عناصر أرضية نادرة ، بلاد الحدبة ، تبسة.

INTRODUCTION

INTRODUCTION

Phosphorus is a vital element for life, serving as a fundamental building block of DNA, RNA, and ATP. It plays an indispensable role in the growth and development of living organisms. In addition, Phosphorites, which serve as the primary reservoir of phosphorus, play a pivotal role in the production of fertilizers, thereby contributing significantly to global agricultural productivity. The global food security is inextricably linked to the accessibility of phosphate, a non-renewable natural resource (Glenn et al., 1994). The forthcoming period will see an imminent deficit in the production of phosphate, which is being driven by the significant demand that can be attributed to population growth (Cooper et al., 2011).

Phosphorites, more commonly designated phosphate rock, constitute a foundational geological asset, performing a pivotal role in global nutrient cycles and agricultural sustainability. These sedimentary rocks, which are rich in phosphorus-bearing minerals, have gained increasing prominence due to their significance across a range of disciplines, including agriculture, environmental science, and paleoclimatology.

The economic and academic importance of sedimentary phosphates has long been a subject of interest for researchers (El Bamiki, 2020). An in-depth understanding of the geological processes that determine the formation of phosphorite is essential to optimize the extraction of these resources and to ensure the implementation of sustainable agricultural practices.

Significant advancements in the field of geochemistry have led to a general consensus on the phenomenon of phosphogenesis, which encompasses a range of biogeochemical processes (Glenn et al., 1994; Jarvis et al., 1994; Krajewski et al., 1994; Föllmi, 1996; Diaz et al., 2008). As a consequence, there have been developments in research indicating that phosphogenesis can occur in a variety of sedimentary environments (Filippelli, 2011).

The substantial accumulations of phosphorites throughout Earth's history were primarily formed during the Upper Cretaceous-Paleogene period (Notholt, 1985; Pufahl & Groat, 2017), particularly within the Tethyan phosphogenic province (Notholt, 1985). This province displays a broad geographical distribution, with occurrences reported across regions including the Middle East, North Africa, the Caribbean, and Central America. In North Africa, phosphorites are concentrated primarily in Algeria and Tunisia, with Morocco exhibiting the most substantial phosphorite reserves.

The phosphorite deposits in Algeria are situated in the Tebessa region, which is located within the Eastern Saharan Atlas. The southern portion of this region, specifically the Djebel Onk area, is the location of the primary phosphorite deposits, including Djebel Onk North, Kef Essenoun, Djemi Djema, Bled El Hadba and Oued Betita. Previous studies on these phosphorites have mainly concentrated on their geological and sedimentological characteristics (e.g., Visse, 1952; Chabou-Mostefai, 1987), mining (e.g., Benabdeslam et al., 2018; Bezzi et al., 2001, 2008 and 2012), and environmental aims (e.g., Boumaza et al., 2021; Benarous et al., 2022; Boumala et al., 2018; Lakehal et al., 2010). However, recent years have witnessed a shift in the field of geochemistry, with the emergence of several new studies (e.g., Kechiched et al., 2016, 2018, and 2020; Ferhaoui et al., 2022, Kechiched et al., 2024; Diab et al., 2024) focusing on phosphatic sites in both the northern (Tazbant, Dyr and El Kouif deposits) and southern (Kef Essenoun deposit) basins of the Tebessa region. The results of these studies have yielded significant geochemical data, particularly with regard to trace and rare earth elements. These data have provided new insights into the composition and characteristics of these phosphorite deposits.

This study aims to conduct a comprehensive petrological and geochemical analysis of phosphorite samples from Bled El Hedba, Djebel Onk deposit in northeastern Algeria. The investigation focuses on characterizing the major, trace, and rare earth element (REE)

compositions to better understand the mineralogical features, textural characteristics, and geochemical signatures of the phosphorites. Additionally, the study seeks to elucidate the paleoenvironmental conditions and mechanisms involved in the formation and accumulation of these phosphorite facies, providing new insights into their origin and geological evolution.

In order to simplify the exposition of the outcomes of this examination, the following textual organization is employed:

- Introduction to the present study framework.
- The 1st chapter gives the basic knowledge and general information about global and local phosphorites.
- The 2nd chapter presents the geological framework of the study area.
- The 3rd chapter presents the petrographic and mineralogical composition of the facies.
- The 4th chapter goes deep inside the chemical composition using major, trace and rare earth element studies.
- The 5th chapter investigates the depositional environment and redox conditions of the phosphorite formation.
- The 6th chapter concerns the economical task.
- An overall conclusion is given at the end of the manuscript.

CHAPTER I

AN OVERVIEW ON PHOSPHORITES

CHAPTER I

AN OVERVIEW ON PHOSPHORITES

A phosphate is a compound derived from phosphoric acid H_3PO_4 by the loss or substitution of one or more hydrogen atoms with other atoms or functional groups. In mineral chemistry, it is a salt resulting from the reaction of a base with this acid, or the anion forming part of this salt. Orthophosphate ions are the most common chemical forms of phosphate in the environment ($H_2PO_4^-$, HPO_4^{2-}, PO_4^{3-}), all derived from phosphoric acid by the loss of one to three hydrogen atoms. In organic chemistry, a phosphate is a type of organophosphorus compound; the substituent groups for the hydrogens of phosphoric acid can then be carbon chains, and they are sometimes referred to as organic phosphates. In geology, it is a rock formed from phosphatic minerals, either amorphous or cryptocrystalline (collophanite), or finely crystalline (apatite). Theses minerals occur as grains, coatings on organic skeletal fragments, finely crystalline layers cementing various debris, or as concretionary nodules.

I.1. Phosphorite chemistry:

The apatites are characterized by the general formula $Me_{10}(XO_4)_6Y_2$ (Bechade, 2008). This formula maintains stoichiometry, with the Me, XO4, and Y sites within the structure consistently occupied. Typically, Me signifies a divalent cation, XO4 denotes a trivalent molecular anion, and Y represents a monovalent anion. The most common apatite is fluorapatite [$Ca_{10}(PO_4)_6F_2$].

Phosphates found in sedimentary deposits are cryptocrystalline (Slansky, 1980). Corresponding minerals are also closely related to fluorapatite. Indeed, due to the relatively flexible structure of apatite, it can accommodate numerous ion substitutions across its three sites. Table 1 illustrates some of the various possible substitutions.

Table. 1: Examples of main substitutions within apatite structure (Banu, 2005).

Me^{2+}				XO_4^{3-}			Y^-		
Ca^{2+}	Sr^{2+}		Cd^{2+}	PO_4^{3-}	SiO_4^{4-}	AsO_4^{3-}	OH^-	F^-	Cl^-
Mg^{2+}	Ba^{2+}		Pb^{2+}	SO_4	MnO_4	VO_4^{3-}	Br^-	I^-	
Cu^{2+}	Zn^{2+}			CrO_4^{3-}	CO_3^{2-}	HPO_4^{2-}	S^{2-}	O^{2-}	CO_3^{2-}
Na^+	K^+	U^{4+}	Eu^{3+}						

There are two types of possible substitutions (Chaïrat, 2005):

• Substitutions of ions with the same charge but different sizes on the Me, XO_4, and Y sites of the apatite structure. These apatites remain stoichiometric, with only a slight deformation of the crystal lattice observed.

• Substitutions involving ions of different charges and sizes that require charge compensation to maintain the electroneutrality of the crystal lattice.

The most prominent substitution observed in sedimentary apatites involves the replacement of PO_4^{3-} with CO_3^{2-}. The addition of extra F^- ions aids in maintaining the crystal's electrical neutrality (Slansky, 1980). The prevalent mineral is carbonate-fluorapatite, also known as francolite, which can be represented by the simplified structural formula: $Ca_{10}[(PO_4)_{6-x}(CO_3F)_x]F_2$. This mineral crystallizes within the hexagonal system. There is potential significance in substitutions by Na, Mg, and OH as suggested by Lehr et al (1967) for sedimentary apatites. They proposed a general structural formula: $(Ca, Na, Mg)_{10}(PO_4)_{6-x}(CO_3)_x F_y (F,OH)$

The main major elements usually found in phosphorites are: P_2O_5, MgO, CaO, SiO_2, Al_2O_3, Fe_2O_3, TiO_2, Na_2O, K_2O and MnO. These elements are linked to key mineral phases like apatite, clays, carbonates, silica, etc. (Chabou Mostefai, 1987; Larouci, 1988).

Similarly, a range of trace elements concentrates within clay and phosphate phases, namely:

- Ba, Cr, Cs, Cu, Ga, Mo, Nb, Ni, Pb, Rb, Sb, Sn, Sc, Sr, V, Zn, and Zr (in clays);

- REEs, U, Y, and Sr (in apatites).

I.2. Phosphorite mineralogy:

Natural phosphates comprise over 200 mineral species (Fisher, 1973). However, the most abundant ones belong to the apatite family (Raguin, 1961). The phosphate mineral in a primary environment can exist in various forms (Straaten, 2002; Abu-Eishah et al., 1991), including:

• **Fluorapatite:** ($Ca_{10}(PO_4)_6F_2$): Predominantly found in igneous rocks and metamorphic settings, such as carbonatites and mica-pyroxenites.

• **Hydroxyapatite:** ($Ca_{10}(PO_4)_6(OH)_2$): Also present in igneous and metamorphic rocks and biogenic deposits.

• **Carbonated hydroxyapatite:** ($Ca_{10}(PO_4,CO_3)_6(OH)_2$): Mainly found in islands and caves.

• **Francolite:** ($Ca_{10-x-y}Na_xMg_y(PO_4)_{6-z}(CO_3)_zF_{0.4z}F_2$): This substituted carbonate-apatite complex is exclusively located in marine environments.

• **Dahllite:** ($3Ca_3(PO_4)_2CaCO_3$): This phosphate structure forms in marine sediments.

• **Collophane:** ($3Ca_3(PO_4)_{2n}Ca(CO_3,F_2,O)_xH_2O$): This is the typical mineral found in marine phosphate sediments.

There are also other phosphatic minerals resulting from the alteration of Ca phosphate deposits. Among these are:

• **Millisites:** (Na-K) $CaAl_6$ $(PO_4)_4$ $(OH)_9$ $3H_2O$.

• **Crandallites:** Ca_2Al6 $(PO_4)_4$ $(OH)_{10}$ $2H_2O$.

• **Augelites:** $Al_2(PO_4)$ $(OH)_3$.

• **Wavellites:** $Al_3(PO_4)_2\ (OH)_3\ 5H_2O$.

• **Turquoises:** $CuAl_6\ (PO_4)_4\ (OH)_8\ 4H_2O$.

• **Autunite:** $Ca\ (UO_2)_2(PO_4)_2\ 10\text{-}12H_2O$.

• **Meta-autunite:** $Ca\ (UO_2)_2(PO_4)_2\ 2\text{-}6H_2O$.

Capdecomme (1952) conducted a study on minerals in the Thiès region of Senegal, revealing that millisites, crandallites, and augelites are the most prevalent. Wavellites and particularly turquoises, however, are the rarest among them. These minerals exhibit diverse chemical compositions, deviating from their theoretical composition due to the inclusion of F and notable concentrations of Sr, Ba, or Fe. Vivianite $Fe_3(PO_4)_2\ 8H_2O$ might also manifest in such altered profiles, commonly found in lacustrine or alluvial deposits.

On limestone rocks, calcium phosphates such as monetite ($HCaPO_4$) or whitlockite $Ca_3(PO_4)_2$ form, alongside apatitic minerals that are typically low in fluorine content. Moreover, alumino-calcium phosphates like crandallite or Fe and Al phosphates (Slansky, 1980) can develop on calcareous rocks.

Sedimentary deposits host various other phosphate minerals, as noted by Fisher (1973). For instance, monazite, a rare earth phosphate, is notably present in the Ordovician formations of Brittany (Slansky, 1980) and in a number of acidic igneous rocks. Autunite or meta-autunite is secondary mineral originating from specific uranium-rich phosphate deposits.

The majority of sedimentary phosphate minerals belong to the apatite family, which crystallizes in the hexagonal system. Its unit cell forms a prism with a hexagonal base and falls within the space group P63/m (Montel et al., 1980). The structure of apatite is defined by XO_4 (PO_4) tetrahedra, constituting its framework. Interestingly, unlike the Me (Ca) or Y (F) sites, no voids or gaps have been observed at the XO_4 sites (Lacout, 1983).

Fluorapatite, represented by the chemical formula $Ca_{10}(PO_4)_6F_2$ and crystallographic parameters of a = 9.375 Å and c = 6.875 Å, is commonly utilized as a reference point (Elliott,

1994). In Figure 1, The structural projection of fluoroapatite, $Ca_{10}(PO_4)_6F_2$, onto the (001) plane, is depicted. The close-knit arrangement of XO_4^{3-} groups unveils two distinct tunnel types within the crystal lattice:

- The initial type, termed type I, accommodates four Me cations known as Me(I), possessing a diameter of 2.5 Å in fluorapatite. These Me(I) cations are positioned along a ternary axis within the structure, displaying C_3 site symmetry. Surrounding each cation are nine oxygen atoms (Fig. 2).
- The second tunnel, labeled as II, measures between 3 and 4.5 Å in diameter within fluorapatite. This tunnel accommodates a set of six Me(II) cations with Cs symmetry. Positioned around the tunnel's periphery, these Me(II) cations form equilateral triangles, staggered by 60° and situated at the ¼ and ¾ positions along the axis displaying 6-helical symmetry (the c-axis of the hexagonal lattice). Each Me(II) cation interacts with seven atoms: six oxygen atoms and one fluorine atom (Fig. 3). The tunnel's diameter allows a degree of mobility and facilitates various exchanges (as noted by Samec, 1965, and Wright, 1969).

Y- anions occupy different positions along the axis defined by the Me(II), varying based on their nature, and enjoy significant mobility within the structure. A visual depiction of this tunnel is presented specifically for fluorapatite (Fig. 4). The reported mesh parameters in literature exhibit considerable variability, yet the most accurate findings specify a=9.3684 Å and c=6.8841 Å, resulting in a mesh volume of V=523.25 $Å^3$. This corresponds to a calculated density of 3.201, aligning well with the measured density (d=3.15).

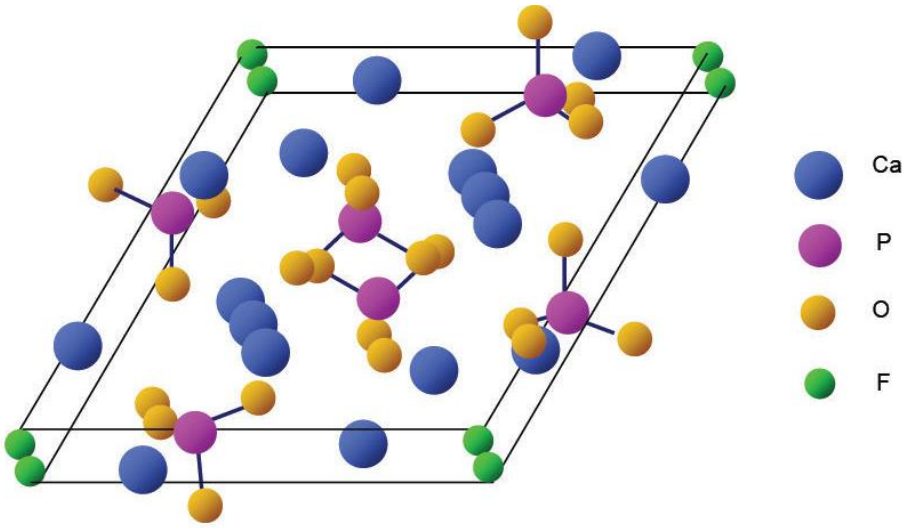

Fig. 1: The representation of the hexagonal mesh base plane projection for apatite $Ca_{10}(PO_4)_6F_2$ (After Bertholus and Defranceschi, 2004).

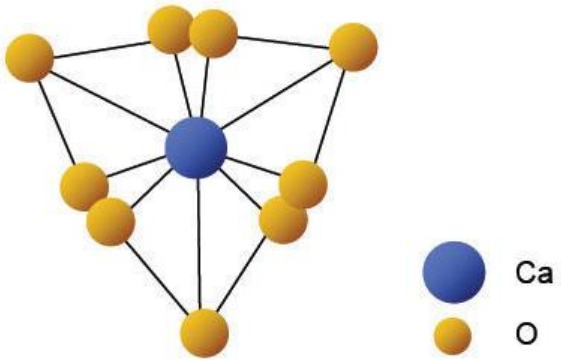

Fig. 2: Environment of calcium atoms of type I sites in non- substituted fluorapatite (After Bertholus and Defranceschi, 2004)

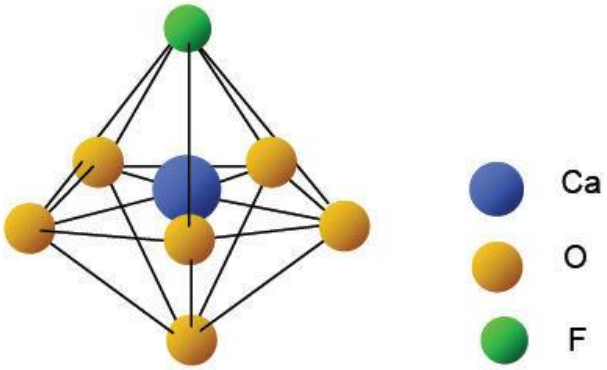

Fig. 3: Environment of calcium atoms of type II sites in non- substituted fluorapatite (After Bertholus and Defranceschi, 2004)

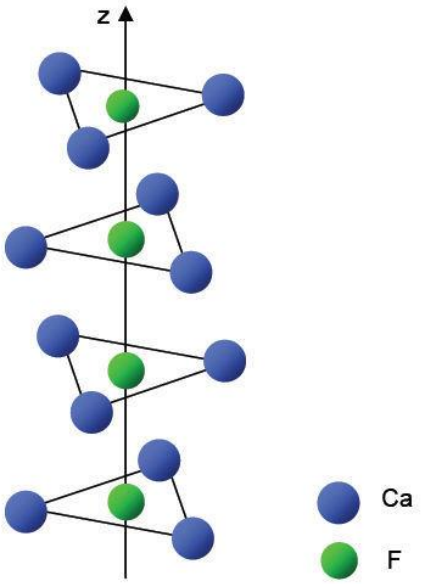

Fig. 4: The arrangement of fluorine atoms in fluorapatite
(After Bertholus and Defranceschi, 2004)

I.3. Origin of phosphorites:

In general, calcium phosphate is found in magmatic rocks and in sedimentary rocks of various ages. We can conclude the origin of its deposits as follows:

I.3.1. Deposits of igneous origin:

This type of deposit is primarily associated with alkaline intrusive complexes. The most common rocks are nepheline syenites, carbonatites, and pyroxenites. These deposits are less numerous and often less rich and smaller in size compared to sedimentary deposits. The Khibiny deposit (USSR), associated with a ring complex of nepheline syenite, represents one of the main deposits of this type (Slansky, 1980). Other deposits of apatite-bearing carbonatites can be found in Canada, Jacupiranga in Brazil, Siilinjärvi in Finland, and Phalaborwa in South Africa.

Fig. 5: The main quarry of Koashva magmatic phosphate deposit (Khibiny Massif – RUSSIA).

I.3.2. Deposits of sedimentary origin:

The most remarkable platform deposits are associated with synclines. They form under an arid climate. The sedimentary facies are primarily of three types: granules or pseudo-ooliths, nodules, and organic debris (coprolites and phosphatized fossils). Sedimentary deposits are more numerous and larger in volume (Smirnov, 1982). The grades in these places are often over 20% and can even reach 30% in P_2O_5 content. The Djebel Onk deposits are among this type, with resources that can reach 2 billion tons within the Djebel Onk basin (kechiched, 2011).

Fig. 6: Kef Essenoun quarry (Djebel Onk region –Algeria).

I.3.3. Deposits of Guano type:

Guano, an organic substance formed through the natural breakdown of seabird waste and bat prey remnants, undergoes a transformative process when acidic droppings settle on limestone-rich soils. Over years and decades, these deposits evolve into a fine-grained amalgamation of phosphatic and nitrated minerals known as guano. This substance is notably prevalent across various Pacific islands, where it accumulates, sometimes reaching thicknesses of several meters. Aside from its mineral composition, guano serves as a historical habitat for seabirds, providing nesting grounds where they lay their eggs. An example is the Cape penguin, which has utilized guano for this purpose.

Among these islands, the Ballestas Islands stand out, with the neighboring Chincha Islands about ten kilometers north, as the most renowned locations for guano in Peru.

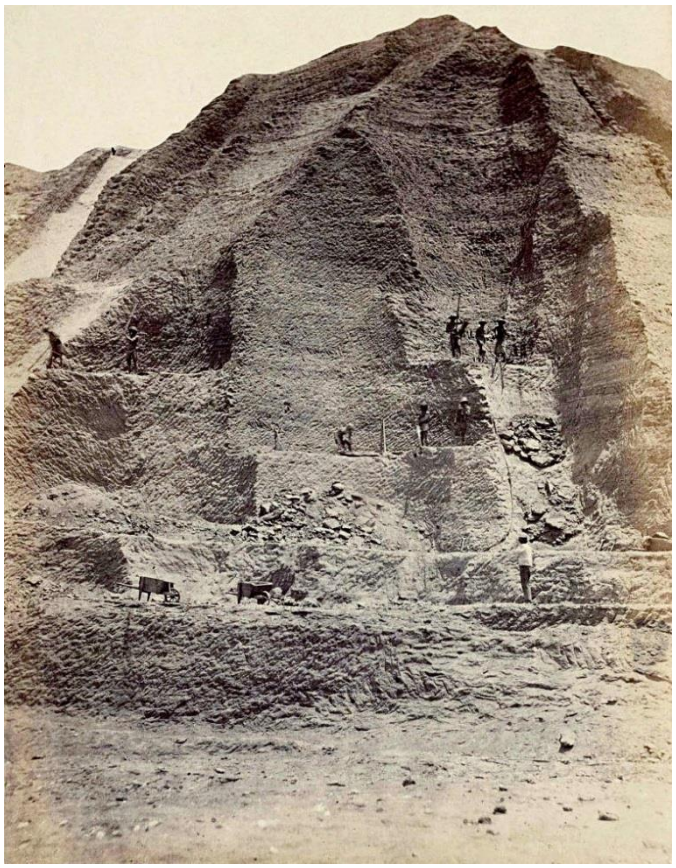

Fig. 7: Deposit of guano-type in Chincha islands (Peru).

I.4. Mechanism of sedimentary phosphogenesis:

One of the most plausible hypotheses, proposed by Kazakov in 1930, stems from oceanographic research findings. These studies revealed a notable trend: the P_2O_5 content in seawater rises as depth increases. The lowest concentrations are found in the photosynthesis-rich zone, where phosphorus gets consumed, while the highest concentrations occur around 500 meters deep.

Phosphorus undergoes chemical precipitation along the edges of the continental shelf, transported there by upward cold currents (upwelling) (Fig. 8). As the water warms, pH levels rise while the partial pressure of CO_2 drops. This shift prompts the precipitation of $CaCO_3$, followed by phosphates. Consequently, chemical phosphate sedimentation doesn't occur in deep areas, where CO_2 pressure is too high, nor in the photosynthesis zone where phosphorus is utilized. The range of around 50 to 500 meters emerges as the zone where phosphate precipitation predominantly occurs. This theory was later refined by Visse in 1952, who suggested a distinction between the genesis and accumulation environments (kechiched, 2011).

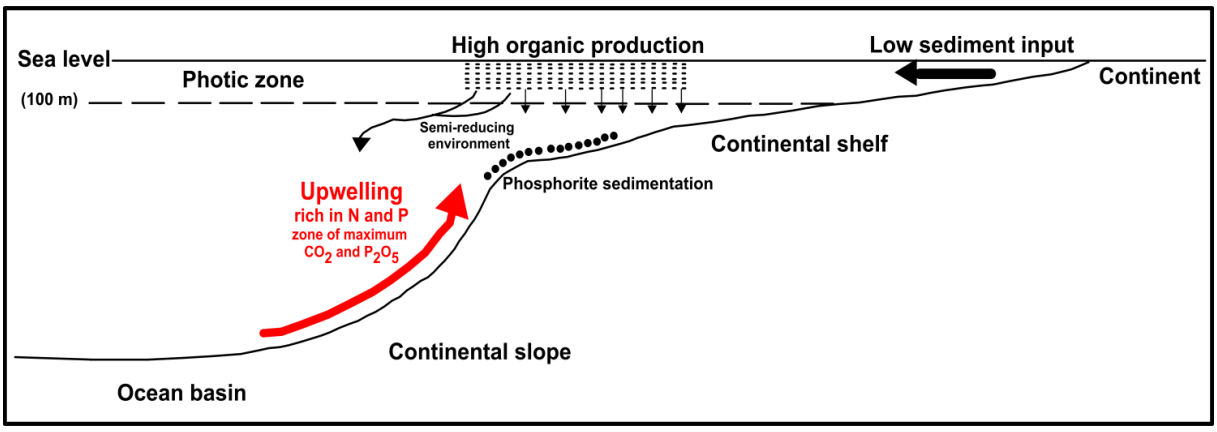

Fig. 8: Kazakov model of phosphogenesis (1930)

These deposits manifest in two primary types:

- Continental shelf deposits: characterized by light coloration, nodular or pseudo-oolithic structures, frequent association with glauconite, and various quartzose detrital elements. These deposits seem to correlate with transgressions (Kechiched, 2011).

- Borderline geosynclinal deposits: These yield darker-colored ores with a pseudo-oolithic structure, generally accompanied by clayey exogangue and significant siliceous formations. This type of deposit is suggestive of a more regressive context (Kechiched, 2011).

I.5. Distribution of sedimentary phosphorites around the world:

I.5.1. On horizontal (geographic) scale:

The largest phosphate deposits belong to the South Tethyan phosphogenic province, which extends from North Africa to the Middle East over approximately 5500 km (Notholt, 1985) (fig. 9) and represents more than 85% of the known phosphate reserves in the world (Jasinski, 2020). The primary phosphate accumulations worldwide developed in low-latitude regions, approximately 10° to 20° (Cook & McElhinny, 1979). Presently, active phosphate deposits are concentrated along continental margins within subtropical areas of lower latitudes (Baturin, 1982). These areas with upwelling phenomena are chiefly found along the west coast of Africa, the east coast of the United States, and offshore regions of California, Peru, and Chile (El Bamiki, 2020). Plate tectonics significantly influenced the formation of substantial phosphate reserves by shifting favorable margin zones for phosphogenesis toward lower latitudes, ensuring sustained phosphate productivity (Cook & McElhinny, 1979).

I.5.2. On vertical (time) scale:

The phosphorites existence is known along the geological scale from the Precambrian to the Cenozoic eras (Cook, 1984) (fig. 10). The oldest phosphate deposits preserved in Earth's geological history are found in the Precambrian era, notable examples being the Zaonega formation in Russia (Joosu et al., 2015) and the Sete Lagoas formation in Brazil (Drummond et

al., 2015). This era coincided with a significant oxygenation event in the Earth's atmosphere known as the Great Oxidation Event (Holland, 2006). This pivotal moment in Earth's timeline marked the onset of sedimentary phosphate formation, triggered by the chemical alteration of phosphorus-rich igneous rocks and the subsequent enrichment of the oceans (Glenn et al., 1994; Papineau, 2010; Pufahl & Hiatt, 2012).

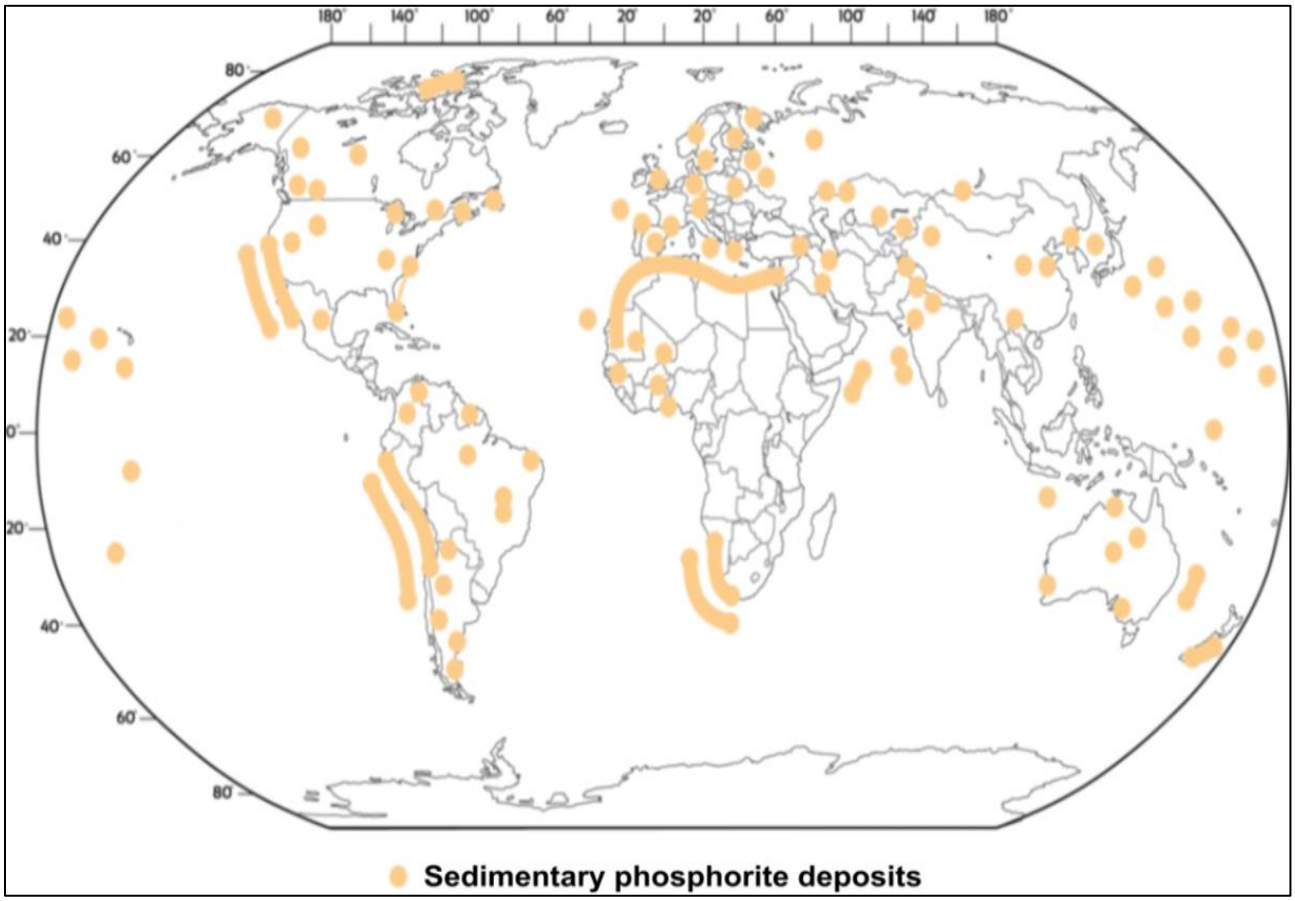

Fig. 9: The spatial distribution of sedimentary phosphate deposits worldwide (Pufahl & Groat, 2017)

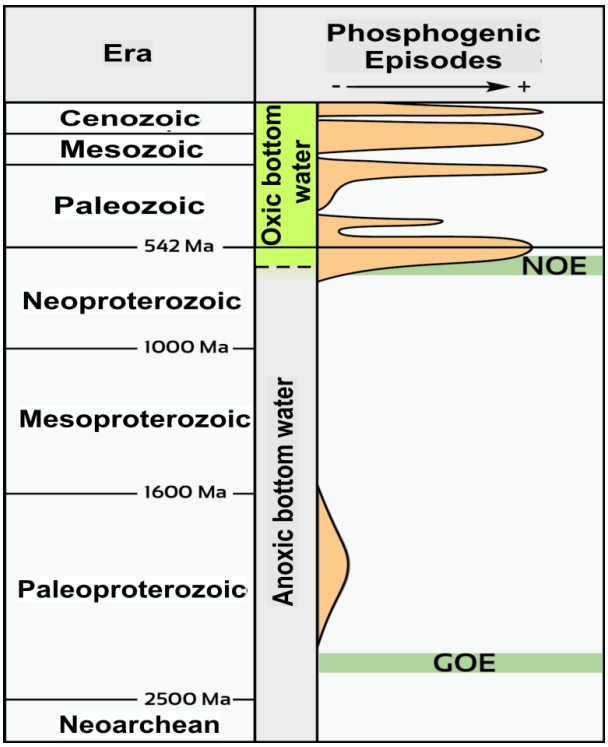

Fig. 10: Temporal distribution of the main phosphogenic events in earth's history (Pufahl & Groat, 2017)

GOE = Great Oxidation Event, **NOE** =Neoproterozoic Oxygenation Event.

I.6. World's phosphorite production and reserves:

Sedimentary deposits contribute between 80% to 90% of the world's production, while igneous rock deposits account for 10% to 20% (FAO, 2004). Global phosphate production capacity rose from 218 million tons in 2014 to 263 million tons in 2017, dipping to 240 million tons in 2019. Leading producers include China with 110 million tons, the United States with 23 million tons, and Morocco and Western Sahara with 36 million tons. These nations collectively yield about three-quarters of the world's total production. Russia (14 million tons) and Jordan (8 million tons) also significantly contribute to the global output (Fig.11).

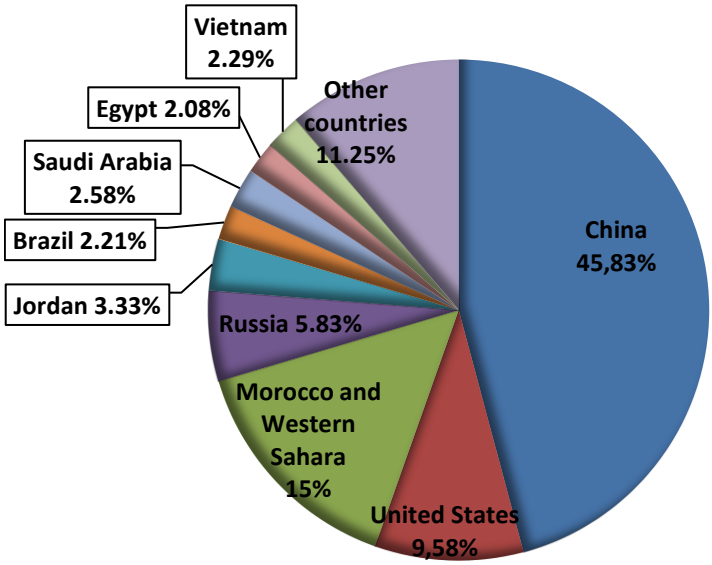

Fig. 11: The worldwide production of phosphate rock in 2018, out of a total of 240 million tons (Data sourced from USGS, 2020).

As per the USGS (2020) data, the primary reserve of phosphorite rock worldwide is concentrated in Morocco and Western Sahara, accounting for over 70% (50 billion tons), while China holds the second position with approximately 5% (3.2 billion tons) (Fig. 12).

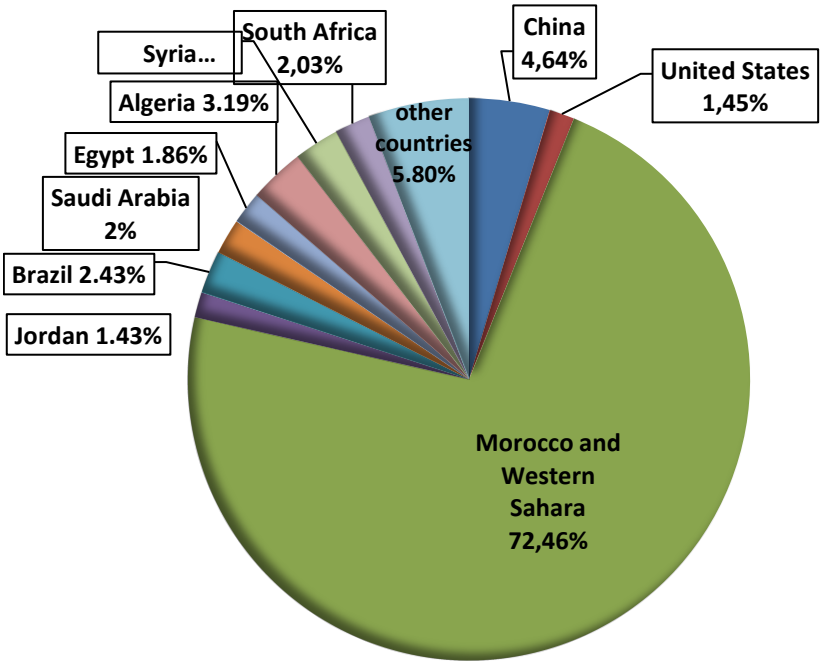

Fig. 12: "Global phosphate rock reserves for 2018.
(Data sourced from USGS, 2020)

I.7. Phosphorite uses:

Phosphorites, which are sedimentary rocks containing high level of phosphate minerals, have several uses:

- **Fertilizers production:**

Phosphorites are a primary source of phosphorus used in the production of fertilizers. Phosphorus is an essential nutrient for plants and is a crucial component of various fertilizers to enhance crop growth.

- **Animal feed:**

Phosphorites are also used in animal feed supplements. Livestock and poultry require phosphorus for bone development and overall growth, making phosphorites valuable in animal nutrition.

- **Industrial applications:**

Phosphorites find use in various industrial processes, such as in the production of detergents, food additives, and certain types of chemicals like phosphoric acid, which has applications in the food industry and as a rust inhibitor.

- **Pharmaceuticals:**

Phosphorus derived from phosphorites is used in pharmaceuticals, particularly in the production of medicines and supplements. For example, The Japanese have innovated in dental hygiene with an anticaries film derived from hydroxyapatite, the primary mineral found in tooth enamel.

- **Environmental remediation:**

Some phosphorites are used in environmental remediation efforts, such as in water treatment to remove heavy metals due to their ability to bind with contaminants.

- **Energy production:**

Phosphorites have also been explored for their potential in energy production, particularly in the development of phosphorus-based compounds for energy storage systems.

These diverse applications highlight the significance of phosphorites across various industries, from agriculture to pharmaceuticals and environmental sectors. The percentages of phosphorites uses in the main domains are presented in figure 13 (according to Fertilizers International 460, 2014).

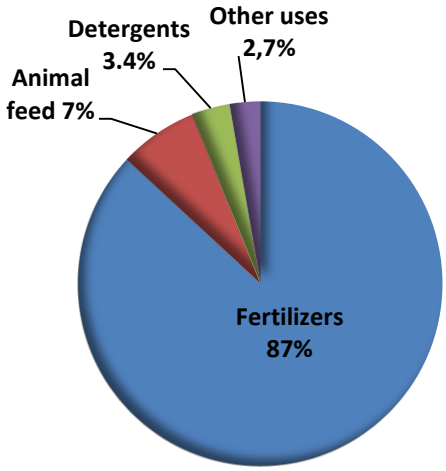

Fig. 13: Phosphorite use domains (Fertilizers International 460, 2014)

I.8. Phosphorites and environment:

Phosphorites and their derivatives can significantly impact the environment in various ways. Here are some key points to consider:

- **Water Contamination:**

The use of phosphorites in fertilizers, particularly in the form of phosphates, can lead to water contamination. Runoff from fields treated with phosphorus-containing fertilizers can carry excess phosphates into water bodies, causing eutrophication. This excessive nutrient influx leads to algal blooms, which deplete oxygen levels in water, harming aquatic life.

- **Heavy Metal Contamination:**

Phosphorites can contain heavy metals like cadmium, lead, arsenic, and mercury. Mining and processing these phosphorites can release these metals into the environment. When these metals (U, Cd, Mo, As, Se, …) leach into soil or water sources, they pose risks to ecosystems and human health (Nathan et al., 1996; Baioumy, 2005; Sassi et Sassi, 1999; Baturin et Kochenov, 2000). They can accumulate in the food chain, leading to toxic levels in plants, animals, and ultimately, humans.

- **Radioactive Elements:**

Some phosphorites contain naturally occurring radioactive elements like uranium and thorium. Mining and processing activities can concentrate these elements, leading to increased radiation levels in surrounding areas. This radiation can potentially contaminate soil, water, and air, posing health risks to both humans and wildlife. Additionally, the disposal of waste from phosphorite processing facilities may contain radioactive elements, necessitating proper management to prevent environmental contamination.

- **Soil Quality:**

Overuse of phosphorus-based fertilizers can disrupt soil quality. While phosphorus is an essential nutrient for plant growth, excessive application can alter the soil's natural balance. It can accumulate in the soil, leading to nutrient imbalances and reducing the soil's ability to sustain plant life in the long term.

- **Ecological Imbalance:**

Mining phosphorites can cause habitat destruction and loss of biodiversity. The process of extraction can lead to the destruction of ecosystems, impacting flora and fauna in the area. This disruption can have far-reaching consequences on the balance of local ecosystems.

- **Energy Consumption:**

The production of phosphorus-based products involves energy-intensive processes. From mining to processing phosphorites into usable forms, significant amounts of energy are consumed. This contributes to greenhouse gas emissions, thereby affecting climate change.

- **Long-Term Sustainability:**

Phosphorus is a finite resource, and the overexploitation of phosphorites raises concerns about its sustainability. As demand increases, there's a risk of depletion, leading to challenges in meeting future agricultural needs.

Efforts are being made to mitigate these environmental impacts. Strategies include improved fertilizer application techniques to reduce runoff, recycling phosphorus from organic waste, and exploring alternative sources of phosphorus to lessen reliance on mined phosphorites. Balancing the essential role of phosphorus in agriculture with its environmental impact remains a challenge, highlighting the need for sustainable practices and ongoing research into alternative solutions.

CHAPTER II

GEOLOGICAL FRAMEWORK

CHAPTER II

GEOLOGICAL FRAMEWORK

The Bled El Hadba phosphorite deposit is situated within the Djebel Onk region, itself a component of the broader Eastern Saharan Atlas. This chapter will delve into the geological traits of the Eastern Saharan Atlas, followed by an exploration of Djebel Onk, and culminating in an examination of the Bled El Hadba site. The focus on the Eastern Saharan Atlas predominantly centers on the Tebessa region.

II.1. Geology of Djebel Onk

The geology of Djebel Onk region is structured as asymmetric N80°-oriented anticlines and synclines, that are often faulted on their flanks. For phosphorite exploitation reasons, the Djebel Onk region is subdivided into a number of sectors, several of them are now under exploration and economic evaluation. Among these sectors: Djemi-Djema East, Djemi-Djema West and Kef Es Senoun exploitations that are under exploitation, while three others are located 6 to 35 kilometers away and are still under exploration: Djebel Onk Nord, Bled El Hadba, and Oued Bétita (Fig. 14).

II.1.1. History of research on the Djebel Onk region:

- Algerian phosphate at Djebel Onk was first discovered in 1873, followed by the discovery of the Gafsa phosphate in southern Tunisia in 1885.
- The exploration of Djebel Onk took place between 1906 and 1908 by Joleaud who studied the lithological, stratigraphic, and structural features among the Eocene layers and identified the phosphate layers at Djemi-Djema sector.
- In 1939, Laffitte identified phosphates in the Maastrichtian and Lower Eocene marls, emphasizing their significant occurrence in the Thanetian.

- In 1948, Flandrin revisited previous descriptions and stratigraphic scales of the Aurès, Négrine Range, and Djebel Onk, noting the presence of phosphates in the Danian, Thanetian, Ypresian, and Upper Lutetian.
- In 1951, Visse conducted an in-depth study of the Djebel Onk phosphorite deposit thoroughly examining its stratigraphy and estimating phosphorite reserves.
- In the early 1960s, phosphate exploitation became a top priority for Algeria's industrialization under the Constantine plan.
- From 1961 to 1963, multiple trials were carried out on Djebel Onk's deposits, employing a method to measure atmospheric radiation for phosphorite exploration, pioneered by the Bureau of Geological and Mining Research (B.R.G.M) in the Tellian Atlas.
- In 1963, Ranchin resumed the study of Djebel Onk, focusing on the Djemi Djema sector in the southern region, specifically examining the rock characteristics and petrography of the main phosphorite layers.
- Between 1971 and 1974, the National Company for Mining Exploration and Research (SONAREM) conducted an aeroradiometric survey in the region, and in 1975, Rudowicz proposed an interpretation based on phosphorite exploration. The following year, SONAREM initiated a phosphate exploration campaign in eastern Algeria (Raoudsep, 1977), followed by prospecting and evaluating the Djebel Onk mining district.
- The Russian (former USSR) cooperation led, between 1985 and 1987, to significant work, resulting in the implantation of 97 drills of about 1,732 meters, and 64 trenches. E.N. FERPHOS entrusted EREM with assessing phosphorite resources in all potential deposits across the Djebel Onk region.
- Based on previous work, E.N. FERPHOS conducted in 1989 a detailed study on all phosphorite deposits.

- From 1993, the mining research concentrated on the Djebel Onk phosphorites, with findings published in national and international journals (e.g., Mezghache, 1991; Bezzi et al., 2001; Mezghache et Hani, 2002; Mezghache et al., 2004; Bezzi et al., 2008.
- Kechiched et al. (2016) examined rare earth elements (REEs) concentrations in the Dj. Onk deposit (the southern basin), revealing REE contents ranging from 174.41 to 906.39 ppm (∑REE average = 623.01 ppm). However, phosphorites in the El Kouif, Dur, Tazbent (northern basin) exhibited lower ∑REE contents (125.45 to 472.44 ppm; averaging 265.57 ppm).
- Kechiched's 2017 thesis delved into a comparative study between North and South Tébessa's phosphates, covering sedimentology, geology, and geochemistry.
- In 2018, Kechiched and collaborators highlighted the enrichment of glauconites in rare earth elements, utilizing in-situ Laser Ablation ICP-MS analyses that revealed contents surpassing 1000 ppm. Additionally, glauconization of phosphate particles in the Kef Essenoun deposit contributed to updating the model for phosphorite deposition, favoring the allochthonous model of phosphate particles.

II.1.2. Lithostratigraphy of Djebel Onk:

The geology and stratigraphic framework of the Djebel Onk region were first established by Visse (1952), who shows a sequence of sedimentary layers spanning from the upper Cretaceous (Maestrichtian) to the middle Eocene (Lutetian). This sequence is overlain by a continental sandy and clayey series of Miocene and Quaternary ages. These studies were later updated by Cielenski et al. (1988) (Fig. 14 and 15).

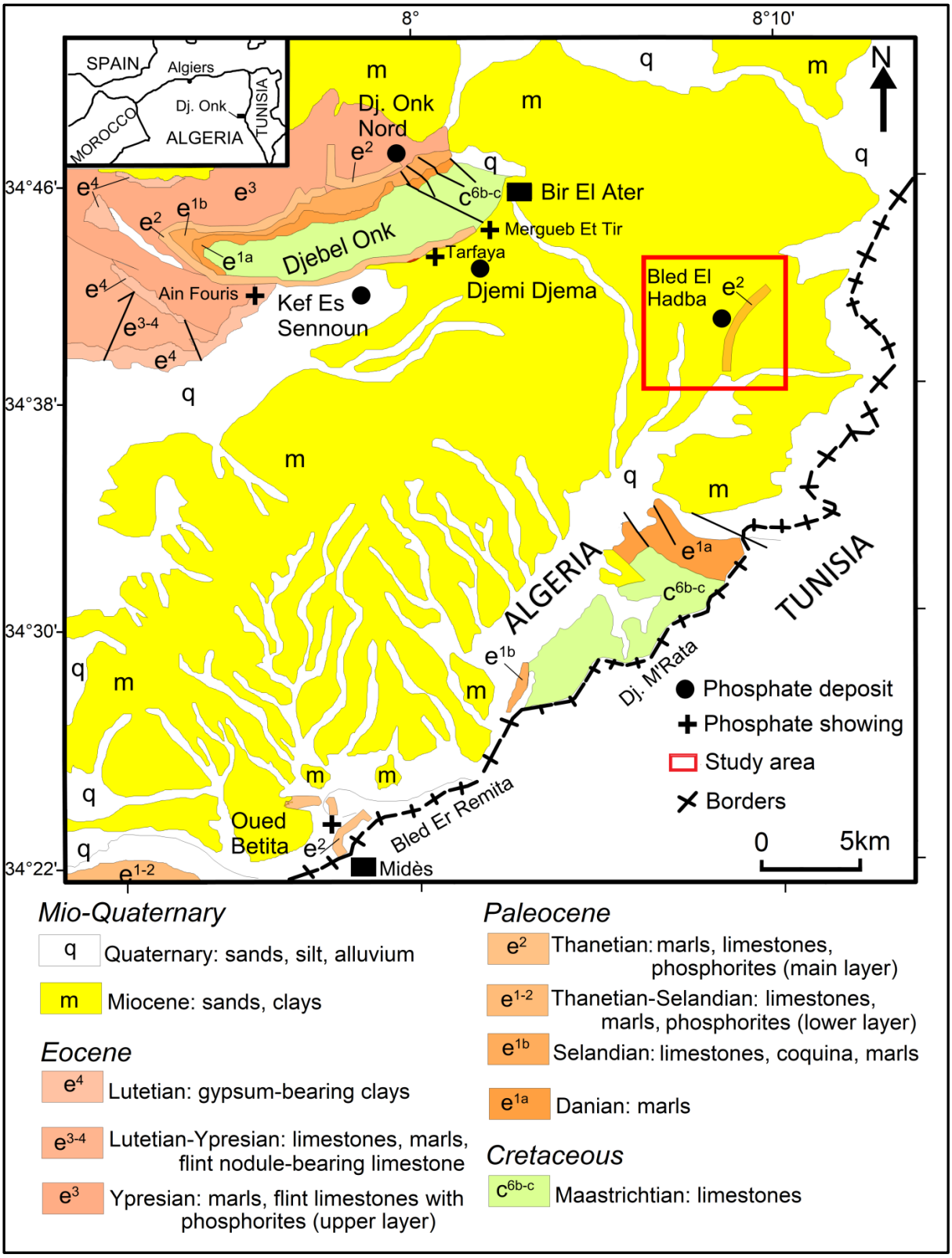

Fig. 14: geological sketch map illustrating the Bled El Hadba phosphorite deposit within the Djebel Onk region (after Cielenski et al., 1988) (coloring modified).

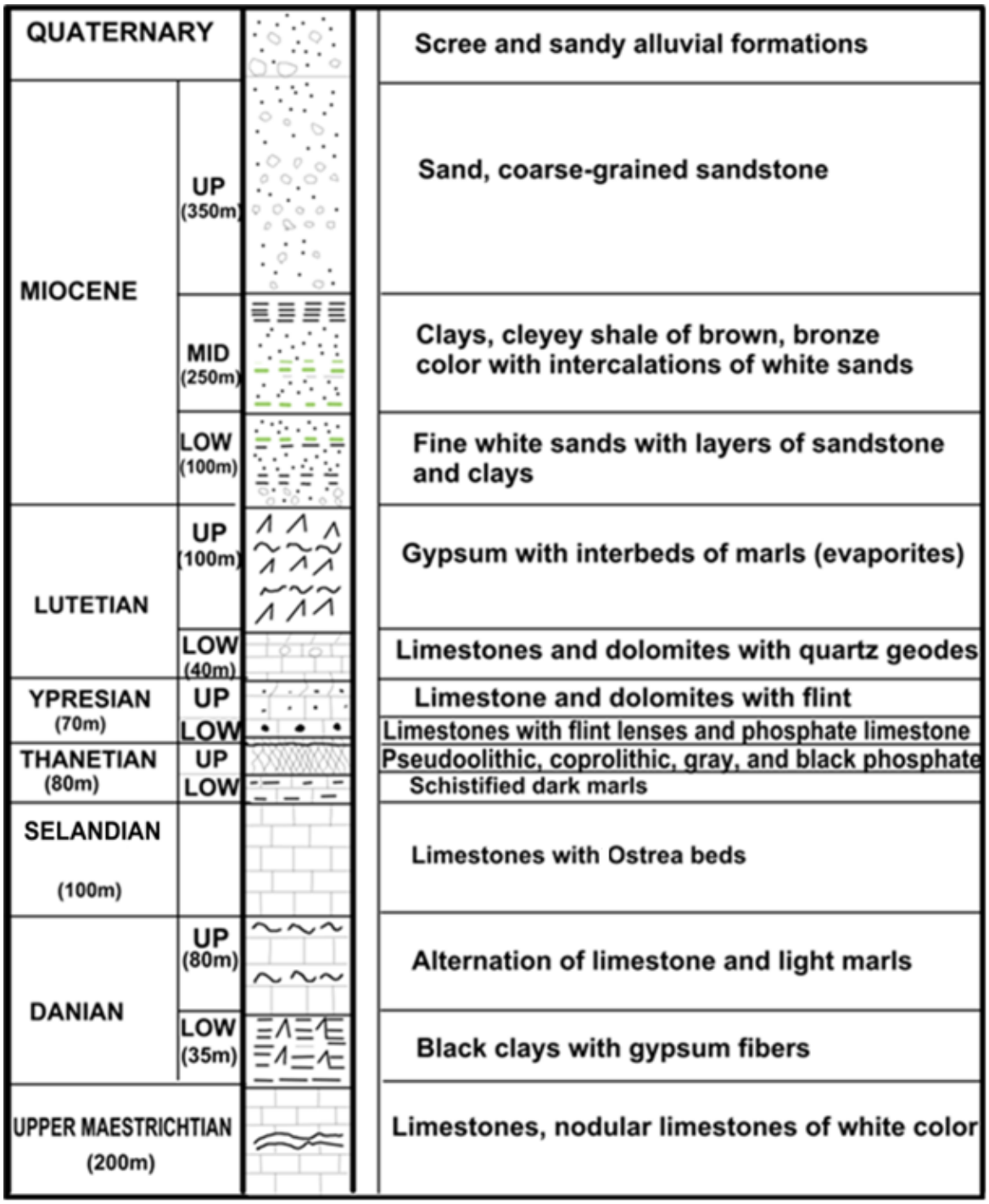

Fig. 15: Stratigraphic column of the Djebel Onk region, NE Algeria.
(after Cielensky et al., 1988)

II.1.2.1. The Cretaceous:

In the context of the Djebel Onk anticline, which is characterized by a rugged tectonic expanse, the oldest visible sediments comprise solely Maestrichtian deposits, which are

characterized by massive white limestones. The limestones in question contain flint-marl intercalations, the most conspicuous of which can be observed within the core of the Djebel Onk anticline. The upper part of these formations exhibits a distinct reddened surface, which is easily discernible from the topography.

II.1.2.2. The Paleocene

The Paleocene in the region is characterized by the presence of diverse marine sediments, which are notable for their substantial thickness, extending up to 350 m.

Danian:

This phase comprises a robust marly complex, which demarcates the Upper Danian and the Lower Danian.

The Upper Danian exhibits limestone formations with considerable intercalations of thick marl, which is characterized by hard cream-colored to white limestone juxtaposed with soft clayey schistose marls of varying thickness (ranging from 10 cm to 1 m).

Conversely, the Lower Danian comprises schistose marly clays in dark gray or greenish brown hues, exhibiting irregularly dispersed hard marl banks occasionally intersected by gypsums, which attain a thickness of 30 to 40 m.

Selandian:

This stratum is characterized by extensive limestone beds, which are intersected by beds of marl. The limestone beds contain the Ostrea canaliculata Sow and Ostrea multicostata Desh (Pelecypoda) species. Such observations can be made at various points, including DJ. Onk, Dj. Darmoun, Djemi-Djema, Oued Betita, and Bled El Hadba, presenting a thickness of 60 m.

Thanetian:

This horizon hosts mineralization and appears prominently along the Djebel Onk anticline, spanning 72 m and segmented into:

- Lower Thanetian: characterized by dark gray to black schistified marls, which feature conglomerates in the lower segment and thin layers of phosphates. It is notable that the formation includes distinct faunal marl layers (Thesio-ogracitis), followed by phosphate intercalations up to 2 m thick, culminating in coarse gastropod-containing limestones and marls. The thickness of the formation varies between 30 and 40 m.

- Upper Thanetian: The stratigraphic sequence begins with a dolomitic layer that houses gastropods and is underlain by a phosphate layer (averaging 30 m in Djebel Onk and Bled El Hadba). This layer diminishes towards the north. Towards its western and southern limits, the stratum transitions into a lumachellic level, which is particularly exploited in Kef Essennoun.

II.1.2.3. The Eocene:

Ypresian:

The Ypresian formations, which are found in great abundance in the Djebel Onk region, rest directly on the Thanetian deposits, and extending over a depth of 32 meters. The formation comprises flint limestone, which contains an intermittent phosphate layer (3 meters) and marly limestone with upper phosphate beds (4.5 meters), and limestone with black flint nodules, exhibiting a ferruginous patina ranging from black to red-brown, with a thickness of 26 meters.

Lutetian:

Overlapping the Ypresian rocks, the Lutetian formations, which are 270 meters thick in the Dj Darmoun region, can be categorized as follows:

- Lower Lutetian: marked by transitions in facies, characterized by the disappearance of limestones and the emergence of chalky white marls hosting quartz geodes and flint. This layer

spans 30 meters and is succeeded by whitish limestones with quartz nodules (15 meters thick) and gypsum formations interlaced with limestone beds (150 meters thick).

- Upper Lutetian: Exhibiting an evaporitic facies, this layer comprises gypsum, greenish clay, green phosphate clay, and limestone beds. The distinct features include phosphated green clay, limestone banks (10 meters thick), and upper green clays interspersed with gypsum benches, spanning 65 meters. The characteristic fauna includes Ostrea multicostata and Cardia placunoides.

II.1.2.4. The Miocene:

The Miocene period is characterized by a complex of terrigenous rocks comprising conglomerates, clays, sands, and shales, divided into three segments:

The Lower Miocene: comprises conglomerates, coarse-grained, and medium-grained sands interlaced with thin layers of silty clays, spanning 200 meters.

The Middle Miocene: predominantly clayey and brown in color, occasionally shifting to shale. It features intercalations of fine and medium-grained sands with a thickness of 100 m.

The Upper Miocene comprises a heterogeneous assemblage of sandy-clayey rocks and sandstones, which are intercalated with gravel banks and large rounded blocks.

II.1.2.5. The Quaternary:

The Quaternary formations, which are extensive across the region, are predominantly composed of scree slopes, sandy deposits, gravels, blocks, and alluvial and fluvial deposits.

II.1.3. Tectonic characteristics of Djebel Onk region:

The Onk-Gafsa-Métloui basin is characterized by a series of asymmetric anticlines and synclines, which are often faulted on their flanks. The anticlines are aligned along a southwest-northeast axis and offset by transverse faults that range between N120° and N140° E. The anticlines of Djebels Onk, Djemi-Djema, and Oued Betita are located on the periphery of the Southern Atlas Flexure, which represents an area where the mobile Atlas region collides with the stable Saharan platform. In more precise terms, they are part of the northern branch of the east-west-directed flexure.

The region can be divided into three main tectonic phases, which are responsible for the structuration of the Dj. Onk region:

• Synsedimentary Tectonics:

During the Paleogene period, a northwest-southeast compressional phase resulted in the formation of synsedimentary ripples and faults. These early tectonic movements resulted in the formation of sedimentation gaps within the Paleocene-Eocene series, as well as the development of paleogeographic features such as highs and lows. These changes influenced the deposition of phosphate sediments. This early deformation may be linked to the halokinesis of the Triassic evaporites, particularly during the Paleocene-Eocene period.

• Mid-Post-Eocene and Pre-Miocene Tectonics:

As the Upper Lutetian series emerged, a significant phase of folding and transverse distensive deformations (N120° to N150°) occurred in the Aurès region. This resulted in the fragmentation of the Upper Cretaceous to Eocene series into small, elongated horsts and grabens along the N170°E direction. These structures were subsequently affected by erosion during the Ante-Miocene period and differential erosion.

The majority of these folds were formed prior to the deposition of Miocene sands. The Djebel Onk anticline emerged during this tectonic phase, as documented by Mezhgache et al. (2000).

• Late Miocene, Post-Burdigalian, Pliocene-Pleistocene Tectonics:

This phase represents a significant folding event in the Tunisian Atlas. Folding in the Upper Cretaceous-Paleocene-Eocene and Miocene series results in the formation of large antiform and synform structures, which subsequently reappear as horsts and grabens within the previously existing structures. These tectonic movements result in the formation of mega-folds in a southward direction and on the reverse flank of Djebel Onk and Djemi Djema. These structural changes define the current landscape of the Djebel Onk region (Fig. 16).

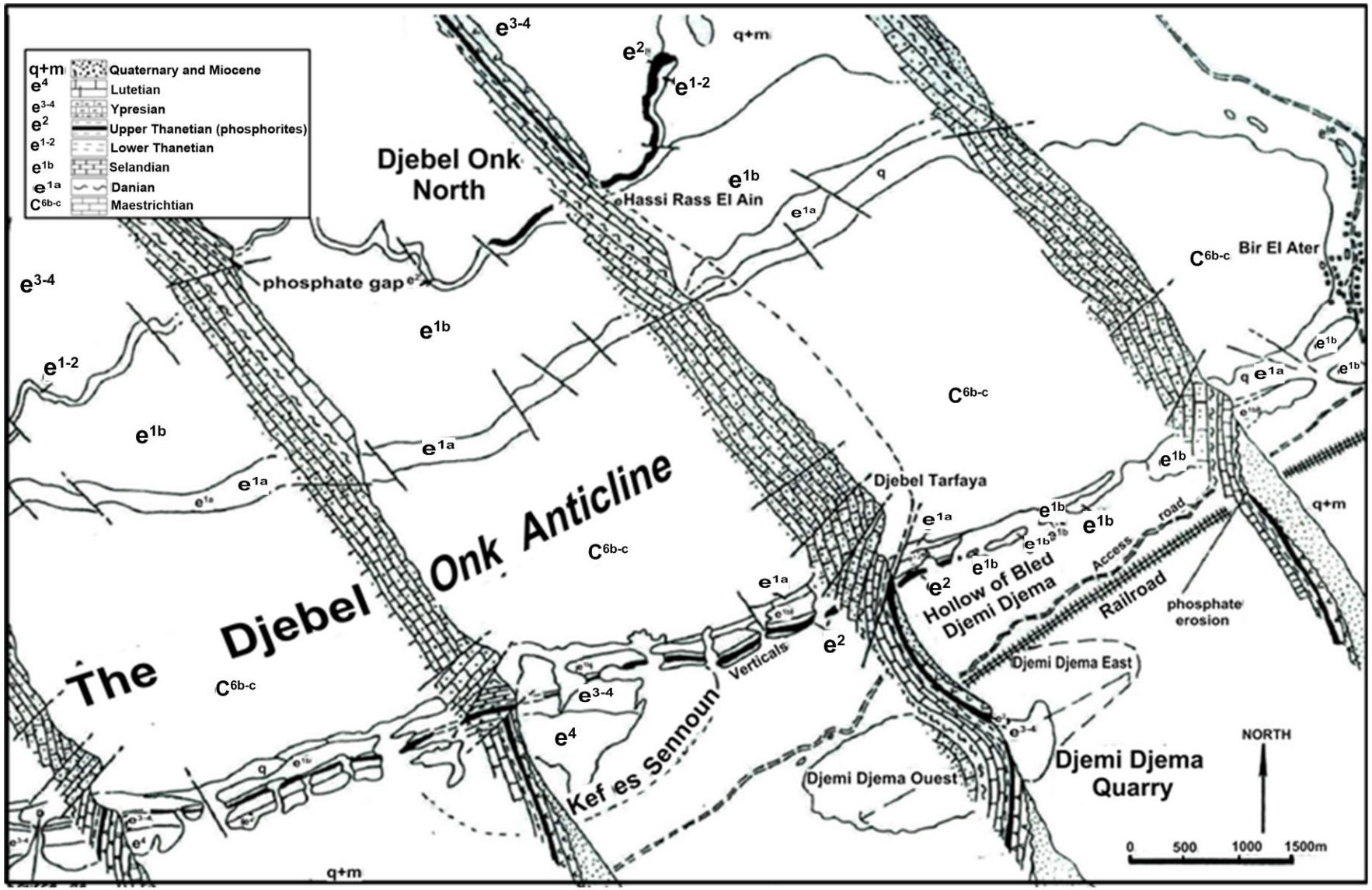

Fig. 16: Stratigraphic and structural sections of the North and South flanks of Djebel Onk (Cielensky et al., 1988)

II.1.4. Paleogeography of Djebel Onk:

The Djebel Onk region is considered to be the western section of the Gafsa-Métlaoui-Djebel Onk basin (as defined by Sassi, 1980) from the Upper Paleocene to the Lower Eocene. The area was once home to a shallow epicontinental sea, situated between the Kasserine Island in the north and the Djeffra barrier in the south (Fig. 17).

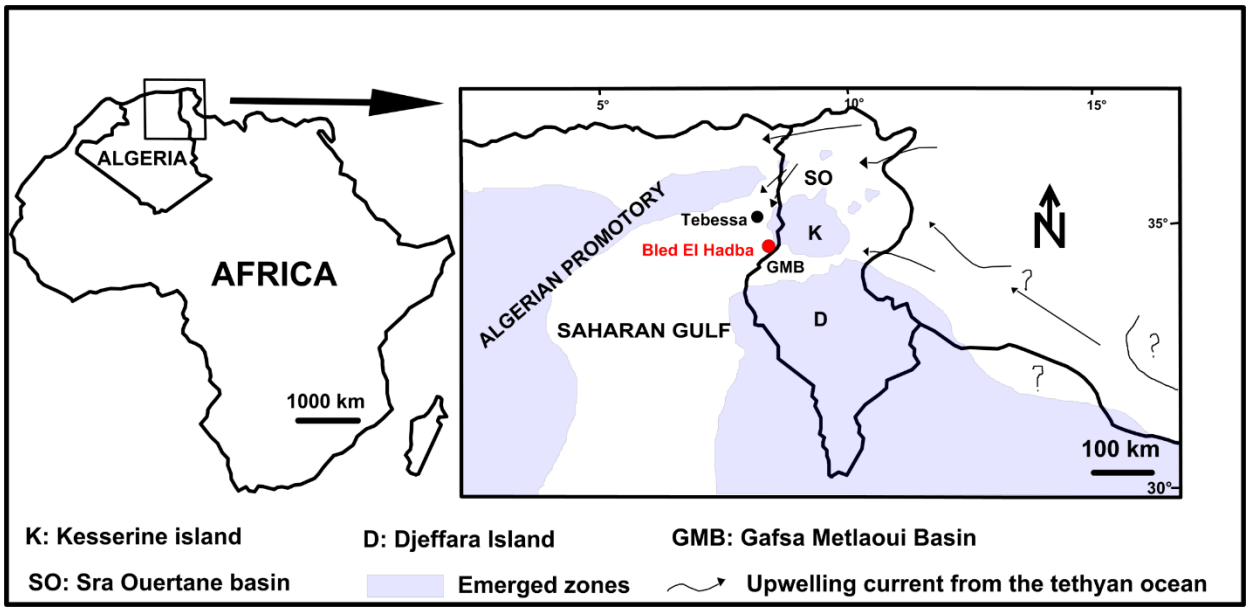

Fig. 17: Paleogeographic situation, during early Eocene, of the Algero-Tunisian phosphorites, including the region under investigation (summary after Sassi, 1974; Burollet and Oudin, 1980; Chaabani, 1995; Winnock, 1980; Zaïer et al., 1998).

The Djebel Onk area has undergone a series of evolutionary stages throughout its geological history, resulting in the formation of distinct imprints within its sedimentary layers. Among these developmental phases:

Marine Sedimentation Period:

This sedimentation phase commenced at the end of the geosynclinal basin's development, spanning North Africa from the Maastrichtian to the Upper Eocene. During the Maastrichtian, there was a gradual subsidence and a period of tranquil sedimentation. A significant facies shift marked the conclusion of the geosynclinal sedimentation cycle between the Maestrichtian and

the Danian, signifying an orogenic shift. This shift resulted in a sudden reduction in basin depth, as evidenced by the persistent clay-carbonate sedimentation observed throughout the Danian.

- **Lower Thanetian:** A further reduction in basin depth was observed. This phase was marked by a significant influx of clay-rich material and clayey-marly sediments, indicating a gradual closure of the sedimentation area and a regression in the marine environment.
- **Upper Thanetian:** This phase is marked by a notable influx of phosphate sedimentation, which signifies a reopening of the sedimentary domain and a return of transgressive influences. Toward the conclusion of the primary phosphate sedimentation phase, a regressive phase commenced, characterized by phosphate reworking and, in select locales, the emergence of a conglomerate horizon comprising dolomite pebbles, indicative of a marine environment. This trend was emerging. The near-saturation of seawater conditions conducive to evaporite facies led to the presence of dolomite, which serves to emphasize the regressive nature of these phosphate facies (Ranchin, 1963). This regressive phase was followed regionally by the Ypresian transgression (flint limestone), which extended beyond previous formations.

The thickest phosphate layers, situated between black marls below and dolomites above, were observed at the Djemi Djema (30m) and Kef Es Sennoun (approximately 50m) deposits, which are characteristic of the subsidence trough.

- **Lutetian:** A gradual reduction in basin depth led to the formation of shoals, lagoons, and evaporite deposits. Variations in thickness and the composition of the phosphate layer reflected a diverse paleogeography.

Period of Continental Sedimentation:

From the Upper Lutetian onward, the terrains started emerging. The Oligocene period does not bear traces due to pre-Miocene erosion.

- **Miocene-Paleocene:** It witnessed an intense phase of continental sedimentation, marked by the deposition of sands, clays, and conglomerates.
- **Quaternary:** The period was characterized by erosion products settling on slopes and valleys, comprising colluvium, alluvium, and slope debris. Distinct evidence of a brief yet pronounced Pleistocene glaciation is well preserved in Djebel Onk.

II.1.5. General characteristics of Djebel Onk phosphorites:

The Djebel Onk basin is notable for its rich mineral composition, which is primarily characterized by phosphorites that are composed mainly of pellets and comprolites. These phosphorites include frequently organic matter, predominantly diatoms and radiolarians, which class them as 'biophospharenites' within the arenites (grains smaller than 2mm). Infrequently, they form biophospharenorudites within the rudite class (grains larger than 2mm). The phosphorite facies of the basin often exhibit phosphate particles homogeneity, with fine grains (ranging from 200 to 300 μm) or a mixture of fine to coarse grains (up to 2 to 3 mm). These grains are cemented by clayey, calcitic, or dolomitic matrix, with rare other particles, such as quartz, zeolites and glauconite.

Diatoms and radiolarians play a pivotal role in the formation of phosphatic pseudooliths, a process elucidated by Champetier and Joussement (1979). The phosphatic facies typically display a color spectrum ranging from beige to brown, with occasional transitions to dark gray or black at the base of the layer. It is noteworthy that the black phosphate contains hydrocarbon impregnations, as observed by Prian and Cortiel (1993).

The 30-meter-thick layer of phosphorites exhibits significant facies variations, both vertically and laterally (Prian and Cortiel, 1993; Mezghache, 2002 and 2004). Two principal types of phosphatic facies are distinguished:

- **Phospharenites:** The specimens exhibit coprolithic biophospharudites with a mixed grain size, ranging from 250 μm to over 1 mm. Typically, the ore is cemented with dolomite and calcite, resulting in either a hard ore or, on occasion, a less compacted, softer ore.
- **Pseudo-oolithic phospharenites:** The finer grains, with a more consistent size (ranging from 100 to 300 μm), are typically bound by clay, resulting in a softer, crumbly ore. However, in some cases, carbonate cementation may also be observed.

The entire 30-meter-thick layer is subdivided into three sub-layers: the lower, main, and upper sub-layer. An intriguing facies is the dark gray pseudoolithic ore, which is organic-matter rich and often forms the base of the phosphorite layer. The organic matter is linked to the presence of hydrocarbons.

From a geochemical point of view, the phosphorites are composed mainly of P_2O_5, CaO, and minor MgO, SiO_2, Al_2O_3, Fe_2O_3, Na_2O, K_2O, CO_2, and F (Cielensky and Benchernine, 1987). These elements are concentrated within apatite, clay minerals, organic matter, bone fragments, and secondary minerals such as iron oxides and hydroxides.

- Uranium (U) and strontium (Sr) are chiefly found in apatite.
- Sodium (Na), barium (Ba), vanadium (V), nickel (Ni), cobalt (Co), chromium (Cr), zinc (Zn), copper (Cu), scandium (Sc), and zirconium (Zr) primarily reside in clay minerals.
- Cobalt (Co) and manganese (Mn) might appear as oxides and hydroxides alongside iron compounds.

- Cadmium (Cd) is notably present in dolomitic carbonates that form a significant part of the matrix (Dassamiour et al., 2010).
- Rare Earth Elements (REEs) are predominantly present in pellets and coprolites. Recent research (Kechiched, 2016, 2017, 2018) shows that REEs are linked to apatites. However, glauconites, too, exhibit notably high concentrations of REEs, surpassing 1000 ppm and even 2000 ppm in some glauconite samples (Kechiched et al., 2018).

II.2. Geology of Bled El Hadba deposit

The geology of the Bled El Hadba deposit has been the subject of many studies and prospection companies. It forms the extreme east part of the Dj onk phosphatic region.

II.2.1. Geographic location of bled El Hadba:

The Bled El Hadba phosphorite deposit is located at 14 kilometers southeast of Bir El Ater town and merely 6 kilometers from the Algerian-Tunisian border (fig. 18).

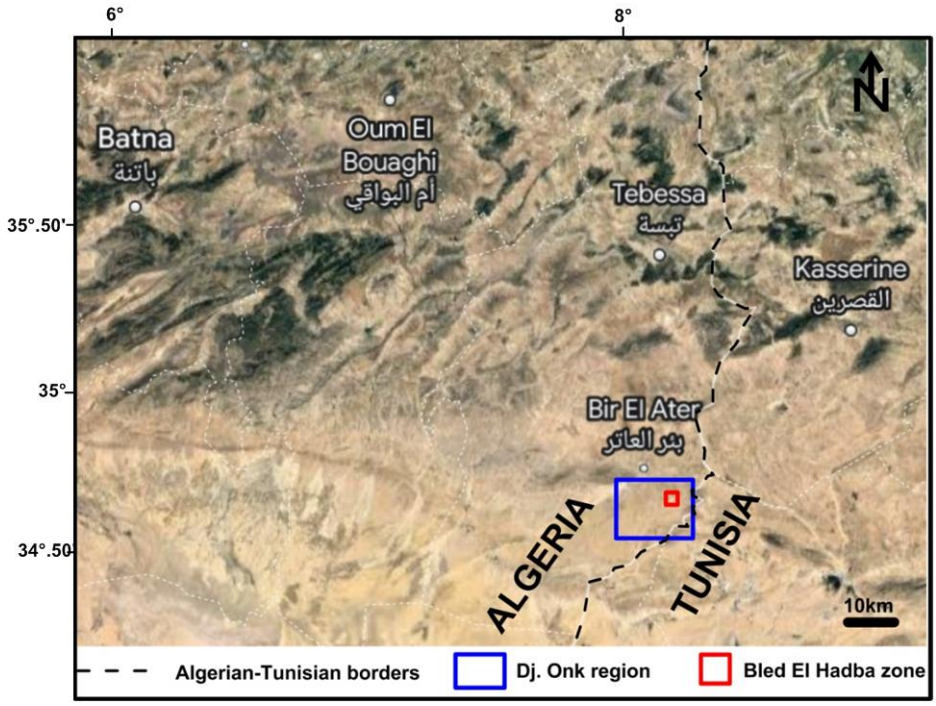

Fig. 18: The Bled El Hadba and Dj Onk geographic localization (Landsat-8, 2023).

II.2.2. Previous research on Bled El Hadba deposit:

This section lists previous and current works conducted on the Bled El Hadba deposit. Several studies on this deposit have inventoried adjacent areas and show mineral resources. The first documented drilling occurred in the late 1970s as part of SONAREM's study: 83 boreholes (12,076 m) were drilled in multiple campaigns, covering an area of approximately 12 km².

- **SONAREM Study (1976 - 1978):** 9 core-drilled boreholes (741 m) were carried out in an exploration campaign. These confirmed the presence of phosphorite layers similar to those previously discovered through mapping and outcrop sampling.
- **EREM Company Study (1985 - 1987):** 11 core-drilled boreholes (a total of 1170 m) were conducted in the southern part of the deposit as part of EREM's drilling campaign. The drilling grid was 400 x 600, with core diameters of 72, 60, and 52 mm in phosphorites, and 93 mm in upper dolomitic limestone and phosphorites. Core recovery in phosphorite exceeded 85%; average sampling intervals were 1 m (rarely 0.5 m). Log plotting was done at a 1:200 scale. Analyses were conducted for 8 elements: P_2O_5, CaO, MgO, SiO_2, Fe_2O_3, CO_2, insoluble residues, and U. An average density of 2.3 t/m³ and porosity of 19.7% were determined for phosphorites, while limited measurements provided 2.5 t/m³ and 10.4% for phosphatic limestone.
- **BRGM-SOFREMINES Work (1993):** Chemical analyses were carried out for six element determinations: P_2O_5, CaO, MgO, Al_2O_3, SiO_2, Fe_2O_3, and loss on ignition (including organic carbon and sulfur in six samples). 44 thin sections were studied for facies detailed petrography. Density determination resulted in 2.3 t/m³ for phospharenites and 2.3 - 2.5 t/m³ for the upper dolomitic phosphate horizon. The average thickness of this deposit was estimated at 30 m, comprising 3 phosphorite horizons, with main (principal) P_2O_5-rich layer and lower and upper layers having less phosphate and a more significant dolomitic matrix, including lumachellic levels.

- **FERPHOS Work:** CERAD carried out 12 drillings (1,277 m) in the late 1990s, covering the northern part of the deposit. Additionally, 12 trenches were excavated, and new topographic maps were generated at scales of 1:1,000, 1:2,000, 1:5,000 based on 20 points/ha over a total area of about 500 ha. Eleven sections, each spaced 250 - 300 m apart and approximately 1,800 m long, were surveyed. Further, shorter sections of 300 - 800 m in length were interpreted in outcrop areas. Core recovery in phosphorites was > 84%. FERTIBERIA (Spain) and ORGM laboratory in Boumerdès conducted geochemical analyses. 66 tons of ore from three phosphate layers were sent to FERTIBERIA for processing trials. Additionally, fine section samples were taken for density determination. Chemical analysis for 18 elements was performed. The average density determined from 47 phosphate samples was 2.14 t/m³, whereas EREM data gave 2.22 t/m³ for the deposit.
- **ORGM Work:** ORGM conducted 48 drillings (a total of 8,480 m) in 2013/2014 for resource determination. Exploration was carried out by ORGM using Algerian drillers before DMT Consulting GmbH (DMT) intervened. ORGM handled logging and sampling works. Remaining cores were stored in core boxes placed in core warehouses. Sampling was performed from split cores. Drilling dip was measured using an inclinometer. Following ORGM's operations, it was concluded that the geology of Bled El Hadba is relatively straightforward.

II.2.3. Stratigraphy of Bled El Hadba deposit:

The lithostratigraphic succession is, in broad lines, quite similar to that of the Djemi-Djema and Kef Es-Sennoun with a lithological succession comprising about 500 m thick layers of sedimentary rocks which were formed during the Maestrichtian to the Lutetian times. These layers are partly covered by Quaternary continental clastic sediments, including sandstones and

clays. However, significant lithological variations within the Bled El Hadba phosphorite sequence have been observed in the form of an outcrop NE-SW-oriented layer. This layer extends westward beneath the Ypresian flint-bearing limestones and Miocene sands (Figs. 19 and 20).

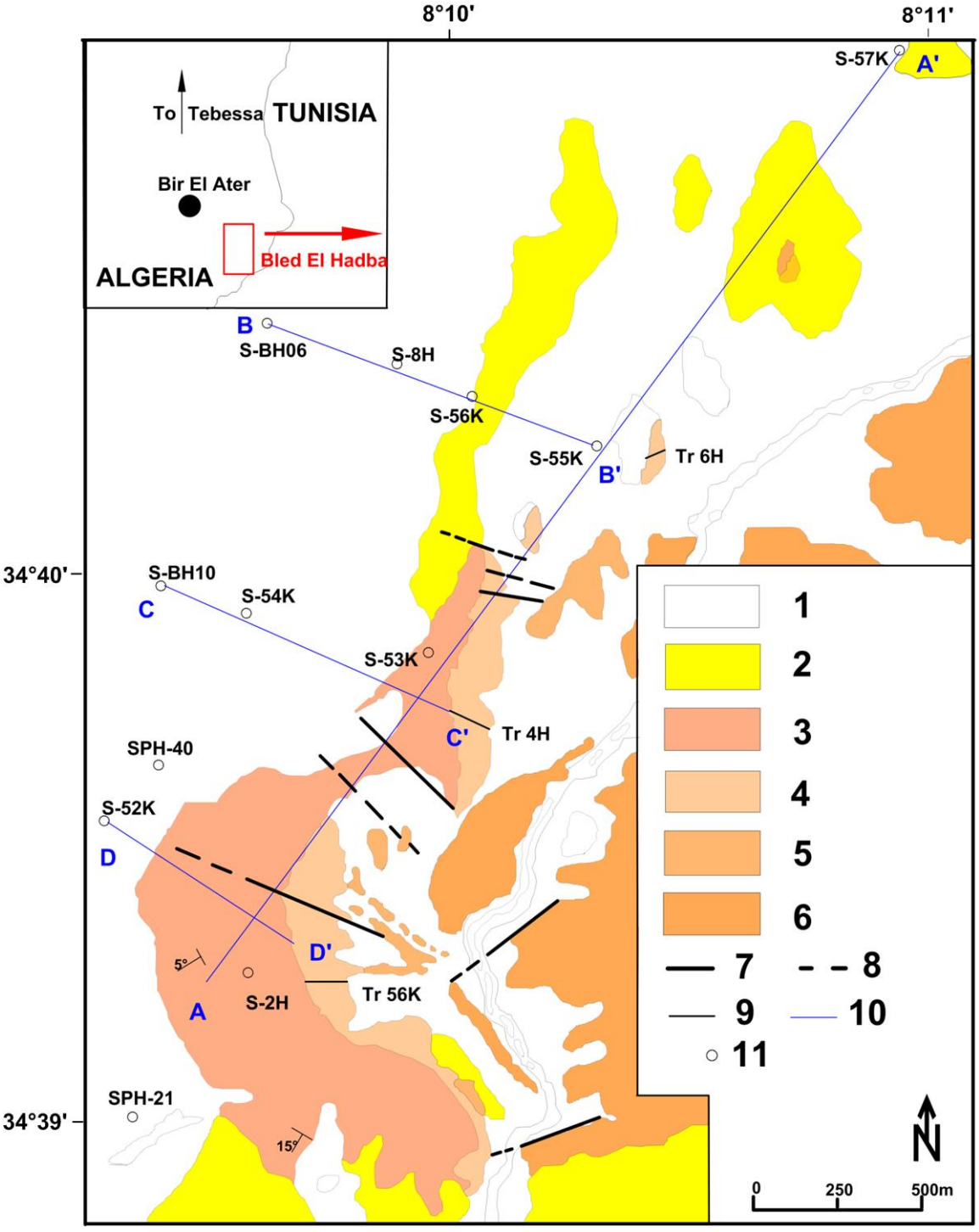

Fig. 19: The geological map of Bled El Hadba (Cielensky and Benchernine, 1987) (coloring modified). 1: Alluvial deposits; 2: Limestones, sands, and clays; 3: Ypresian chert-bearing limestone; 4: Thanetian phosphorite layer; 5: Lower Thanetian marls and clays; 6: Selandian marls and limestones; 7: Observed fault; 8: Hypothetical fault; 9: Trench; 10: Geological section line; 11: Borehole.

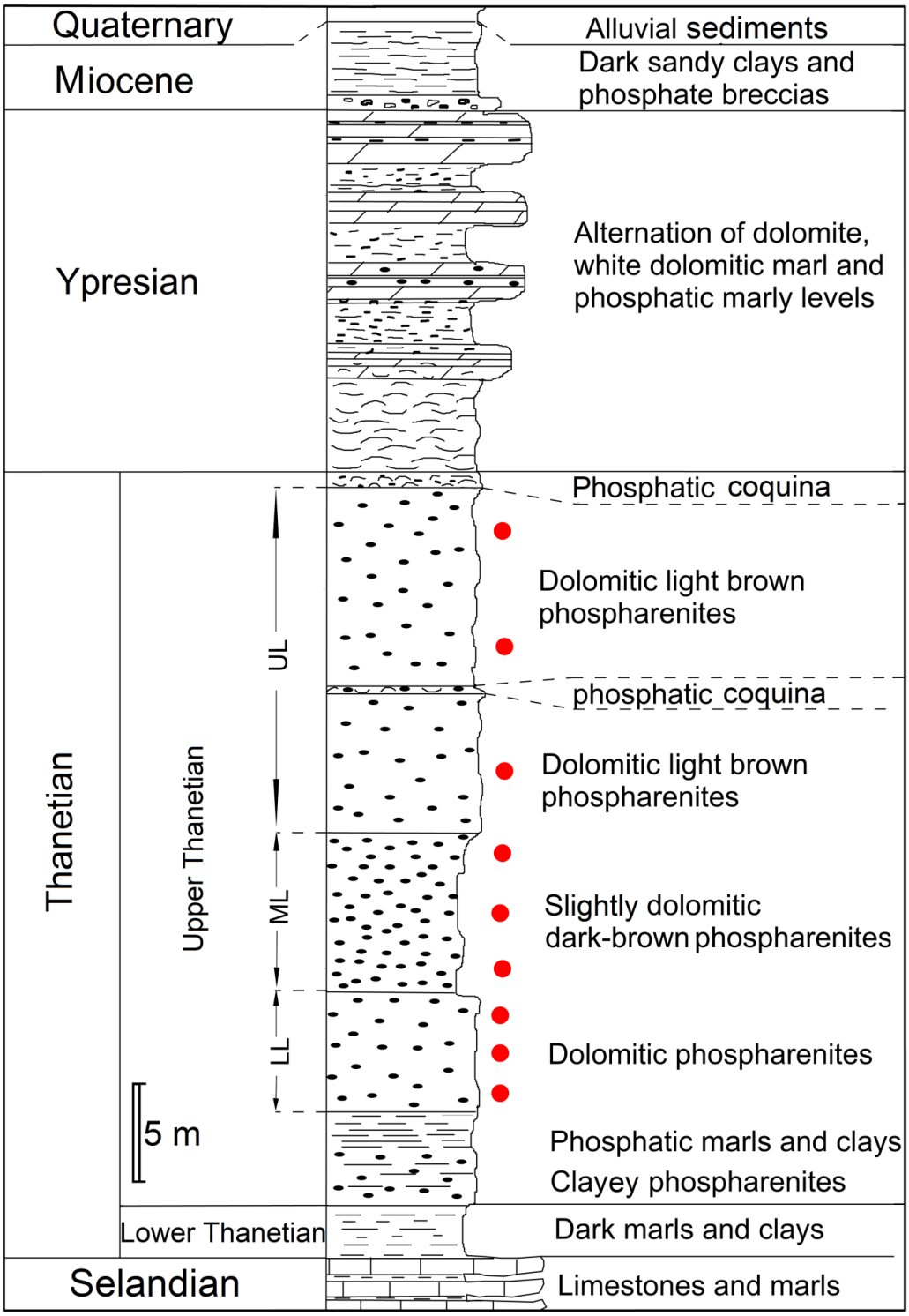

Fig. 20: The Bled El Hadba lithostratigraphic column (after EREM, 1987; modified) (Red marks represent sample positions). UL: Upper Layer, ML: Main Layer, LL: Lower Layer.

II.2.3.1. Paleocene

Selandian:

The Selandian formation is exposed in the southeast of the deposit. At the bottom, there are silicified limestones with bioclastic coquina and other fossilized organisms. These limestones are followed by a sequence of alternating coquina-bearing clay, calcareous clays, and dolomitic marls. Above them, there is a dolomite layer, on top of which rest light gray limestones slightly phosphatic. This layer can reach a thickness of up to 100 meters.

Thanetian:

- **Lower thanetian:** It comprises dark grey to greenish clayey marls and bituminous material which occurs sporadically in the form of thin layers of grey limestone, and about 10 cm thick phosphatic beds. At the top of this series were deposited coprolitic phosphorites with coarse-grained and clayey-marly matrix, with intercalation of thin layers of phosphatic and dolomitic marls. The thickness of this series varies from 0.80 m in borehole SPH-40 to 5.90 m in borehole SPH-21 (cf. Fig. 19), and exceeds 3m within the deposit. The lower Thanetian sediments ends with the deposition of a series of layered grayish phosphatic marls and are typically between 1.70 and 2m in thickness.
- **Upper thanetian:** It exclusively constitutes the most productive zone of the phosphorite mineralization known in the actively mined deposits of the Djebel Onk basin. The geological map of Bled El Hadba (Fig. 19) shows that the Thanetian phosphorite layer that reaches around 30 m in thickness and forms a NE-SW trending outcrop, is gently dipping under the Ypresian flint-bearing limestones and Miocene sands (Bezzi et al., 2008). In general, these phosphorites

show grain sizes ranging from fine to coarse, and colors of beige, greyish and, in places, black with a bluish tinge, in the form of lenses. The hard phosphorite facies is characterized by calcareous matrix, whereas the matrix of friable phosphorites is mainly clayey. This phosphorite layer contains a variety of bioclasts, including lamellibranchs, gastropods, fish bone and shark teeth.

II.2.3.2. Eocene

Yprisian:

It lies conformably above the upper Thanetian phosphates and comprises grayish compact, occasionally dolomitized, limestone at the bottom with centimeter-sized flint nodules and thin phosphorite horizons measuring less than 2 meters in thickness. This is followed by the deposition of whitish to grayish, often gypsum-rich marls, and layers of flint, as well as dolomitized limestone beds. Within this marly formation, a distinctive 3 to 14 meter-thick phosphorite layer emerges, that is composed of fine to medium-grained light gray phosphorite with calcareous-dolomitic (magnesian) cement. It occasionally includes centimeter-thick intercalations of limestone and flint. Above these marls, the Ypresian ends with a series of light gray coquina limestone, featuring quartz geodes and flint nodules at the top. The total thickness of the Ypresian can reach 55 meters. Nevertheless, this thickness gradually decreases towards the northwest and south of the deposit, leading to an Ante-Miocene erosion unconformity that truncated the Ypresian formations.

II.2.3.3. Miocene

It covers the previously described lithologies, showing a progressively increasing thickness towards the west and northwest where it reaches 77 meters. These sedimentary deposits composed mainly of sand, shows intercalations of marly limestone and dolomitic rock fragments.

II.2.3.4. Quaternary

Quaternary deposits are widely distributed throughout the studied area. They comprise both aeolian (wind-deposited) and alluvial (water-deposited) formations.

II.2.4. Tectonic features

Located on the western flank of Djebel Zerga, the Bled el Hadba area is composed of Selandian, Thanetian, and Ypresian sediment outcrops. These sediments show a sub-horisontal structure, slightly dipping (5 to 10°) to the wewt-souththwest (Figs. 19 and 21). This structure is affected by a series of faults, resulting in significant vertical and horizontal displacements, with horizontal shifts sometimes exceeding 100 meters. The prevailing directions of these faults are mainly NW-SE (Fig. 19), with a greater frequency and significance of occurrences observed towards the Eastern parts of the deposit.

II.2.5. Description of phosphatic layer

The Thanesian phosphatic layer presents a general W - NW dipping monocline structure. The geological section (AA') (Fig. 21a) shows a maximum thickness of phosphatic layer in the central part of the zone (borehole S-53K). This thickness decreases to the NNE until its disparition with the Eocene limestones in the borehole S-57K on top of the lower Thanetian. The sections (BB'), (CC') and (DD') (Fig. 21b, c and d, respectively) show a dipping that change between 5 to 15° to the NW. They also show that the thickness of phosphorite layers increases from the north to the south part of the area.

As indicated on figure 21, the phosphorite layer of the Upper Thanetian is subdivided into three sub-layers: lower, main and upper sub-layer. This subdivision is based on the P_2O_5 and MgO contents. The lower sub-layer (LL) shows a generally lower thickness than the two other sub-layers, and does not exceed 5m. However, it can reach 18m in the western part of the area (Fig. 21d). The main sub-layer (ML) displays variable thicknesses, between a few meters

up to about 25m. The upper sub-layer (UL) presents thickness which varies between 1 to more than 18 m (Fig. 21a).

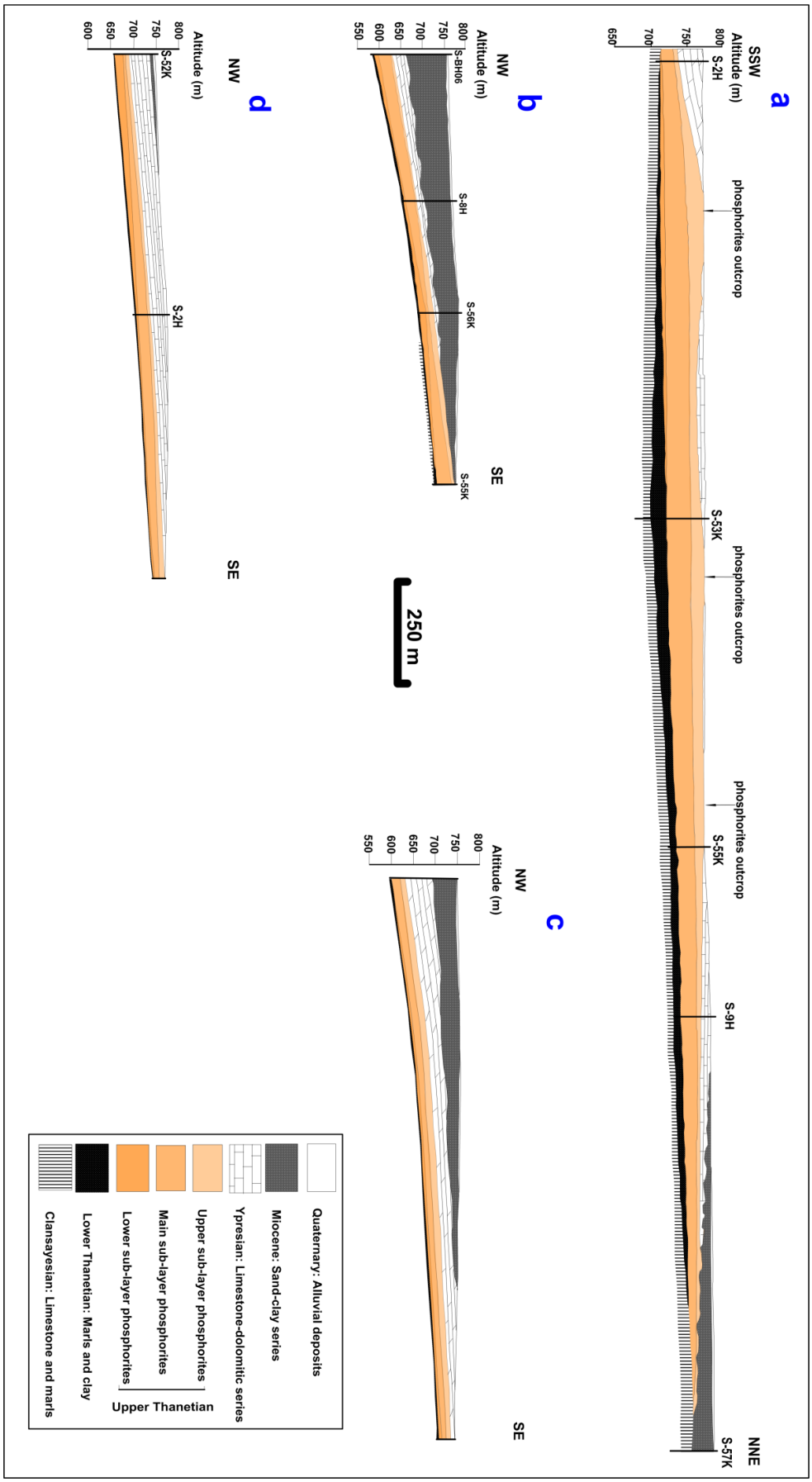

Fig. 21: Geological sections of Bled El Hadba region. a: (AA'), b: (BB'), c: (CC'), d: (DD') (section lines are shown in Fig. 19) (modified, after Kechiched, 2011)

The main petrological characteristics of the three sub-layers (lower, main, and upper) of the Bled El Hadba phosphorite are as follows:

- **Lower sub-layer:**

This sub-layer (Fig. 22) exhibits fine to medium-grained phosphorite facies with a carbonaceous (calcareous-dolomitic), rarely siliceous, cement contributing to the relative hardness of the facies. The carbonaceous material, predominantly dolomitic, often forms levels with a low occurrence of phosphorite elements (pellets and coprolites) and rare green glauconite particles. (Fig. 22b-d).

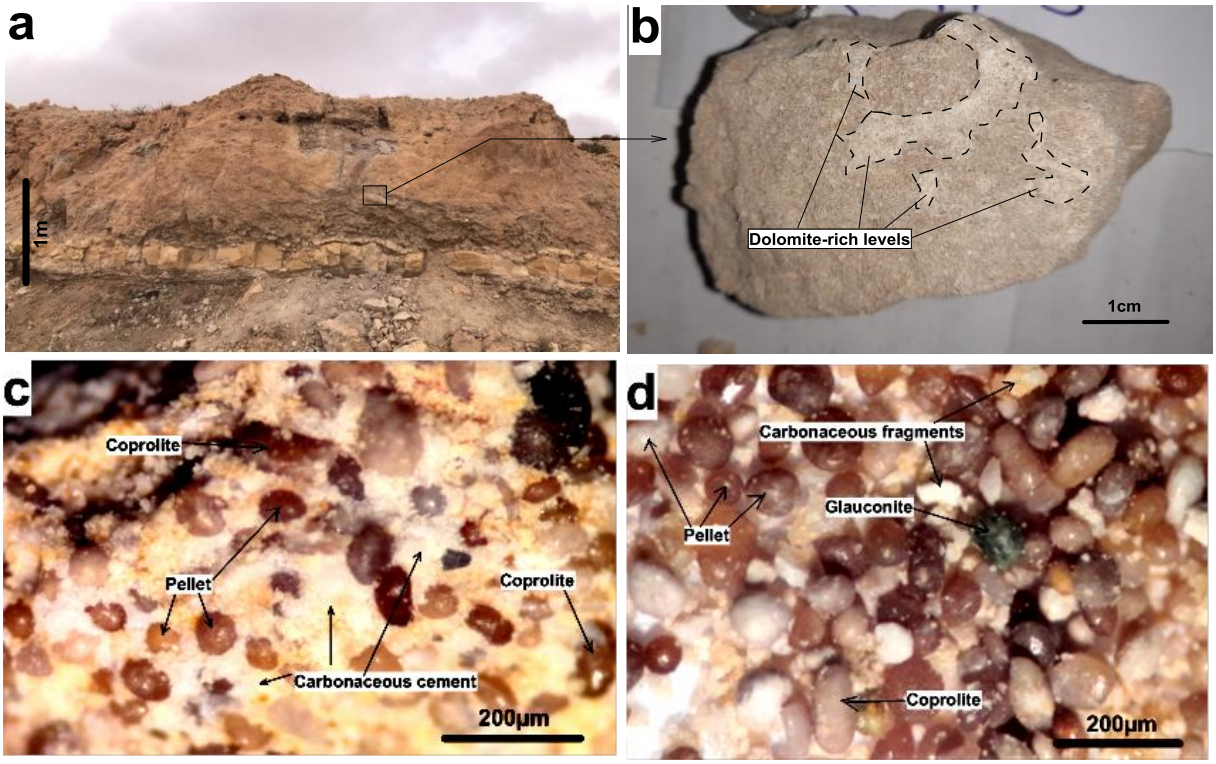

Fig. 22: (**a**) The field lower sub-layer outcrop. (**b**) Hand specimen from the lower sub-layer showing irregular centimetric levels of dolomitic material. (**c**) Magnification under the binocular microscope revealing low frequency of grains cemented by dolomitic cement. (**d**) Phosphatic particles separated from the cement/matrix.

➢ **Main sub-layer:**

The main sub-layer (Fig. 23) shows relatively homogeneous fine-grained facies. The phosphatic elements (mainly pellets and coprolites), which are more abundant in this sub-layer, are cemented by clayey to carbonaceous matrix. The clayey matrix is disply a relatively dark color of this facies (Fig. 23b), and gives the facies its relative friabile habit compared to the other two sub-layers (Fig. 23c, d).

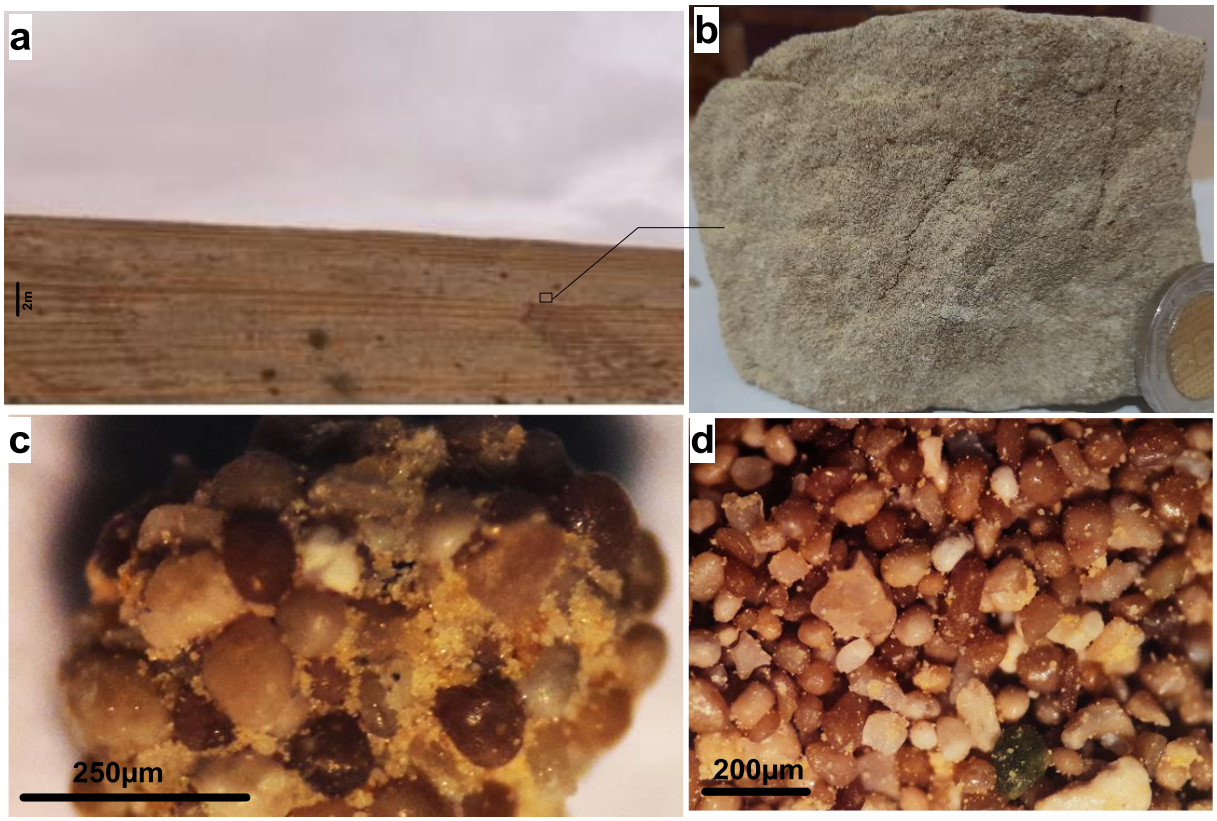

Fig. 23: (**a**) The field outcrop of the main sub-layer. (**b**) Hand specimen from the main sub-layer showing relatively dark color due to the presence of clayey matrix. (**c**) Magnification under the binocular microscope displaying high frequency of grains cemented by clayey to carbonaceous cement. (**d**) Phosphatic particles separated from the cement/matrix.

➢ **Upper sub-layer:**

The upper sub-layer (Planche 3a) looks much more like the lower sub-layer, with fine to medium-grained phosphatic mudstones, with hard, compact carbonaceous cement represented mainly by dolomite (Fig. 24) of grayish, beige, and dark gray color. This sub-layer is the poorest in phosphatic elements displaying low frequencies of grain abundance (30 to 40%) (Fig. 24c). It is also characterized by its heterogeneity with large grain-size variation (Fig. 24d).

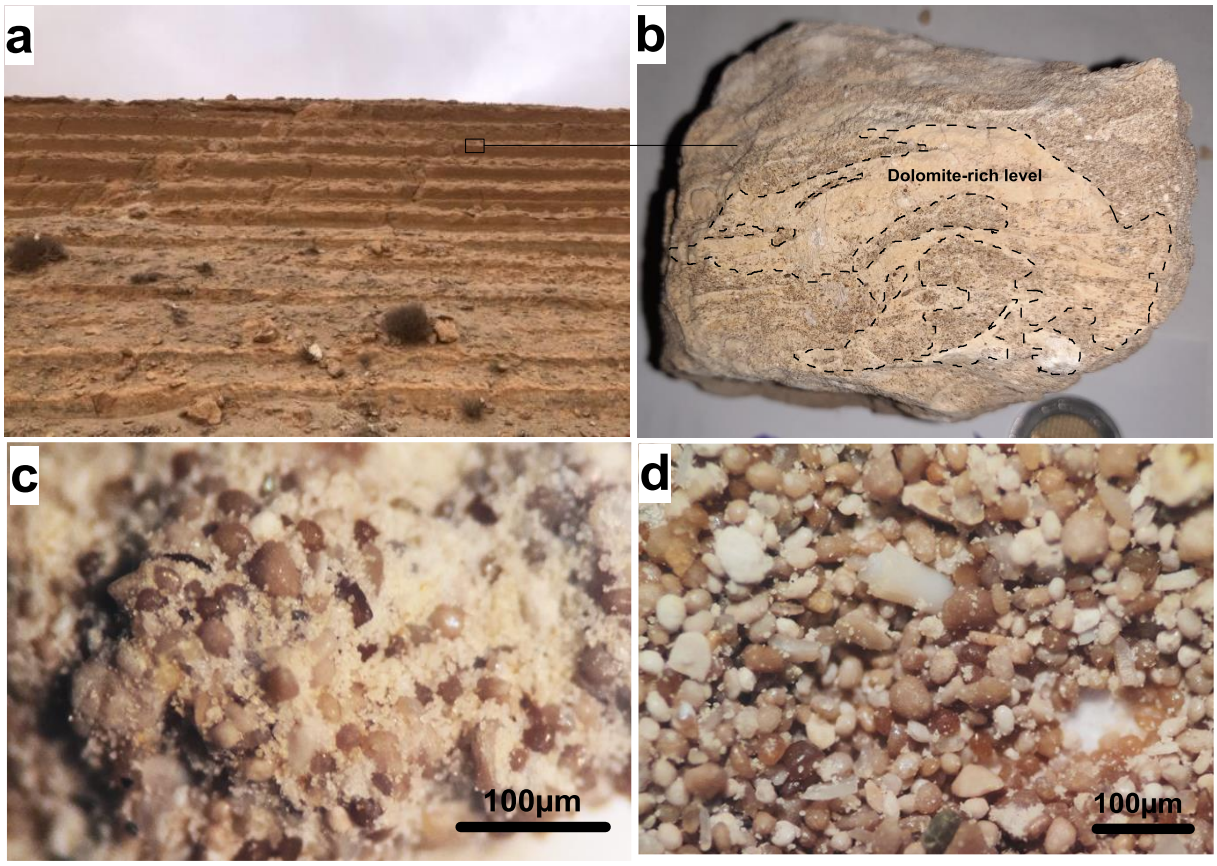

Fig. 24: (**a**) Field outcrop of the upper sub-layer. (**b**) Hand specimen of the upper sub-layer showing dolomitic-rich material. (**c**) Magnification under the binocular microscope revealing low frequency of grains cemented by carbonaceous (mainly dolomite) cement. (**d**) Phosphatic particles separated from the cement/matrix.

The Bled El Hadba phosphorite deposit is located in the Djebel Onk region, which is part of the Tebessa region within the Eastern Saharan Atlas. The Tebessa region is of great

interest for study due to its complex geology. It mainly consists of Mesozoic-Cenozoic formations and is characterized by significant tectonic activity, including Triassic uplift, subsidence, fault networks, collapse basins, and extensive folding. These tectonic processes have collectively contributed to the formation of anticlinal massifs that are oriented along the NE-SW axis, resulting in a well-defined structural complexity.

The Djebel Onk anticline exhibits formations ranging from the Cretaceous to the Quaternary, with particular emphasis on the Upper Thanetian level. This level is notable for its substantial 30-meter thick phosphorite layer, which extends seamlessly from Kef Essenoun in the west to Bled El Hadba in the east.

The geology of the Bled El Hadba deposit closely resembles that of Kef Essenoun and Djemi-Djema, with stratigraphic formations spanning from the Paleocene to the Quaternary. The upper Thanetian phosphatic layer in Bled El Hadba shares similar morphological characteristics with other primary deposits, such as Kef Essenoun and Djemi Djema. It can be divided into three distinct sub-layers: the lower sub-layer, which is characterized by high hardness and a dominance of dolomite, even reaching almost pure dolomite levels; the main sub-layer, which is relatively friable and dark due to the presence of clayey material forming the matrix/cement, along with carbonaceous material; and the upper sub-layer, which is very hard due to the compact dolomitic cement and exhibits grayish, beige, and dark gray colors.

CHAPTER III

PETROGRAPHY AND MINERALOGY OF THE BLED EL HADBA PHOSPHORITES

CHAPTER III

PETROGRAPHY AND MINERALOGY OF THE BLED EL HADBA PHOSPHORITES

The petrographic and mineralogical studies are of great value, as they enable the precise determination of both the quantities and qualities of minerals within the studied facies. Furthermore, this approach provides insights into the dispersion of these minerals among the various components within the samples. This chapter begins with a comprehensive petrographic examination of thin sections prepared from representative phosphorite samples from each phosphorite sub-layer, which is then followed by an investigation of the mineralogical studies often with the aids of X-Ray Diffractometry (XRD) method.

III.1. Petrography

III.1.1. Methodology:

The petrographic study is undertaken through the observation of prepared thin sections from phosphorite samples under an optical microscope. More than 40 thin sections were prepared at Thin Section Laboratory, Department of Geology, Badji Mokhtar University - Annaba. Given the friability of phosphorite, a specific preparation method was often necessary to prepare these thin sections. Induration of the samples became imperative to facilitate subsequent processes involving cutting, polishing, and bonding. Prior to analysis, the samples were dried in an oven set at a maximum temperature of 100°C to eliminate any moisture content present in the samples. Subsequently, the samples are meticulously impregnated with resin, drop by drop under vacuum conditions, in order to ensure the complete removal of any trapped air bubbles. In order to facilitate the hardening of the resin (and therefore the entire sample), the sample is placed on a hot plate at a temperature of approximately 80°C for a period of

approximately 1h 30 mn. Once the hardening phase is complete, the sample is ready for conventional thin section preparation procedures (sawing, polishing, gluing, and other standard operations) (Fig. 25).

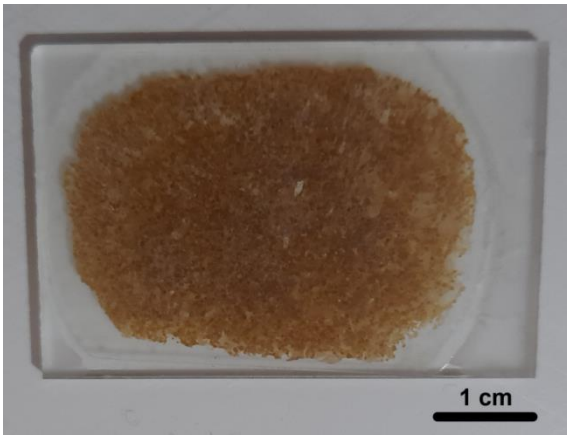

Fig. 25: example of thin section

III.1.2. Petrographic description

The petrographic analysis of phosphorites from Bled El Hadba shows relatively uniform granulometry, characterized by grain sizes ranging from 180 to 300 μm, classifying them as phospharenite facies. However, exceptions include some grains, particularly coprolites and some bioclasts, which can reach sizes of few millimeters. The following petrographic description will concentrate on the main phosphatic particles, such as pellets, coprolites, glauconites, bioclasts, intraclasts, and the cement/matrix nature. The observations under microscope use both Plane Polarized Light (**PPL**) and Crossed Polarized Light (**XPL**).

III.1.2.1. The phosphorite particles:

Pellets:

The pellets particles of the Bled El Hadba phosphorites are similar to those of the Algerian-Tunisian deposits; they are thaught to result from organic matter phosphatization as well as the fragmentation of preexisting coprolites during reworking events.

As shown in figure 26, the pellets typically exhibit sizes between 50 and 200 µm, and high degree of roundness, ranging from very well-rounded to rounded shape. However, smooth ovoid pellets are the predominant form.

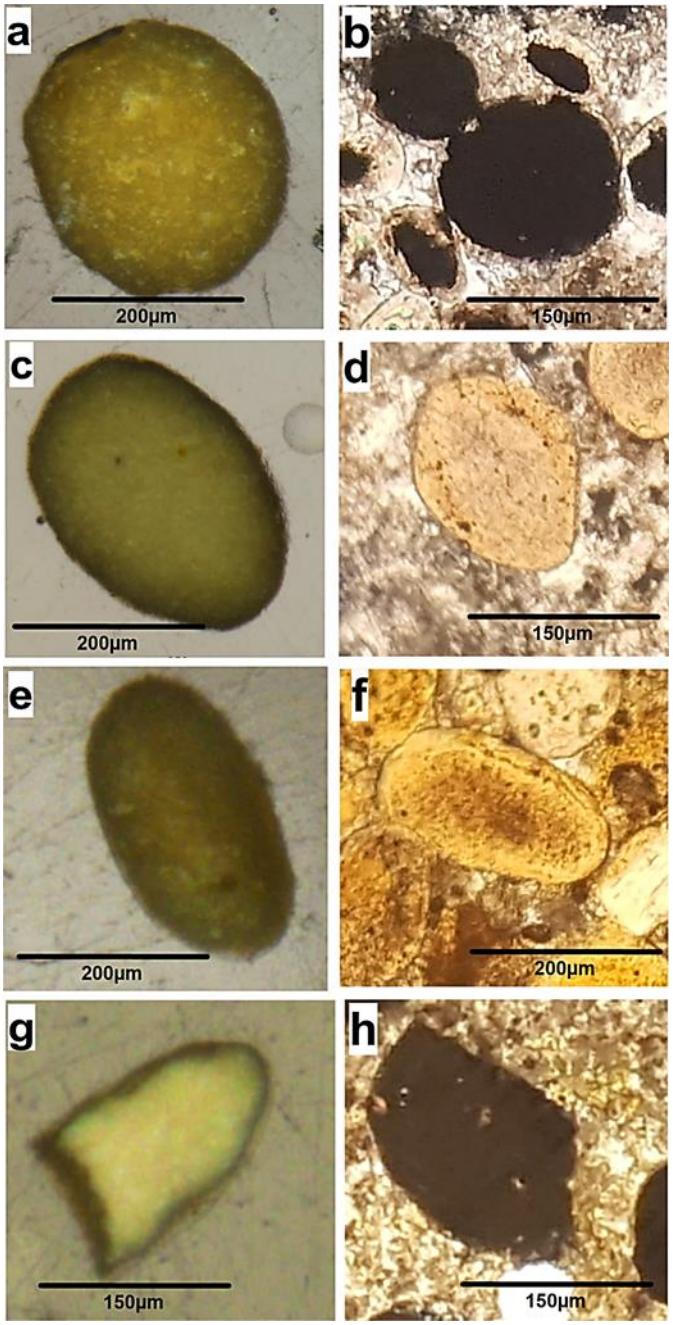

Fig. 26: Microphotographs showing different pellet shapes. (**a** and **b**) well-rounded pellet; (**c** and **d**) fairly well-rounded pellet; (**e** and **f**) rounded pellet; (**g** and **h**) irregular fragmented pellet. (Pictures in the left are for separated grains, whereas those in the right are from thin sections (b and h: PPL; d and f: XPL))

The coloration of the pellets is dependent on the presence of organic, argillaceous, or ferruginous impurities. In general, pellets exhibit a range of colours, including dark, brown, and even greenish (Fig. 27).

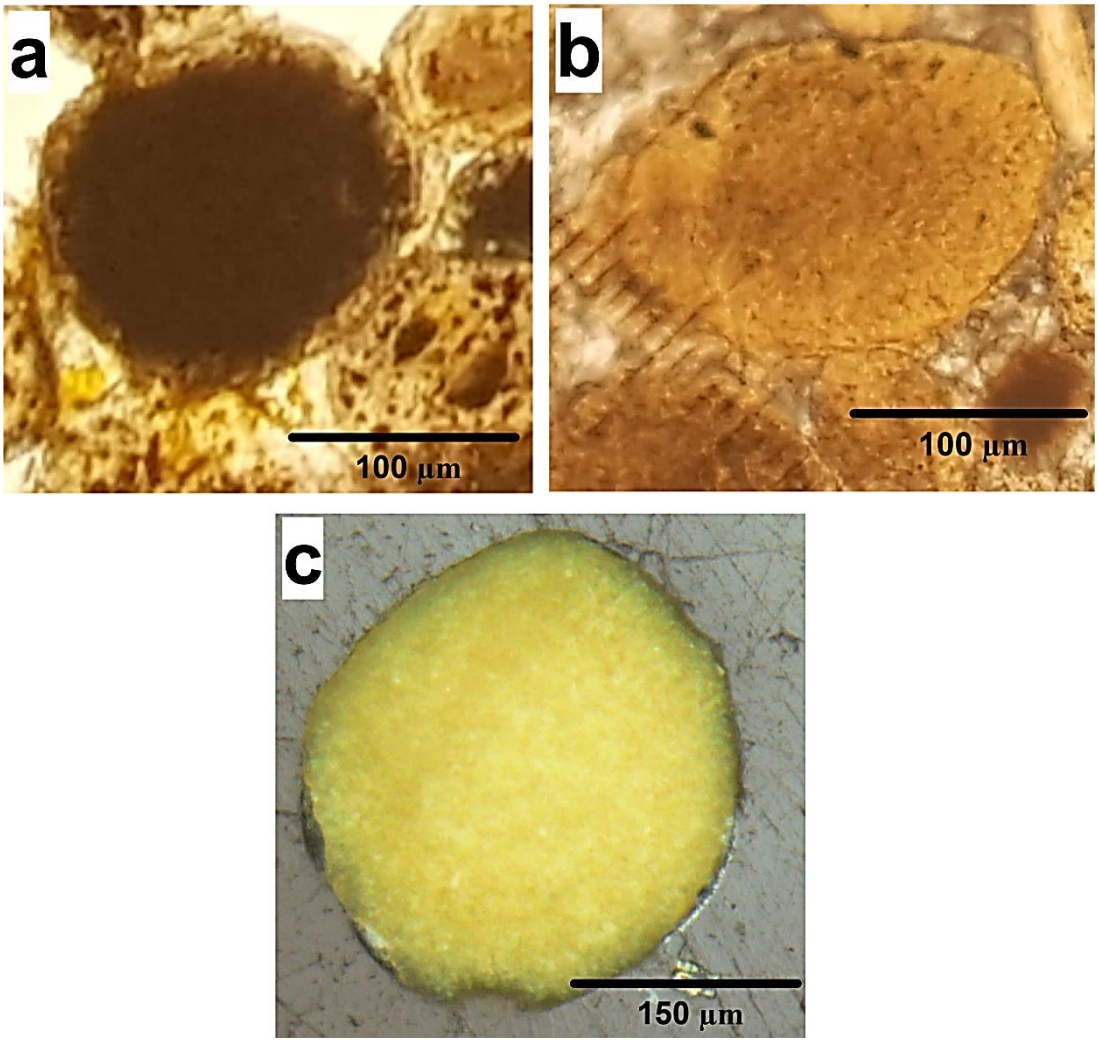

Fig. 27: Microphotographs under PPL microscope showing the colors of pellets (**a**) dark and (**b**) brownish pellet (thin section observation); and (**c**) greenish pellet (separated particle).

Some pellets show an angular silt-sized quartz nucleus and a concentric phosphatic matter; these are often called pseudo-oolitic particles (Fig. 28b). In addition, they often include organic, argillaceous, crystalline (apatite) and bioclastic material (Fig. 28a).

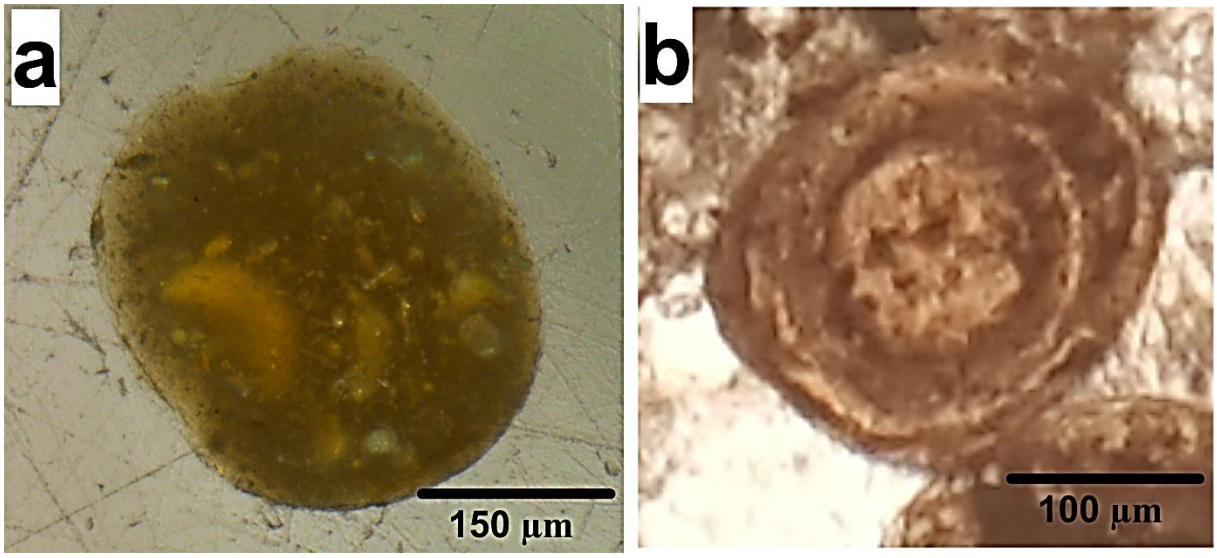

Fig. 28: Microphographs under PPL microscope showing (**a**) Pellet containing various materials. (**b**) Pellet showing concentric structure (pseudo-oolite).

Organic matter is a common component of the pellets. It may be found in different forms: (1) filling the majority of the particle; (2) randomly scattered as patches; (3) in concentric layers; or (4) concentrated in the central part of the pellet. (Figs. 29a-d).

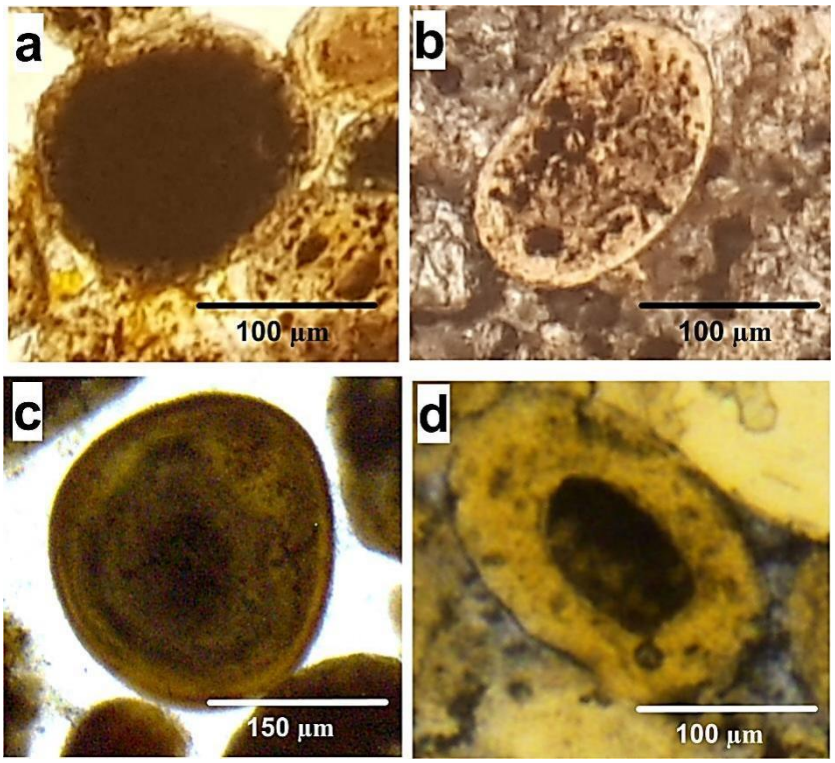

Fig. 29: Microphotographs under PPL microscope showing distribution of organic matter in pellets. (**a**) filling the particle; (**b**) randomly scattered as patches; (**c**) in concentric layers; (**d**) concentrated in the center.

Some pellets may show an aspect of glauconite particle by the green color around their rims, indicating the glauconitization process which is known to be developed from the rim to the core of the particles (Fig. 30).

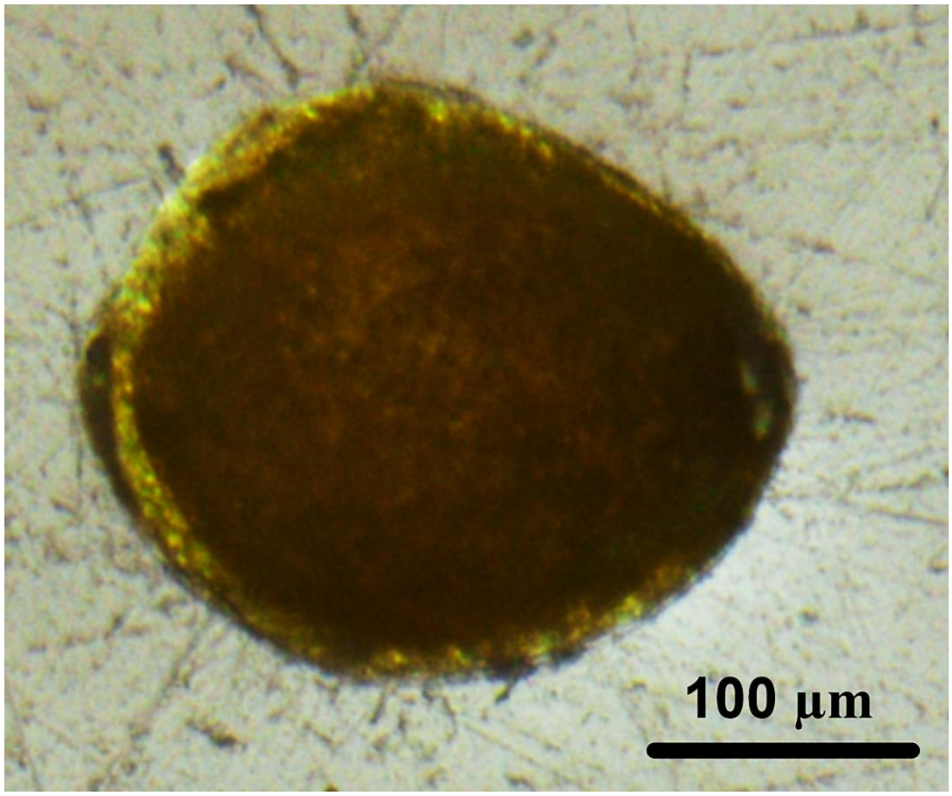

Fig. 30: Microphotograph of separated pellet desplaying glauconitization process at the rims.

Coprolites:

Coprolites typically exhibit cylindrical to irregular shapes, with colors ranging from white, brown to grey (Fig. 31a-c) and varying in size from 500 µm to several millimeters (Fig. 31d, e).

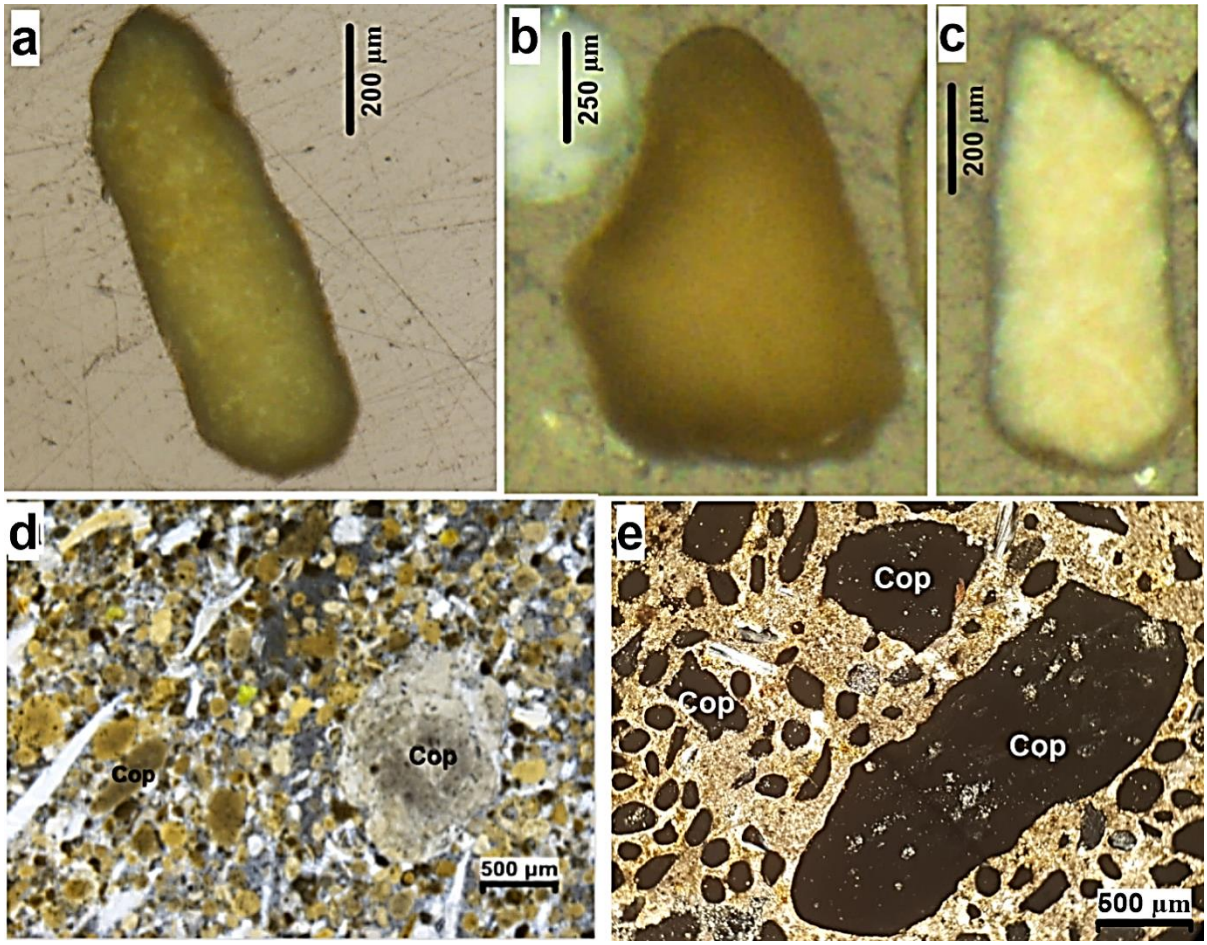

Fig. 31: Microphotographs of coprolite habits: (**a**) separated cylindrical coprolite; (**b**) separated irregular brownish coprolite; (**c**) separated whitish coprolite; (**d**) and (**e**) thin sections showing coprolite size varying from 500 µm to few millimeters (**d**: PPL; **e**: XPL).

Coprolites frequently contain inclusions, such as organic matter, apatite crysts, carbonaceous materials (mainly dolomite or/and calcite), siliceous minerals, and fragments of glauconite (green color within coprolite) (Fig. 32a, b). These inclusions may originate from the remains of fossilized siliceous tests and the precipitation of dissolved silica. Similar to pellets, the coprolites often show glauconitization processes, mainly at the particles' rims. This phenomenon is observed through the development of the green color from the rim to the core (Fig. 33).

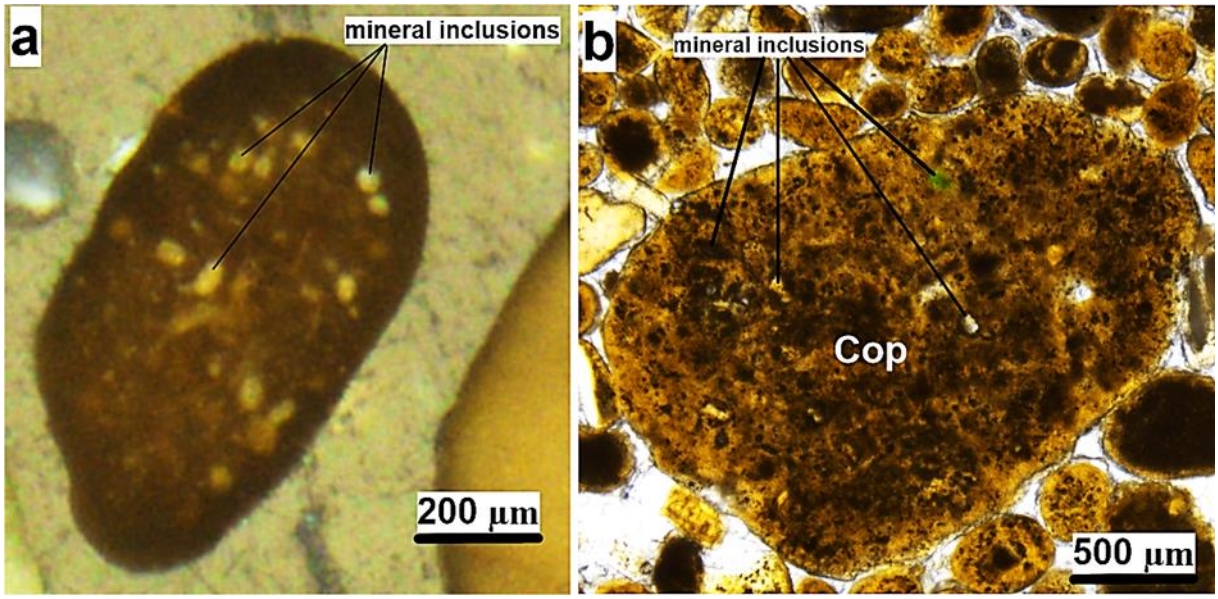

Fig. 32: Microphotographs of coprolites displaying various types of inclusions. (**a**) separated coprolite with mineral inclusions; (**b**): inclusions within coprolite from thin section observation under plane polarized light (PPL).

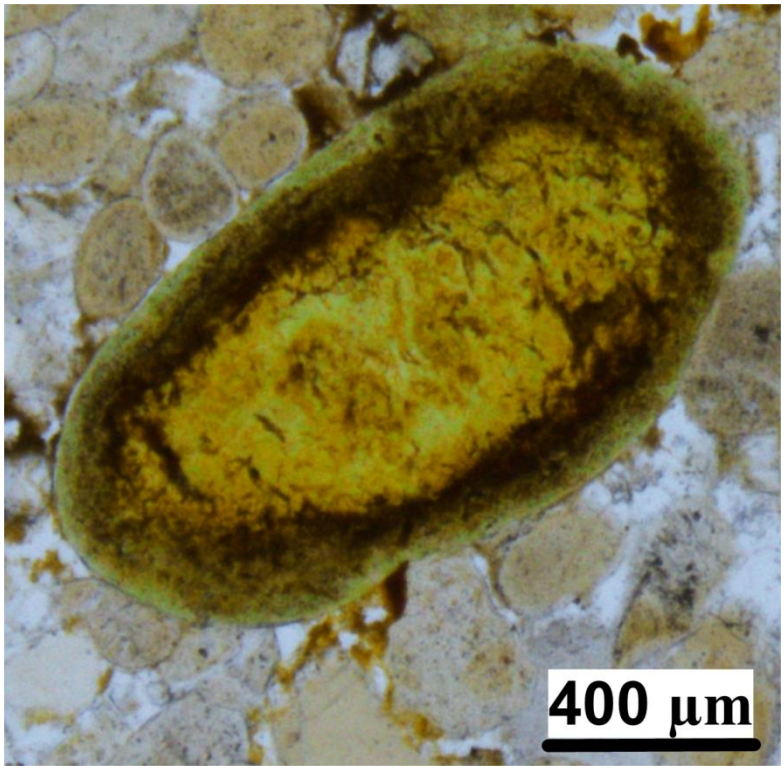

Fig. 33: Microphotograph under plane polarized light (PPL) of coprolite showing developement glauconitization process from the rim to the core of the particle.

Glauconites:

Glauconites are readily distinguished by their distinctive green colour. The argillaceous particles exhibit a diverse range of shapes, spanning from rounded to irregular (Fig. 34a-c), with sizes typically ranging from 300 μm to a few millimeters in some cases. Unlike pellets and coprolites, glauconites often contain a number of inclusions, which are most likely inherited from the original non-phosphatized particles (Fig. 34d).

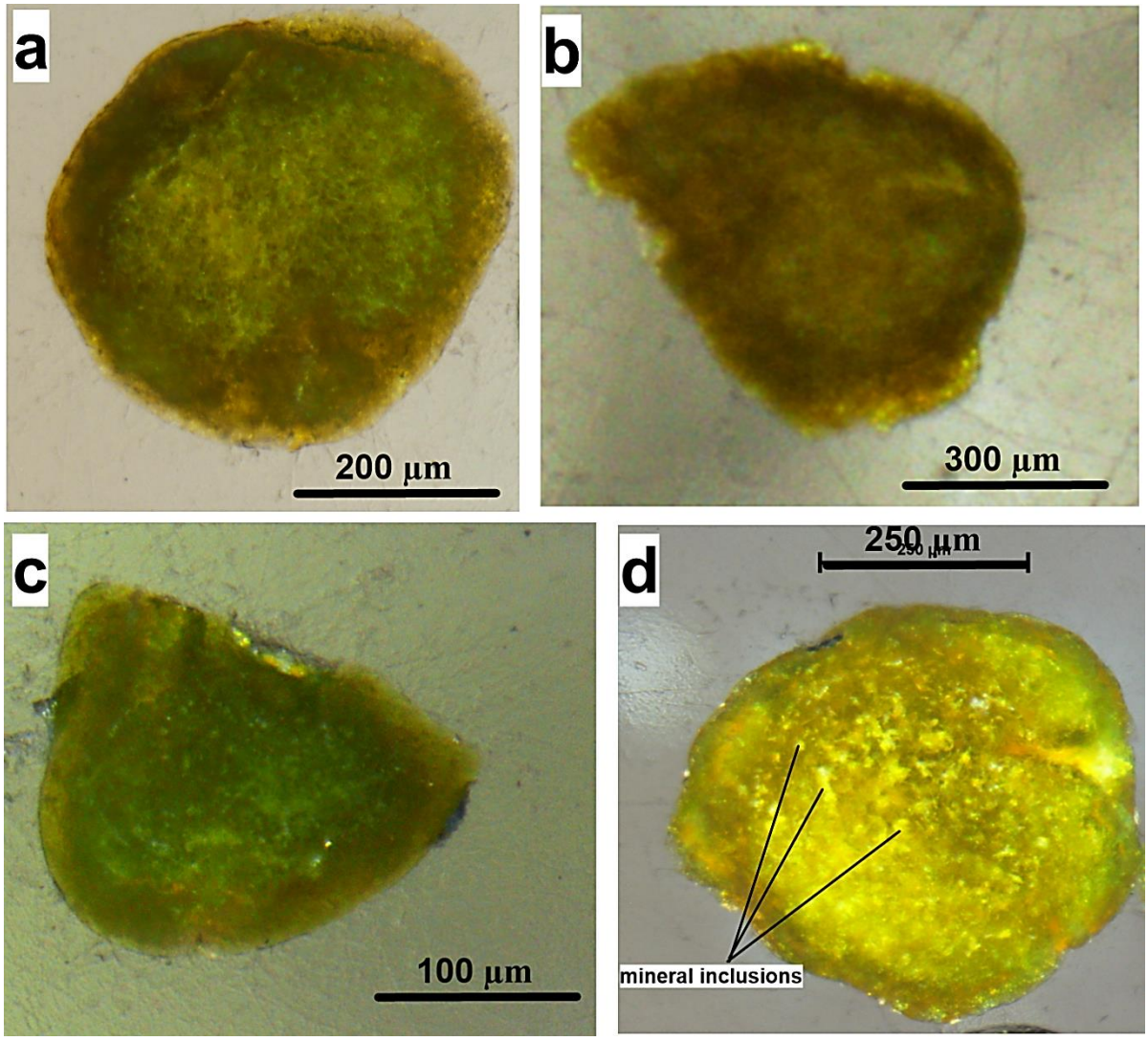

Fig. 34: Microphotographs of separated glauconite particles showing well rounded (**a**), Irregular (**b**), fragment-like (**c**) shapes; (**d**) glauconite containing various inclusions.

Glauconites are randomly distributed throughout the facies, but their abundance is considerably lower than that of pellets and coprolites. They typically comprise no more than 3 to 4% of the total phosphorite particles (Fig. 35a-c).

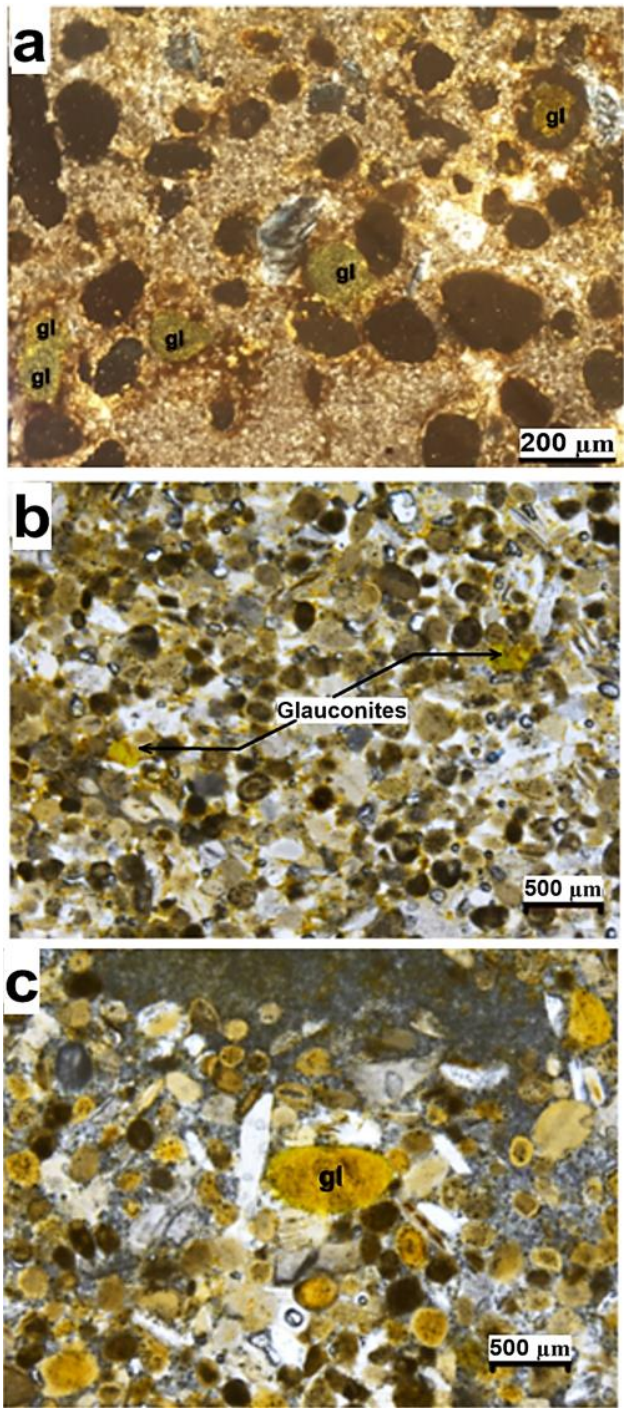

Fig. 35: Microphotographs crossed-polarized light (XPL) showing glauconite particles (gl) in thin sections: (**a**) glauconites with relatively high abundances in wackestone texture; (**b**) glauconites in packestone texture with size < 200 µm; (**c**) glauconite with relative high size (> 500 µm).

Bioclasts and intraclasts:

The main components of bioclasts are fish teeth, bones, and lamellibranch fragments. A wide range of sizes is observed, with specimens measuring from 500 µm to several centimeters. This is particularly observed in the case of fish teeth (Fig. 36a-d).

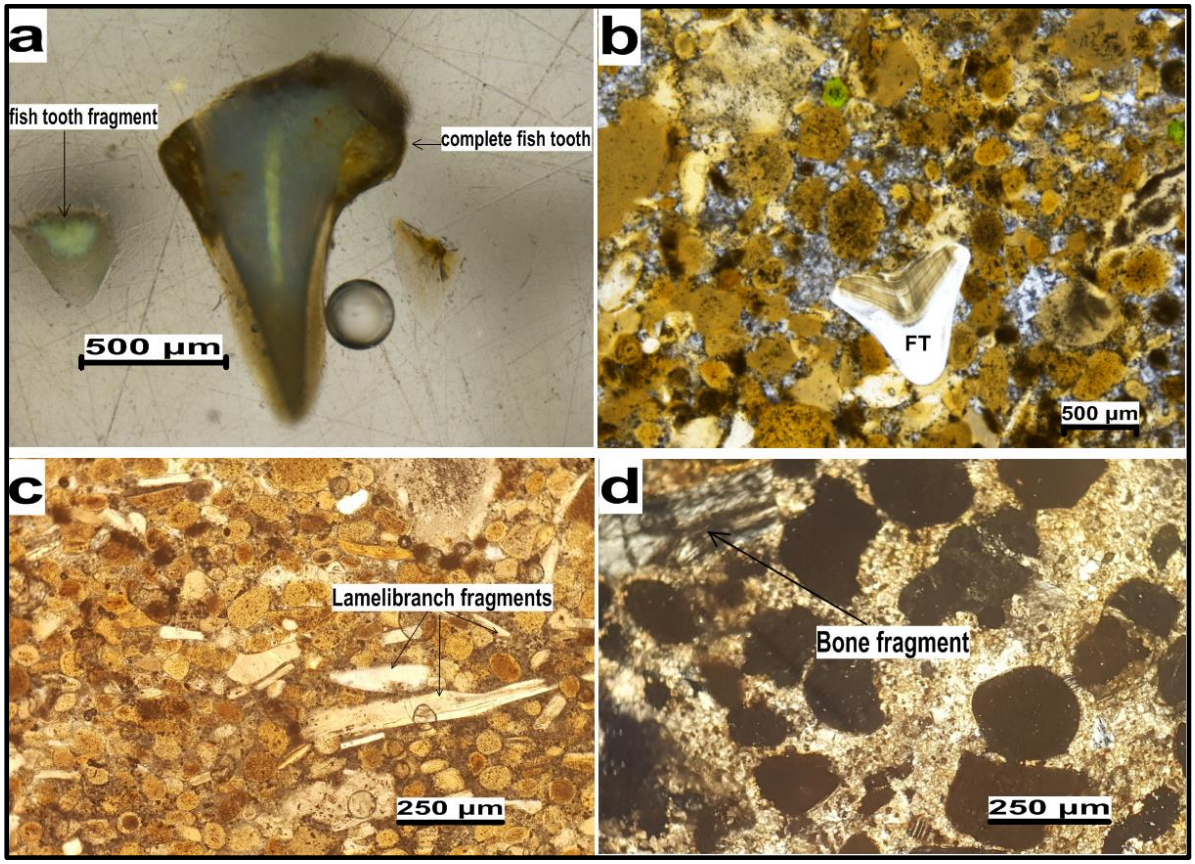

Fig. 36: Microphotographs showing the main types of bioclasts in the studied phosphorites: (**a**) fish teeth in complete and fragment form (PPL), (**b**) fish tooth (FT) along with coexisting phosphatic particles observed in thin section (PPL), (**c**) Lamellibranch fragments (PPL), (**d**) bone fragment (XPL).

The main intraclasts observed within the Bled El Hadba phosphorites are siliceous materials that may exist in two aspects: amorphous silica, represented by opal-CT; and crystalline silica represented by quartz grains (Fig. 37a, b). The siliceous material may be originated from (1) fragmented fossils of siliceous tests, (2) precipitated silica, or (3) quartz detrital grains.

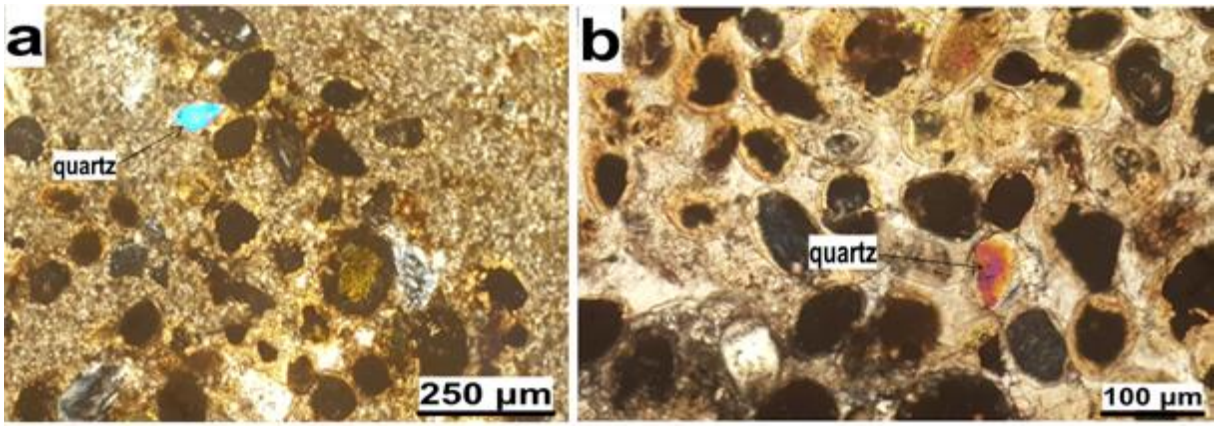

Fig. 37: Microphotographs under XPL microscope showing quartz grains with phosphatic paricles.

Iron oxides:

The occurence of iron hydroxides is rarely observed. It is predominantly located within the microcracks and interstitial between the phosphatic particles (Fig. 38a, b). This may be attributed to the post deposition oxidation of iron-rich material.

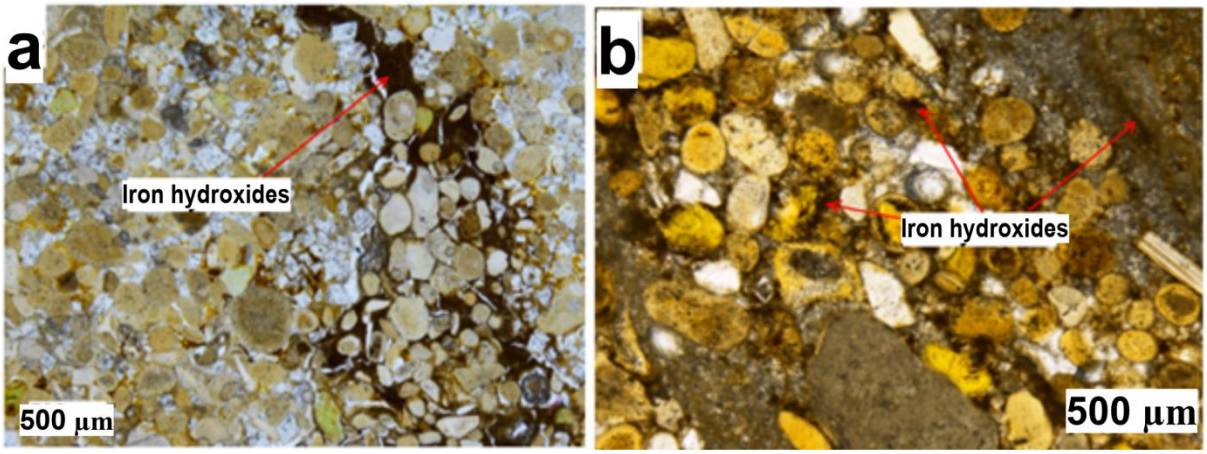

Fig. 38: Microphotographs under PPL microscope (**a** and **b**) showing hydroxides occupying microcracks and interstitial position.

Matrix/Cement:

The matrix is composed of extremely fine clayey material, typically measuring less than 4 µm, which shows a dark color (Fig. 39a, b). The prevalence of this clayey matrix causes friability habit of the phosphatic rocks.

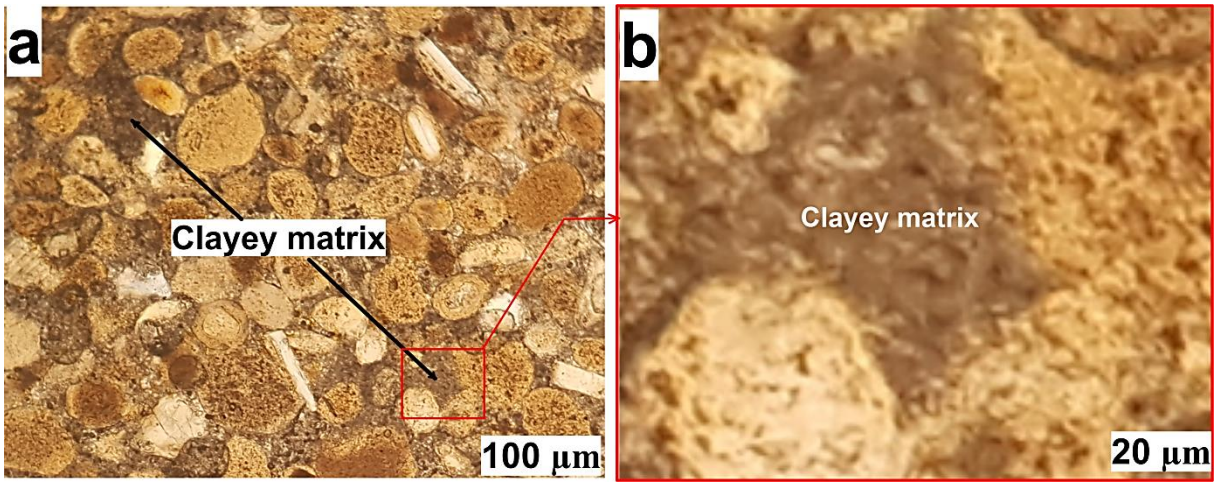

Fig. 39: Microphotographs under PPL microscope showing the clayey matrix in (**a**) small scale and (**b**) big scale.

The cement may also be composed of sparitic microcrystalline carbonaceous material, which is typically calcite and/or dolomite, with sizes exceeding 5 µm (Fig. 40a, b). This specific type of cement plays a significant role in determining the hardness characteristics exhibited by the facies.

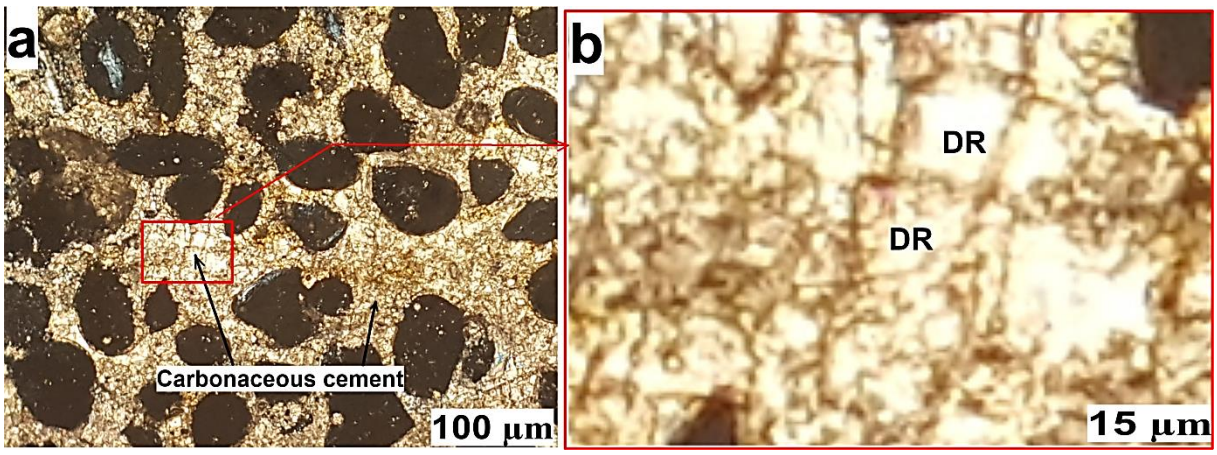

Fig. 40: Microphotographs under XPL microscope showing the carbonaceous cement in (**a**) small scale and (**b**) big scale. (DR: euherdral dolomite).

III.1.2.2. The phosphorite sub-layers:

The petrographic investigation, which focused on the observations of individual phosphatic sub-layers (LL, ML, and UL), revealed that their distinctions were based first on

the varying abundances of phosphatic particles, and hence P_2O_5 contents, and second on the nature of the matrix.

The petrographic characteristics of these sub-layers are as follows:

Lower sub-layer:

The lower sub-layer (LL) is distinguished by a fine-grained texture, with particles ranging in size from 100 to 200 µm. It is recognized by its hardness. Phosphatic particles, which constitute up to 75% of the rock, are cemented by calcareous, dolomitic, and/or silicic matrix (Fig. 41a). The composition includes pellets, glauconites, bioclasts, and pseudo-oolites with diameters between 100 and 200 µm, while coprolite grains can be as large as 500 µm (Fig. 41a and b).

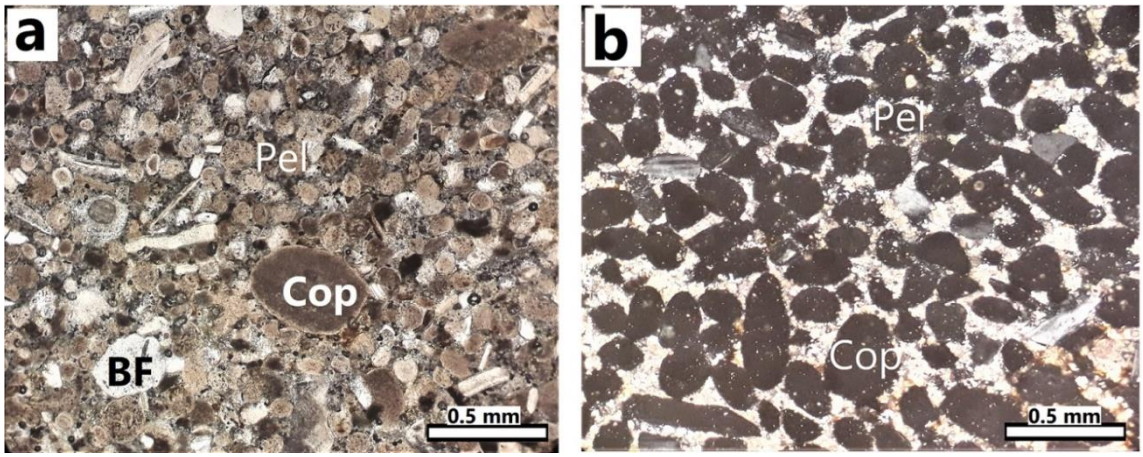

Fig. 41: Microphotographs (a: under PPL, and b: under XPL) showing the aspect of the lower phosphorite sub-layer (LL). Cop: coprolite, Pel: pellet, Gl: glauconite, BF: bone fragment, Qz: quartz.

Main sub-layer:

The main sub-layer (ML) is characterised by a larger grain size and phosphatic particle abundances that are comparable to those observed in the lower sub-layer (ranging from 75 to 85%). However, it is characterized by a clayey to calcareous cement (Fig. 42a), and therefore is more friable than the other phosphorite layers. The particles, including pellets, glauconites, bioclasts, and pseudo-oolites, have an approximate size of 200 µm, while coprolites can reach 1 to 2 mm in diameter (Fig. 42a and b).

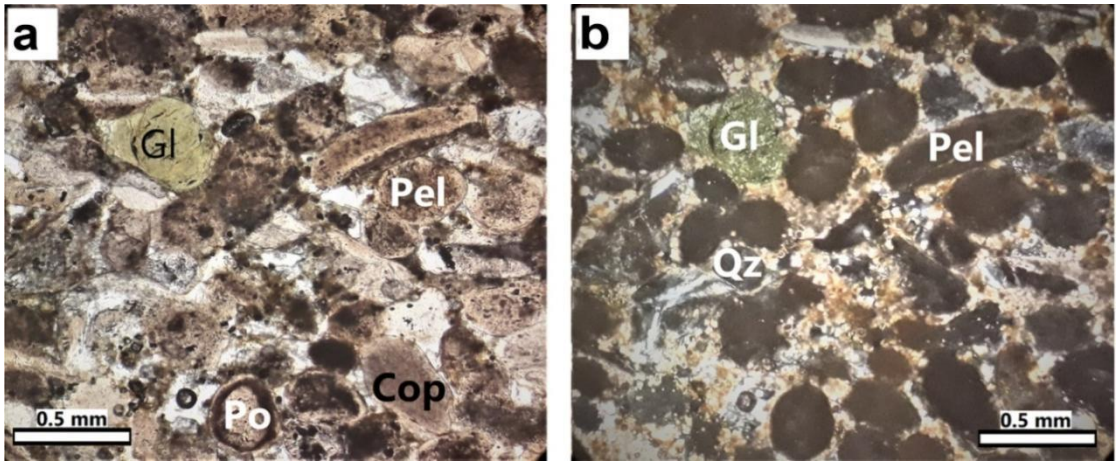

Fig. 42: Microphotographs (a: under PPL, and b: under XPL) of the phosphorite main sub-layer (ML). Cop: coprolite, Pel: pellet, Gl: glauconite, Qz: quartz.

Upper sub-layer:

The upper sub-layer (UL) exhibits a markedly lower abundance of phosphatic particles, comprising between 30 to 40% of the rock. It is distinguished by greater hardness, attributed to the high percentage of dolomitic and calcitic cement, which constitutes 60 to 70% of the rock. The phosphatic particles in this sub-layer exhibit a relatively coarse and heterogeneous grain size, with an average diameter of approximately 100 to 500 μm (Fig. 43a and b). This sub-layer is also characterised by a greater prevalence of glauconite minerals, and lower abundance of bioclasts.

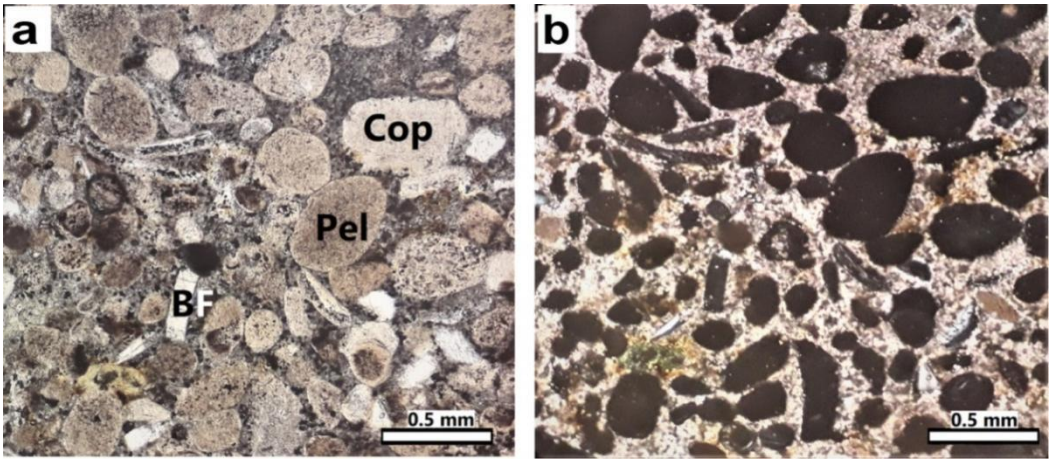

Fig. 43: Microphotographs (a: under PPL, and b; under XPL) of the phosphorite upper sub-layer (UL). Cop: coprolite, Pel: pellet, BF: bone fragment.

III.2. Mineralogy:

III.2.1. Methodology:

For the detailed mineralogical study, X-Ray diffraction (XRD) analysis was used. Powdered representative samples from each sub-layer were prepared for analysis to better characterize the mineralogical composition. These analyses were carried out at the Faculty of Science, El Manar University, Tunisia. The analysis was performed using a CPS 120 INEL XRD powder diffractometer with a CuKα radiation source, a wavelength λ of 1.5418 Å, and an acceleration voltage of 40 kV. Data collection spanned from 4° to 70° 2θ, and mineral phases were identified with the assistance of the X'Pert HighScorePlus software package (PANalytical_2004) and PDF-2 (2004) Data base.

3. 2. Results and interpretations:

The results of XRD applied on each sub-layer are as follows:

Lower sub-layer (LL):

Representative samples from the lower sub-layer gave the following results (fig. 44a):

- **Main minerals:**
  - Dolomite (Ca Mg $(CO_3)_2$)
  - Apatite group:
    - Carbonate Fluorapatite ($Ca_5(PO_4,CO_3)_3F$)
    - Fluorapatite ($Ca_5(PO_4)_3F$)
    - Hydroxylapatite ($Ca_5(PO_4)_3(OH)$)
- **Accessory minerals:**
  - Quartz (SiO_2)
  - Calcite ($CaCO_3$)
  - Gypsum ($CaSO_4,2H_2O$)

Main sub-layer (ML):

Representative samples from the main sub-layer gave the following results (fig. 44b):

- **Main minerals:**
  - Dolomite (Ca Mg $(CO_3)_2$)
  - Apatite group:
    - Fluorapatite ($Ca_5(PO_4)_3F$)
    - Hydroxylapatite ($Ca_5(PO_4)_3(OH)$)
- **Accessory minerals:**
  - Quartz (SiO_2)
  - Calcite ($CaCO_3$)
  - Gypsum ($CaSO_4,2H_2O$)
  - Pyrite (FeS_2)

Upper sub-layer (UL):

Representative samples from the upper sub-layer gave the following results (fig. 44c):

- **Main minerals:**
  - Dolomite (Ca Mg $(CO_3)_2$)
  - Apatite group:
    - Carbonate Fluorapatite ($Ca_5(PO_4,CO_3)_3F$)
    - Fluorapatite ($Ca_5(PO_4)_3F$)
    - Hydroxylapatite ($Ca_5(PO_4)_3(OH)$)
- **Accessory minerals:**
  - Quartz (SiO2)
  - Calcite (CaCO3)

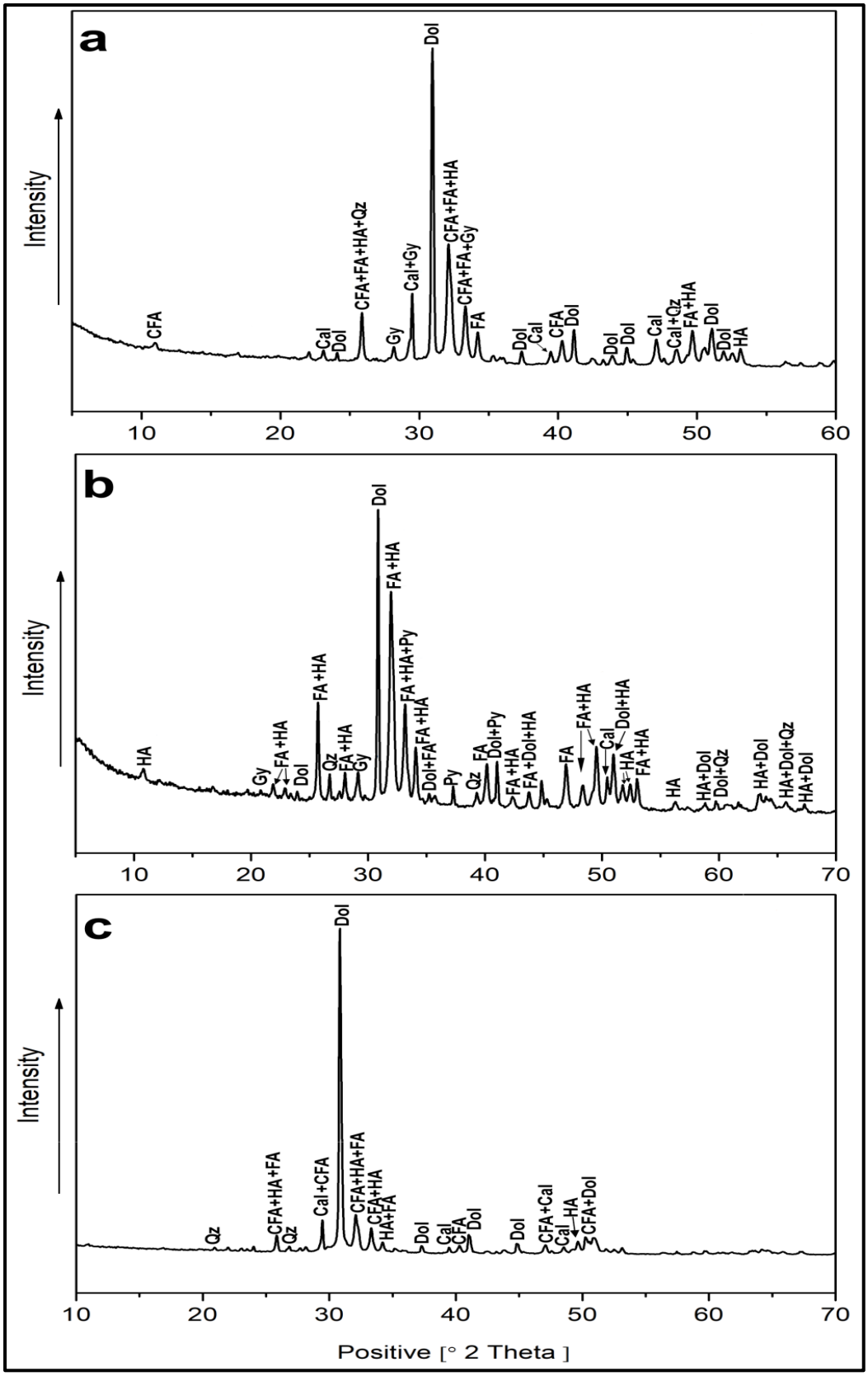

Fig. 44: XRD results of samples from lower (a), main (b) and upper (c) sub-layers. (CFA: Carbonate Fluor-Apatite; FA: Fluor-Apatite; HA: Hydroxyl-Apatite; Dol: Dolomite; Cal: Calcite; Gy: Gypsum; Qz: Quartz; Py: Pyrite)

The interpretation of the XRD results leads to the following conclusions: the apatite group (carbonate fluorapatite, fluorapatite, and hydroxylapatite) and dolomite emerge as the primary minerals across all three sub-layers. Meanwhile, calcite, quartz, and gypsum are present in smaller quantities. In addition, traces of pyrite are marked in the main sub-layer. The carbonate-fluorapatite, fluorapatite and hydroxylapatite are associated with distinct phosphatic particles, mainly pellets and coprolites, whereas dolomite, calcite, gypsum, and quartz constitute the matrix minerals, with dolomite exhibiting a notably higher dominance.

In concusion, the Bled El Hadba phosphorite samples reveal a diverse particles, including pellets, coprolites, glauconites, and bioclasts represented by bone and lamellibranch fragments. Additionally, intraclasts, such as quartz and some carbonate fragments (calcite and dolomite), are observed.

The composition of the matrix/cement predominantly comprises dolomite, particularly noticeable in the lower and upper sub-layers. In the main sub-layer, the dolomitic cement coexists with clayey material, contributing to the relative friability of this facies.

A higher abundance of pellets, coprolites, and glauconites is observed in the main sub-layer. Conversely, lower sub-layer and, notably, upper sub-layer exhibit lower grain frequencies, with a prevalence of dolomite. The highest abundance of glauconites is notably observed in the upper sub-layer.

The mineralogical analysis conducted on samples from the three phosphatic sub-layers of the Bled El Hadba deposit, using XRD method, identified the main minerals as carbonate

fluorapatite, fluorapatite, hydroxylapatite and dolomite. Calcite, gypsum, and quartz were found as minor constituents within the matrix.

Notably, the main sub-layer exhibits a higher concentration of apatite minerals (fluorapatite and hydroxylapatite) compared to the lower and upper sub-layers, which are predominantly characterized by the dominance of dolomite. Additionaly, the main sub-layer marks the presence of pyrite traces which are absent in the lower and upper sub-layers.

CHAPTER IV

GEOCHEMISTRY OF THE BLED EL HADBA PHOSPHORITES

CHAPTER IV

GEOCHEMISTRY OF THE BLED EL HADBA PHOSPHORITES

The geochemical exploration of Algerian phosphorites has been the focus of numerous investigations conducted by various researchers. These studies predominantly concentrated on major and trace elements, as evidenced by the works of Chabou-Mostfai (1987), Cielensky and Benchernine (1987), Daas-amiour (2012) as examples. However, in-depth and comprehensive geochemical analyses, specifically targeting Algerian phosphorites, started with the work of Kechiched et al. (2016) which was focused on the phosphorites located in the northern Tebessa region. This fundamental study provided insights into major, trace, and rare earth elements within these phosphorites. Subsequent research investigations have been extended to cover both the northern basin (El Kouif, Dyr, Tazbant) and southern basin (Kef Essenoun) phosphorite deposits in order to better understand the geochemical features of these Algerian phosphorites, in terms of their P_2O_5 contents and REE enrichment, as well as the paleoenvironmental conditions for their deposition (Kechiched et al., 2018, 2020; Ferhaoui et al., 2022; Kechiched et al., 2024; Diab et al., 2024).

In this chapter, we aim to give more results on geochemical analysis of the giant Bled El Hadba phosphorite deposit. Our focus will encompass a comprehensive study encompassing major, trace, and rare earth elements (REEs), offering insights into the environmental dynamics and deposition conditions. This study uses a dual approach, incorporating whole rock chemistry involving major and selected trace elements on one hand, and on the other hand the analysis of phosphorite particles, encompassing major, trace, and rare earth elements, thereby providing a better understanding through grain-level investigations. This approach is intended to provide a thorough understanding of the chemical image and its implications for the Bled El Hadba phosphorite deposit.

IV.1. Whole rock chemistry

IV.1.1. Methodology:

The three phosphatic sub-layers (upper, main, and lower sub-layers) of the Bled El Hadba deposit were sampled for chemical analyses. These comprise nine samples distributed from the bottom to the top of the phosphorite layer and including the three sub-layers (LL, ML, and UL; cf. Fig. 20). Powders of whole-rock samples were generated for the analysis of both major and trace elements. These were carried out at the the Mineralogical Laboratory, Faculty of Sciences, Sfax University, Tunisia. After being finely crushed, the samples were overnight steamed at 50°C. The powders were then recovered inside 32 mm-diameter plastic XRF double-ended cups, one end of which had previously been covered with a thin, replaceable polypropylene film (TF-240-255). A Thermo Scientific Niton FXL FM-XRF analyzer was employed for the XRF analyses, characterized by a 50 kV, 200 μA x-ray tube and the incorporation of CDD GOLDD drift detector technology. This uses a mining programme that permits the examination of 38 elements (Cu, Ni, Mo, Ag, Zr, Nb, Th, Y, Rb, Bi, Sr, U, As, Si, Cl, S, Mg, Au, Se, Hg, Ga, Pb, W, Sb, Sn, Cd, Co, Zn, Mn ,Fe, V, Cr, Ca,Ti, Ba, K, P, Al) and produces elemental results quickly and reliably (1-3 mn/sample). The calibration of major elements, such as calcium and phosphorus, was conducted with the use of phosphate standards from Morocco (Bcr32) and Tunisia (OTC from Oued Theldja, Metlaoui).

IV.1.2. Results and interpretation:

The chemical composition data of the whole-rock samples, including major and trace elements, are given in Table 2 and illustrated in figure 45.

Within the Bled El Hadba phosphorites, the main sub-layer exhibits the highest P_2O_5 content, ranging from 22.11 to 23.98 wt%, in contrast to the lower and upper sub-layers (11.78–18.97 wt% and 10.60–15.60 wt%, respectively). Nevertheless, these values are notably lower

than those observed in the Kef Essenoun and El Kouif phosphorite deposits situated further north (27.93–34.25 wt% and 22.95–35.00 wt%, respectively; (Kechiched et al., 2020; Ferhaoui et al., 2022; Kechiched et al., 2024)). Conversely, the whole-rock phosphorites exhibit high CaO concentrations ranging from 43.78 to 49.36 wt%. While these CaO concentrations are comparable to numerous phosphorite deposits in North Africa (Buccione et al., 2021), the CaO/P_2O_5 ratios are significantly higher (1.98 to 4.39) compared to the northern deposits, where Kechiched et al. (2020) reported ratios ranging from 1.4 to 2.7. This discrepancy is likely attributed to the calcareous-enriched cement present in the Bled El Hadba phosphorites. Authors suggest that high ratios are indicative of low phosphorite quality. Trace elements, such as Sr, Y, Cr, and V, exhibit high contents, similar to those observed in the northern phosphorites (e.g., Kef Essenoun and El Kouif; Kechiched et al., 2020).

Table 2: Major and trace element data of whole-rock analysis of Bled El Hadba phosphorites.

Sample No	Bh1	Bh2	Bh3	Bh4	Bh6	Bh7	Bh8	Bh9
	Lower sub-layer			Main sub-layer		Upper sub-layer		
Major oxides (wt.%)								
SiO_2	4.77	3.27	3.53	5.26	4.63	3.93	6.91	4.42
TiO_2	0.03	0.02	0.02	0.04	0.02	0.02	0.05	0.03
Al_2O_3	1.04	0.75	0.83	1.51	1.24	1.08	1.82	1.00
$Fe_2O_{3(t)}$	0.27	0.25	0.35	0.59	0.49	0.41	0.56	0.56
MgO	2.25	4.48	5.82	3.91	3.42	5.29	5.63	3.21
CaO	49.36	46.81	47.60	45.99	47.44	47.53	43.78	46.58
K_2O	0.09	0.12	0.13	0.45	0.44	0.42	0.66	0.38
P_2O_5	15.34	18.97	11.78	22.11	23.98	15.60	12.21	10.60
CaO/P_2O_5	3.22	2.47	4.04	2.08	1.98	3.05	3.59	4.39
Trace elements (ppm)								
Th	9.86	10.1	4.44	11.62	10.07	5.73	6.73	3.57
Zr	39.94	52.05	35.06	57.94	59.13	42.61	44.91	33.74
Y	126.37	161.28	99	187.39	180.26	115.85	134.86	81.18
Sr	1251.39	1576.93	1054.66	1814.52	1912.39	1551.52	1432.11	924.22
U	33.41	48.78	37.9	51.78	53.54	51.49	44.57	36.62
Zn	147.87	171.04	164.82	113.62	80.27	54.91	69.56	130.12
Cr	183.64	298.78	210.32	319.51	298.37	176.5	241.31	138.15
V	42.41	65.57	133.35	112.78	80.87	115.81	113.48	186.85

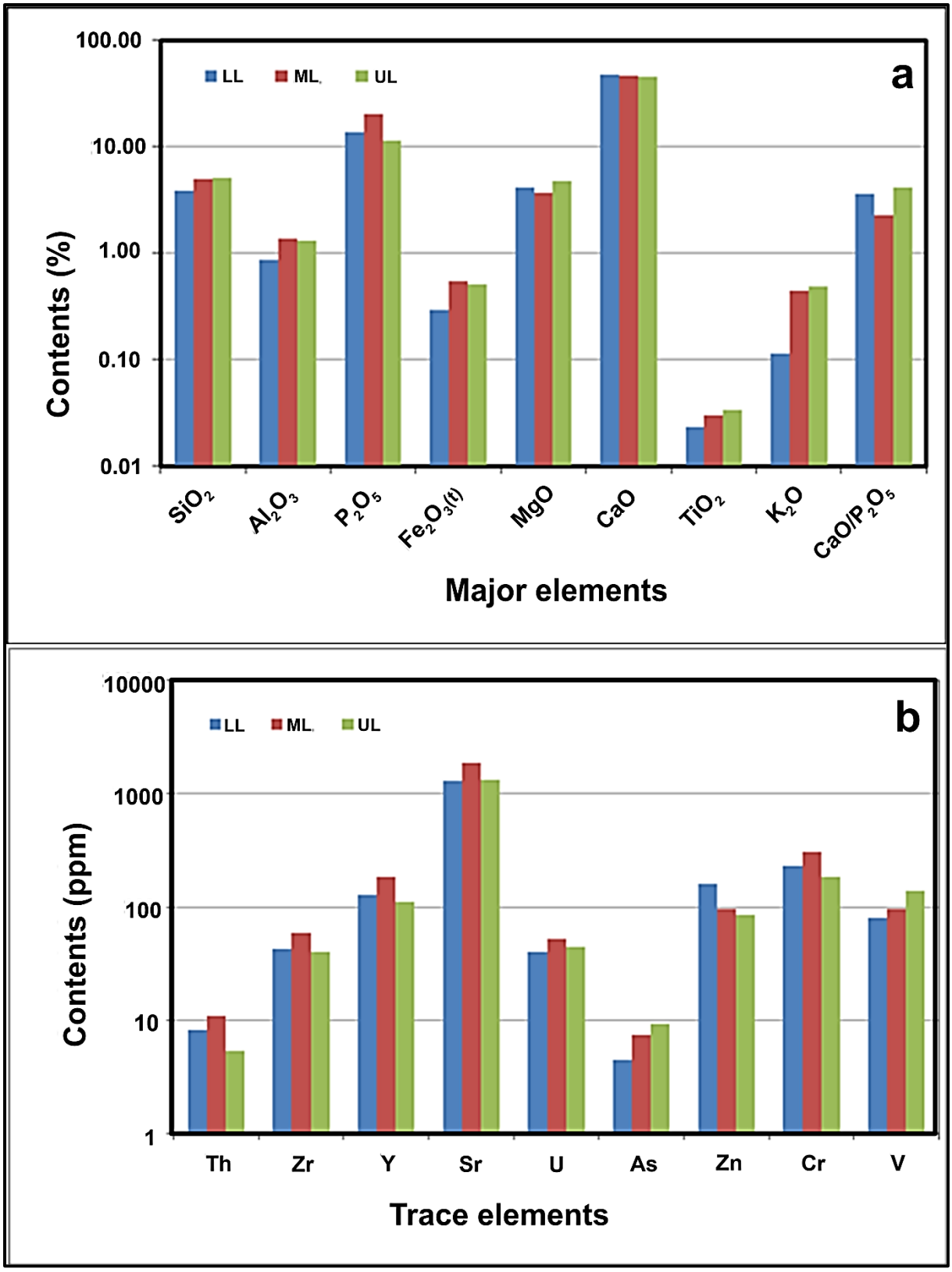

Fig. 45: Histograms displaying the mean concentrations of (**a)** major and (**b)** trace elements in the three sub-layers (LL: lower sub-layer, ML: main sub-layer, UL: upper sub-layer)

Figure 46a, b, c, and d illustrate the relationship between Al_2O_3 and SiO_2, $Fe_2O_{3(t)}$, K_2O, and MgO contents in the whole-rock samples. While the distribution of MgO contents is observed in both the dolomite cement and glauconite minerals, the other three oxides exhibit significant positive correlations. The correlation coefficients (*r*) for SiO_2, $Fe_2O_{3(t)}$, and K_2O are 0.95 ($p < 0.001$), 0.73 ($p = 0.038$), and 0.86 ($p = 0.006$), respectively, as we move from the lower to the upper sublayers. This pattern suggests a gradual input of these elements over time, potentially leading to the observed gradual increase in glauconite particle contents in the upper layer.

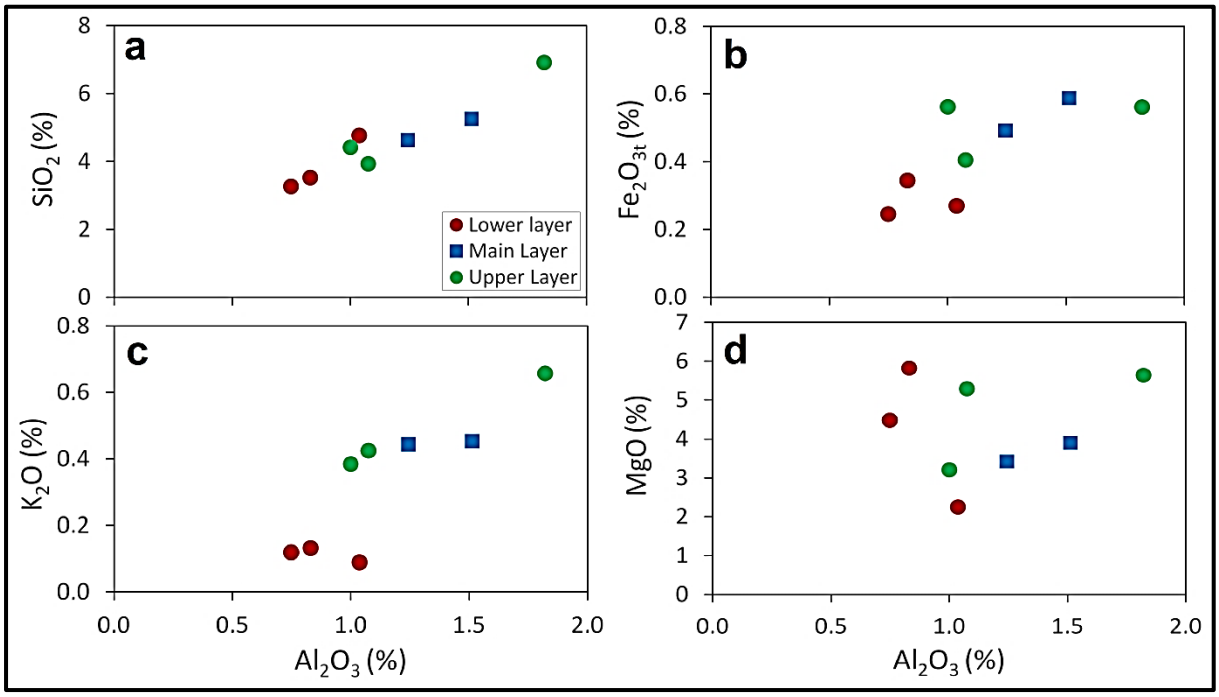

Fig. 46: Variation diagrams of Al_2O_3 *vs* SiO_2, $Fe_2O_{3(t)}$, K_2O and MgO (a, b, c, d respectively)

Nevertheless, the P_2O_5 contents do not exhibit any significant associations ($p > 0.05$) neither with CaO ($r = 0.13$, $p = 0.76$) nor with Al_2O_3 ($r = 0.12$, $p = 0.79$) (Fig. 47a, b). This suggests that CaO is present in both CFA minerals within phosphate particles and in the calcareous cements, specifically calcite and dolomite. Conversely, the trace elements strontium (Sr) and yttrium (Y) exhibit strong positive correlations with P2O5 ($r = 0.91$, $p = 0.001$),

indicating their role as substitutes for calcium in the apatite minerals found in phosphatic particles such as pellets and coprolites (Fig. 47c, d).

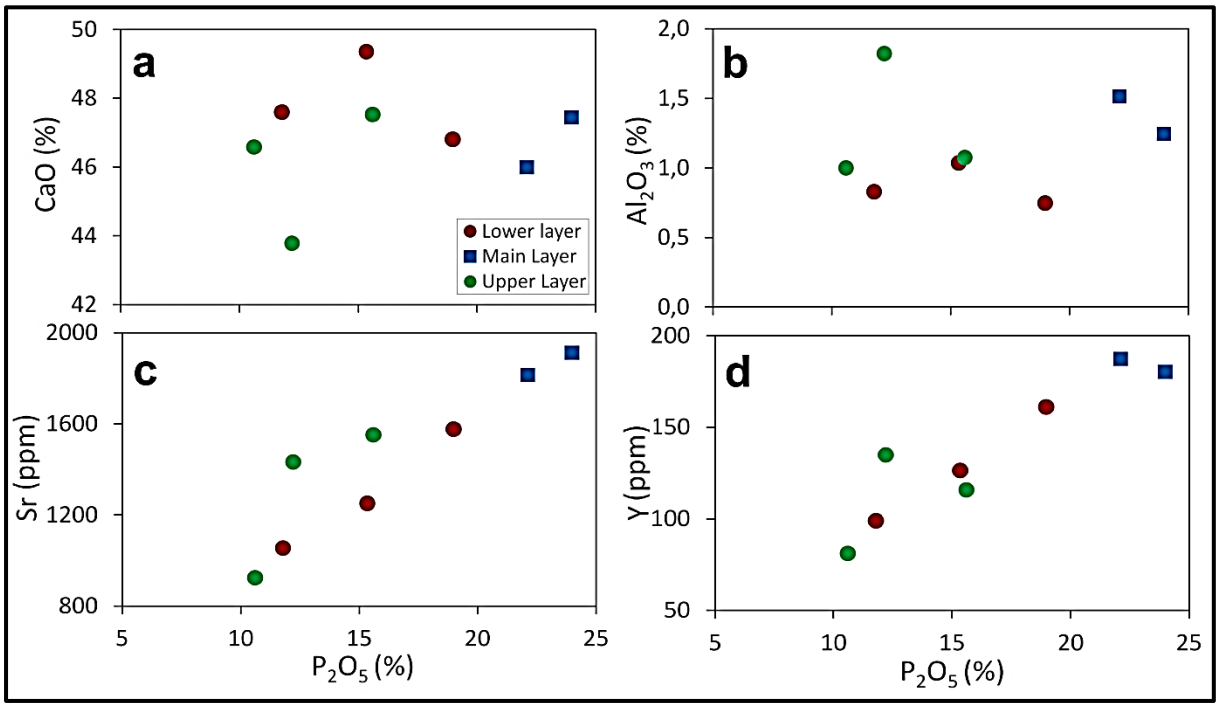

Fig. 47: Variation diagrams of P_2O_5 Vs CaO, Al_2O_3, Sr and Y (a, b, c, d respectively).

IV.2. Particles chemistry:

IV.2.1. Methodology:

To separate the different phosphate particles from the cement in phosphorite rocks, a series of techniques were used. First, the rocks were crushed then wet-sieved to obtain the desired particle size. Second, a thorough washing process was carried out to remove all cement from the various phosphorite particles. After drying, the the pellet, coprolite, and glauconite particles were separated manually using hand-picking techniques under a binocular microscope. From the three sub-layers, a total of 25 phosphatic particles were carefully chosen and selected for chemical analyses. Among these particles, there were 7 glauconites, 9 pellets, and 9 coprolites. The selected particles were then prepared for *in-stu* Laser Ablation (LA) ICP-

MS at the ICP-MS Laboratory located at Plateforme AETE-ISO, OSU OREME, University of Montpellier, France.

The examination involved the use of a ThermoFinnigan Element XR ICP-MS, paired with a Geolas (Microlas) automated platform hosting a 193 nm Compex 102 laser from LambdaPhysik. Signals were captured in Time Resolved Acquisition mode, with 2 minutes allocated for the blank and 1 minute for the measurement of the analytes. The laser was operated with an energy density of 5 J/cm2 at a frequency of 5 Hz, utilizing a spot size that varied from 50 to 120 μm. Oxide levels were assessed by monitoring the ThO/Th ratio, which remained below 0.8%. During the analytical tests, reference sample BIR-1G was examined as an unknown, and the results were in good accordance with the values reported (Gao et al., 2002). The utilization of the NIST 610 standard as an external calibration reference, alongside the internal standardization employing calcium, was executed in accordance with the methodologies outlined by Longerich et al. (1996) and Günther et al. (1999). Additional information can be found in Bosch et al. (2014) and Fernandez et al. (2016). The calculations were conducted based on the methodology proposed by Kechiched et al. (2018), resulting in weight percentages of 37% for pellets and coprolites, and 27% for glauconites. To process the data, the GLITTER software package (Van Achterberg et al., 2001) was employed, which involved analyzing time-resolved spectra and ensuring the absence of heterogeneities within the analyzed volume.

IV.2.2. Results and interpretation

IV.2.2.1. Major elements:

Table 3 displays the findings of "in situ" microanalysis concerning the primary elements examined in various phosphorite particles, including glauconites, pellets, and coprolites, sourced from the upper, main, and lower sub-layers.

Table 3: Major element concentrations in particles from the three sub-layers of the Bled El Hadba phosphorites ((gl) for glauconite, (pl) for pellet, and (cop) for coprolite).

Major oxides (wt%)							
Particles	Spot posit.	MgO	Al_2O_3	SiO_2	P_2O_5	TiO_2	Fe_2O_3
Upper sub-layer							
gl	Rim	2.49	3.64	22.39	17.57	0.02	7.26
	Core	2.18	2.97	19.91	18.27	0.01	6.27
gl	Core	2.15	2.98	19.48	18.24	0.02	6.73
pl	Core	0.56	0.93	3.42	21.92	0.05	0.45
	Rim	0.50	0.75	2.52	21.14	0.04	0.31
pl	Core	0.51	0.30	1.44	22.27	0.01	0.15
	Rim	0.38	0.14	0.75	21.19	0.01	0.12
pl	Core	0.45	0.39	1.53	22.01	0.01	0.18
cop	Core	0.45	0.53	2.17	22.44	0.03	0.46
	Rim	0.39	0.39	1.67	22.16	0.02	0.17
cop	Core	0.50	0.73	2.73	22.44	0.04	0.31
	Rim	0.48	0.64	2.49	21.75	0.04	0.26
cop	Core	0.45	0.45	1.82	21.80	0.02	0.23
Main sub-layer							
gl	Core	1.11	1.49	11.05	19.35	0.01	4.59
	Rim	2.36	3.84	24.63	19.02	0.01	8.59
gl	Core	2.22	2.83	20.01	18.86	0.01	6.52
	Rim	2.37	3.21	20.95	18.68	0.02	6.88
pl	Core	0.44	0.82	2.29	22.30	0.08	0.42
	Rim	0.41	0.47	1.54	22.66	0.02	0.25
pl	Core	0.37	0.40	1.38	24.33	0.02	0.11
	Rim	0.36	0.21	0.83	22.17	0.01	0.10
pl	Core	0.48	0.95	3.88	24.03	0.04	0.42
cop	Core	0.48	0.62	2.01	23.67	0.04	0.34
	Rim	0.45	0.41	1.76	23.59	0.02	0.33
cop	Core	0.45	0.31	1.25	22.48	0.02	0.26
	Rim	0.45	0.30	0.99	23.20	0.01	0.33
cop	Core	0.40	0.09	0.69	23.51	0.05	0.05
Lower sub-layer							
gl	Core	0.63	0.66	6.21	17.69	0.01	3.98
	Rim	0.91	1.02	8.86	17.45	0.01	4.60
gl	Rim	1.04	1.16	11.87	18.19	0.01	6.62
	Core	1.09	1.20	11.70	18.84	0.01	5.76
gl	Core	1.84	1.96	17.49	19.01	0.01	7.46
pl	Core	0.30	0.26	0.91	23.82	0.02	0.31
	Rim	0.35	0.28	0.91	22.13	0.02	0.13
pl	Core	0.37	0.34	1.30	23.68	0.02	0.31
	Rim	0.38	0.34	1.39	23.88	0.04	0.27
pl	Core	0.36	0.28	1.00	24.08	0.01	0.10
cop	Core	0.33	0.00	0.37	23.81	0.00	0.07
	Rim	0.31	0.01	0.29	24.03	0.00	0.06
cop	Core	0.34	0.21	0.81	23.91	0.01	0.09
	Rim	0.34	0.28	0.87	23.58	0.02	0.11
cop	Core	0.30	0.00	0.38	24.12	0.00	0.03

The P_2O_5 concentrations in both the pellets and coprolites exhibit a limited range of values, from 21.14 to 24.33 wt% (with an average of 22.94 wt%) across the three sub-layers (LL, ML, and UL). In contrast, the glauconite minerals display slightly lower P_2O_5 contents compared to the pellets and coprolites, with concentrations ranging from 17.45 to 19.35 wt% (average of 18.43 wt%). It is likely that the PO_4^{3-} ions are adsorbed within the microfractures and pores of the mineral, as suggested by Younes et al. (2019). It can be observed that the cores of the glauconite, pellet, and coprolite particles show a minor increase in P_2O_5 content when compared with the rims.

The pellets and coprolites of the three sub-layers contain very low contents of some oxides, such as SiO_2, Al_2O_3, MgO, TiO_2, and Fe_2O_3. This is attributed to the prevalence of carbonate fluorapatite (CFA) as the main mineral with the theoritcal formula of: (Ca, Na, Mg, $Sr)_{10}(PO_4, CO_3, SO_4)_6F_2$ (McArthur et al., 1980; McArthur et al., 1986)) in these particles, as opposed to glauconites which contain SiO_2, Al_2O_3, MgO, and Fe_2O_3 as major components in its chemical formula $(K,Na)(Fe,Al,Mg)_2(Si,Al)_4O_{10}(OH)_2$.

The enrichment of SiO_2, Al_2O_3, $Fe_2O_{3(t)}$, and MgO, along with the depletion of P_2O_5, observed from the cores to the rims of individual glauconite particles, could be indicative of glauconitization. This process was previously referenced by Kechiched et al. (2018) in their examination of glauconite-bearing phosphorites found in Djebel El Kouif and Kef Essenoun deposits. A noticeable decline in the P_2O_5 content from the cores to the rims can be observed within the single pellet and coprolite particles. This finding provides evidence that in the Bled El Hadba phosphorites, the phosphatization process of fecal pellets took place before the glauconitization process. Furthermore, the process of glauconitization of phosphatized particles intensifies over time, as the particles in the lower sub-layer contain lower concentrations of MgO, SiO_2, $Fe_2O_{3(t)}$ (as shown respectively in Fig. 48a, b, c for glauconites; Fig. 48d, e, f for pellets and coprolites) and Al_2O_3 compared to those in the main and upper

sub-layers. Nevertheless, there is a slight decrease in phosphatization observed from the lower to the upper sub-layers, with average P_2O_5 contents varying from 21.88 ± 2.73 wt% to 21.02 ± 1.76 wt%, respectively (Fig. 48g, h) (see also Table 3).

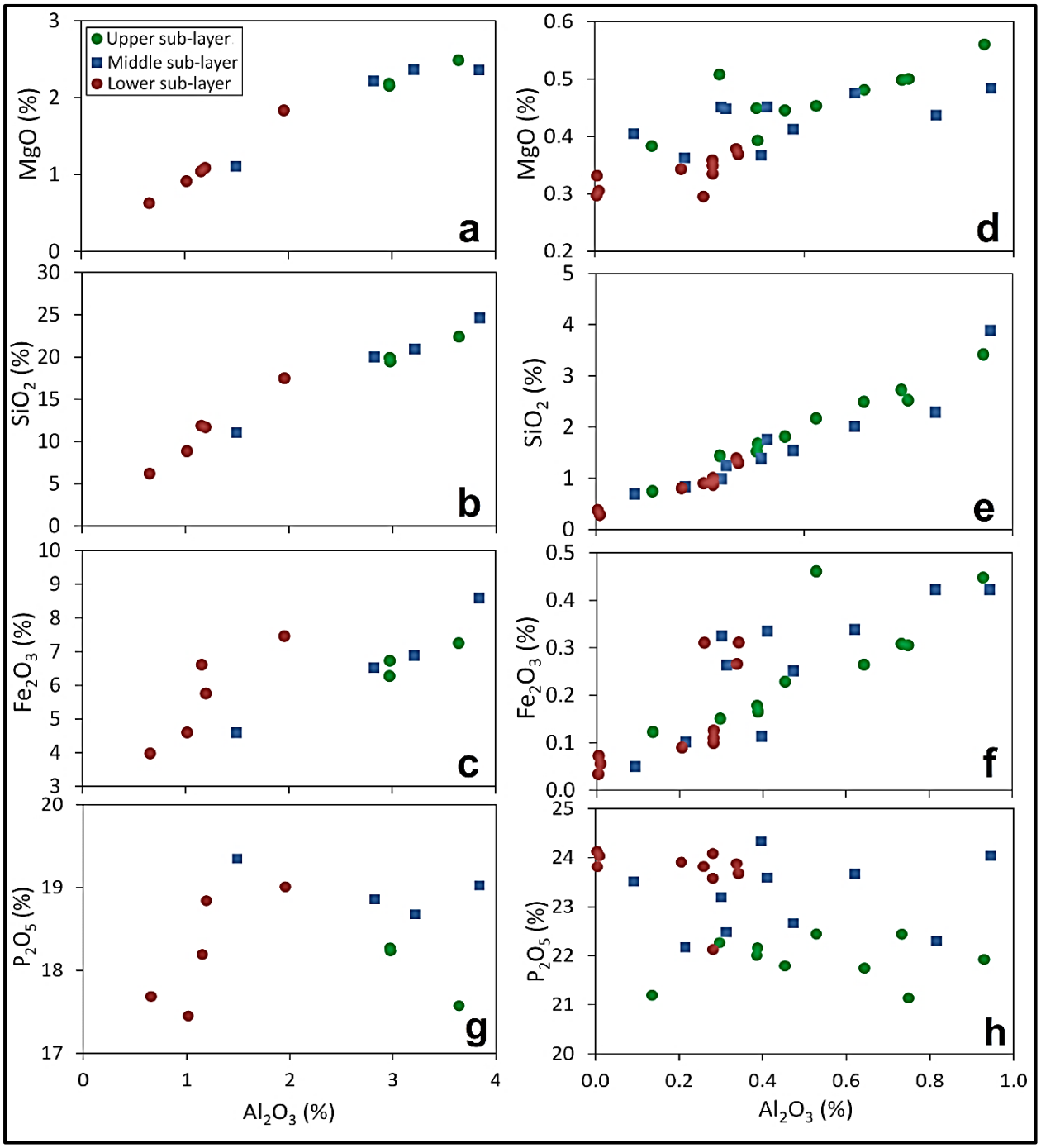

Fig. 48: Variation diagrams of Al_2O_3 in relation to MgO, SiO_2 and Fe_2O_3(t) for glauconites (a, b, c) and for pellets and coprolite (d, e, f), and in relation to P_2O_5 for glauconites (g) and pellets and coprolite (h) of phosphorites from the Bled El Hadba deposit.

Besides the glauconitization processes, the adsorption of PO_4^{3-} might serve as an additional factor contributing to the observed P_2O_5 enrichment in glauconite minerals. This could potentially elucidate the absence of a distinct correlation between Al_2O_3 and P_2O_5 ($r = 0.17$, $p = 0.593$). In their experimental study, Younes et al. (2019) pointed out the suitability of glauconite as a natural adsorbent for phosphate removal from wastewater, attributing its effectiveness to specific features such as pore radius, pore volume, and irregular structure, which were similarly described by McRae (1972).

IV.2.2.2. Trace elements:

Table 4 illustrates the outcomes of the "in situ" microanalysis for trace elements that were applied to different phosphorite particles, such as glauconites, pellets, and coprolites, across the upper, main, and lower sub-layers.

The analysis of trace elements indicates that glauconites show notably high contents of V, Cr, Ni, Zn, and Rb compared to those in pellets and coprolites, with no significant distinctions observed among the three sub-layers. Conversely, the Sr and Ba concentrations are higher in pellets and coprolites compared to glauconite. The V content in glauconites across the three sub-layers ranges from 164 to 356 ppm, while in pellets and coprolites, V concentrations vary between 31.9 and 162 ppm. The Cr contents in glauconites display a significant variability, with values ranging from 234 to 1987 ppm. The average Cr content is 416 ppm for the lower sub-layer, 1300 ppm for the main sub-layer, and 1285 ppm for the upper sub-layer. In contrast, pellets and coprolites exhibit a narrower range of Cr contents, varying from 34.6 to 306 ppm across the lower to upper sub-layers. Nickel concentrations in glauconites range from 10 to 35 ppm, whereas pellets and coprolites have much lower concentrations, below 10 ppm. The zinc contents in glauconites exhibit an upward trend, with concentrations increasing from approximately 100 ppm in the lower and main sub-layers to a

peak of 363 ppm in the upper sub-layer. However, pellets and coprolites display lower zinc contents, often below 100 ppm. In terms of Rb concentrations, glauconites show varying levels, starting from 41.1 ppm in the lower sub-layer and peaking at 117 ppm in the upper sub-layer.

Table 4: Trace element concentrations in particles from the three sub-layers of the Bled El Hadba phosphorite ((gl) for glauconite, (pl) for pellet, and (cop) for coprolite).

Trace elements (ppm)														
Particles	Spot posit.	V	Cr	Co	Ni	Cu	Zn	Rb	Sr	Y	Zr	Ba	Th	U
Upper sub-layer														
gl	Rim	356.35	1658.56	0.93	35.62	13.25	363.15	116.74	1185.96	358.08	64.44	8.60	7.28	83.77
	Core	273.97	1127.68	0.83	23.30	12.00	291.27	98.93	1005.59	278.03	50.80	6.12	5.15	83.64
gl	Core	269.40	1067.70	0.75	33.61	12.16	346.41	101.87	1042.13	274.83	58.40	6.54	3.87	78.59
pl	Core	72.75	291.77	1.37	10.40	24.00	129.70	7.00	2003.30	96.11	28.71	22.94	0.96	23.08
	Rim	65.24	278.59	1.17	8.25	16.38	107.80	6.35	1960.05	162.43	25.72	20.84	5.36	28.26
pl	Core	106.94	303.24	1.16	6.32	24.16	118.99	2.08	2390.89	157.69	22.45	46.21	0.38	32.58
	Rim	162.33	305.60	0.79	7.21	7.12	93.08	1.12	2222.44	278.23	20.79	22.31	4.52	65.28
pl	Core	49.34	118.75	1.06	6.14	32.82	95.12	2.85	2109.41	79.90	7.41	16.81	0.30	22.44
cop	Core	73.72	257.60	1.28	20.42	14.97	129.84	4.01	2064.00	68.09	21.72	16.68	0.57	22.89
	Rim	56.59	233.27	0.83	6.94	14.40	79.04	3.72	1989.01	298.13	25.55	17.38	5.24	70.50
cop	Core	58.22	215.01	1.42	8.55	101.68	142.82	4.94	1949.20	85.08	20.40	20.94	0.63	18.23
	Rim	57.73	221.16	1.04	5.65	43.93	113.09	4.63	2027.59	98.55	24.45	19.32	1.24	20.94
cop	Core	63.28	200.33	0.94	5.93	13.37	91.47	2.98	2081.26	74.15	21.66	21.67	0.45	19.85
Main sub-layer														
gl	Core	129.11	539.22	0.55	7.07	9.75	75.64	67.51	967.39	214.58	19.90	6.72	2.07	31.36
	Rim	287.74	1987.13	1.36	14.87	7.50	139.82	133.81	966.07	521.44	42.28	8.61	10.98	37.47
gl	Core	335.86	841.09	0.63	9.99	7.43	110.82	97.85	952.38	263.88	37.17	7.19	2.38	95.09
	Rim	379.97	1829.49	0.61	13.79	15.72	128.60	105.83	1026.56	532.57	34.88	9.03	10.17	45.63
pl	Core	37.69	245.33	1.05	7.73	12.19	76.14	8.01	2340.44	115.16	22.38	26.44	1.25	33.26
	Rim	39.29	219.38	0.95	2.47	6.49	70.78	4.39	2490.85	312.07	21.05	26.12	7.89	53.95
pl	Core	53.34	184.01	0.82	2.51	9.11	64.15	2.61	2258.88	111.63	15.86	32.76	0.63	25.74
	Rim	40.90	233.80	0.81	2.52	6.67	53.65	1.88	2322.68	253.92	29.82	26.11	18.53	53.44
pl	Core	80.68	285.80	0.97	6.46	15.36	76.34	8.40	2331.10	67.95	18.50	28.81	0.82	27.58
cop	Core	48.90	138.09	1.05	3.38	15.97	68.69	6.66	2363.44	58.21	13.93	33.82	0.74	16.76
	Rim	43.26	140.70	0.82	1.20	8.29	57.72	5.86	2219.74	81.49	14.90	33.09	1.61	15.89
cop	Core	33.88	117.34	0.73	3.04	5.79	65.52	3.45	2401.13	56.23	9.07	30.53	0.30	15.80
	Rim	31.85	163.01	0.86	3.54	4.29	64.74	3.46	2359.26	62.00	12.58	31.55	0.26	15.67
cop	Core	32.64	75.87	0.69	2.17	7.21	46.40	0.85	2321.96	67.12	11.38	17.26	0.43	17.10
Lower sub-layer														
gl	Core	224.36	233.70	1.199	30.14	20.65	122.06	41.1	1077.3	74.64	23.08	6.74	0.564	41.37
	Rim	187.84	291.68	0.834	15.29	18.36	97.6	59.29	1110.6	129.13	19.44	6.97	2.28	55.52
gl	Rim	244.3	402.98	1.055	34.46	29.81	164.69	74.79	1035.6	168.06	25	7.73	0.15	32.68
	Core	164.1	413.47	0.525	10.3	25.28	105.9	80.66	968.53	115.34	15.45	6.64	2.66	30.62
gl	Core	278.91	740.26	0.81	19.39	71.18	156.89	102.38	1201.2	92.45	30.01	11.03	2.98	31.67
pl	Core	89.48	223.25	0.737	9.42	8.59	53.11	1.717	2255.1	143.73	33.03	26.56	2.76	29.33
	Rim	79.2	191.08	0.693	3.7	3.74	28.53	1.923	2354.33	254.68	20.72	24.13	17.64	74.16
pl	Core	58.07	196.61	0.899	4.57	26.99	59.03	4.41	2193.14	90.7	17.62	23.44	0.37	17.38
	Rim	56.85	211.81	0.591	5.45	21.76	61.44	4.26	2244.7	117.85	20.92	24.28	2.20	20.72
pl	Core	91.11	214.02	0.694	5.57	4.5	30.27	1.623	2326.45	95.25	26.42	26.98	0.66	31.9
cop	Core	51.70	40.94	0.531	3.61	7.16	39.05	0.161	2480.8	83.85	4.48	21.2	0.01	22.38
	Rim	49.38	41.17	0.567	3.13	6.98	37.54	0.168	2339	84.8	4.77	20.63	0.30	22.82
cop	Core	53.22	70.12	0.694	3.01	23.42	41.21	1.638	2181.9	99.12	11.38	27.85	0.51	26.91
	Rim	72.16	108.40	0.663	3.59	17.55	37.58	2.396	2266.23	128.96	18.82	27.92	1.491	30.01
cop	Core	48.61	34.56	0.439	3.56	6.7	34.21	0.199	2351.49	84.54	3.73	17.78	0.151	24.05

On the other hand, pellets and coprolites contain significantly lower Rb contents, often measuring below 9 ppm. The concentrations of Sr in pellets and coprolites are significantly

higher compared to glauconites. On average, pellets and coprolites contain 2208 ppm of Sr, with concentrations ranging from 1949 ppm to 2491 ppm. In contrast, glauconites have an average Sr concentration of 1045 ppm, with concentrations between 952 ppm and 1201 ppm. When it comes to Ba content, pellets and coprolites exhibit variations from 17 ppm to 46 ppm, depending on the sub-layer. In contrast, glauconites consistently have Ba contents below 10 ppm in all three sub-layers.

Calcium (Ca^{2+}), with its ionic radius (0.99 Å), can be substituted for Na^{+} (0.97 Å), Sr^{2+} (1.12 Å), Th^{4+} (0.94 Å), Y^{3+} (0.93 Å), U^{4+} (0.89 Å), REEs, and other elements possessing similar ionic radii. Within the Bled El Hadba phosphorites, Sr is the most abundant among trace elements, with concentrations that may go beyond 2400 ppm. Sr is enriched in marine phosphorites worldwide, up to 1900 ppm (Tooms et al., 1969). Furthermore, Lucas et al. (1990) conducted experiments that revealed a correlation between the Sr content of apatite and the equilibrium precipitation from fluids containing varying levels of Sr. The high contents of strontium (Sr) in the Bled El Hadba phosphorites can be attributed to their marine origin. This is because Sr, along with barium (Ba) to a lesser extent, substitutes for calcium (Ca) in carbonate-fluor apatite (CFA), as observed by Lucas et al. (1990). The pellets and coprolites, which are primarily composed of CFA (Tahri et al., 2019), exhibit a higher concentration of Sr (averaging at 2208 ppm) and Ba (up to 46 ppm) compared to glauconite minerals (with an average Sr content of 1045 ppm and less than 11 ppm Ba). This aligns with the findings of McArthur (1978, 1985), who noted that francolites (CFA) typically contain approximately 2500 ppm of strontium. In contrast, glauconites demonstrate significantly higher concentrations of V, Cr, Ni, Zn, and Rb when compared to pellets and coprolites. With ionic radii of 0.54 Å and 0.62 Å, V^{+5} and Cr^{+3} have the potential to replace Fe^{3+} (0.63 Å) or Al^{3+} (0.53 Å), while Ni^{2+} (0.69 Å) and Zn^{2+} (0.68 Å) may substitute for Mg^{2+} (0.66 Å) in glauconite with a formula ($K_{0.79}$ $Ca_{0.05}$ ($Al_{0.35}$ $Fe^{3+}{}_{1.06}Fe^{2+}{}_{0.25}$ $Mg_{0.41}$) ($Si_{3.61}Al_{0.39}$)$O_{10}(OH)_2$) as given by

McRae (1972), though other elements such as V4+, Pb^{3+}, U^{4+}, and Th^{4+} may substitute Ca^{2+} in the apatite structure (Gilinskaya, 1990 ; Gilinskaya et al., 1993; Gilinskaya and Tybulewicz, 1993; Gilinskaya and Zanin, 1983) of pellets and coprolites. In the case of glauconite, Rb^{+} can easily substitute for K^{+} due to the similarities in their valence state (1+) and ionic radius (1.48 Å for Rb^{+} and 1.33 Å for K^{+}). The glauconites in the main sub-layer can contain Rb^{+} concentrations as high as 134 ppm. However, in pellets and coprolites, which are relatively poorer in K^{+}, the Rb^{+} concentrations are lower, measuring less than 9 ppm (cf. Table 4).

IV.2.2.3. Rare earth elements:

The results of REE analysis in the different phosphorite particles (glauconites, pellets and coprolites) from the upper, main and lower sub-layers are shown in table 5.

The data of rare earth elements (Tab. 5) exhibit exceptional high contents, whether in glauconites, pellets, or coprolites. However, upon closer inspection, it can be seen that the most important concentrations are in glauconite particles. Specifically, the sum values of rare earth elements (∑REE) in glauconites range from 253 to 2050 ppm in the whole phosphorite layer. In the three sub-layers, an average concentration of 380 ppm is observed in the lower sub-layer, 1429 ppm in the main sub-layer, and 948 ppm in the upper sub-layer.

The *in-situ* analyses of individual glauconite minerals also show an interesting observation: the rims of the crystals exhibit higher concentrations of REE in comparison to the cores. The ∑REE contents detected in pellets and coprolites are notably decreasing compared to those identified in glauconites, with values ranging from 194 to 911 ppm. The lower, main, and upper sub-layers display mean ∑REE concentrations of 346 ppm, 399 ppm, and 375 ppm, respectively. Furthermore, it should be emphasized that the REE levels in the analyzed pellet and coprolite particles exhibit a consistent pattern of being greater in the peripheral rims than in the central cores, as indicated in Table 5. This phenomenon can be attributed to the process of REE uptake from an external source.

Table 5: REE concentrations in particles from the three sub-layers of the Bled El Hadba phosphorite ((gl) for glauconite, (pl) for pellet, and (cop) for coprolite).

Rare earth elements (ppm)																
Particle	Spot posit.	La	Ce	Pr	Nd	Sm	Eu	Gd	Tb	Dy	Ho	Er	Tm	Yb	Lu	∑REE
Upper sub-layer																
gl	Rim	260.19	306.66	53.28	230.96	43.72	10.98	47.09	6.77	39.42	8.79	23.07	2.92	18.93	2.65	1055.43
	Core	228.26	265.03	42.91	192.50	36.79	9.04	37.21	5.19	30.63	6.88	17.71	2.33	14.26	2.01	890.75
gl	Core	229.66	269.00	44.32	192.65	35.95	9.12	36.21	5.36	30.42	6.89	18.56	2.40	14.47	2.10	897.11
pl	Core	73.59	90.44	13.26	56.87	10.89	2.98	11.05	1.63	10.14	2.14	5.66	0.92	6.04	0.94	286.56
	Rim	110.80	125.61	19.34	84.13	16.11	4.08	16.26	2.52	16.22	3.88	9.66	1.53	10.22	1.59	421.95
pl	Core	97.28	79.36	12.42	54.03	9.56	2.86	11.06	1.70	11.30	2.96	8.42	1.33	8.70	1.31	302.28
	Rim	162.16	139.73	26.42	116.85	22.17	5.71	23.89	3.59	24.32	5.91	16.22	2.31	15.45	2.26	566.99
pl	Core	63.43	78.60	11.69	49.89	9.68	2.67	9.11	1.42	8.72	1.88	4.80	0.68	5.03	0.65	248.24
cop	Core	52.29	60.14	8.70	37.61	6.94	2.01	6.96	1.10	6.88	1.58	4.23	0.65	4.52	0.71	194.32
	Rim	224.44	290.53	42.31	182.66	34.97	8.97	34.80	5.20	32.74	7.18	20.34	2.81	19.33	2.91	909.19
cop	Core	71.09	89.09	13.14	57.91	11.09	2.95	10.52	1.67	9.78	2.11	5.35	0.73	4.76	0.70	280.88
	Rim	78.28	95.25	14.41	62.38	11.42	3.16	11.48	1.76	10.73	2.47	6.45	0.92	6.22	0.91	305.83
cop	Core	60.06	72.07	11.00	45.62	8.60	2.47	8.85	1.33	8.27	1.78	4.86	0.69	4.81	0.73	231.14
Average		131.66	150.89	24.09	104.93	19.84	5.15	20.35	3.02	18.43	4.19	11.18	1.56	10.21	1.50	506.97
SD		77.77	94.37	15.82	69.44	13.21	3.20	13.77	1.95	11.41	2.56	6.91	0.88	5.59	0.81	315.67
Main sub-layer																
gl	Core	201.25	251.83	35.72	153.09	27.48	7.08	29.38	3.98	22.75	5.01	13.27	1.68	10.38	1.52	764.43
	Rim	477.77	686.02	98.58	448.62	84.24	21.12	85.18	11.60	62.86	12.84	31.21	3.96	23.08	3.12	2050.20
gl	Core	250.68	338.67	51.63	227.82	44.06	10.77	41.82	5.62	31.29	6.67	16.10	2.17	13.48	1.93	1042.71
	Rim	436.84	582.90	96.13	419.46	80.05	20.29	80.27	10.66	58.84	12.52	30.48	3.83	22.73	3.08	1858.08
pl	Core	102.50	114.50	16.87	71.37	12.90	3.29	12.47	1.98	11.46	2.58	7.21	1.03	7.17	1.07	366.40
	Rim	226.28	270.37	40.23	171.29	33.52	8.41	35.22	5.28	31.94	7.58	21.09	2.90	19.03	2.98	876.12
pl	Core	96.87	123.69	18.39	81.33	15.05	4.19	14.63	2.18	12.72	2.79	7.32	1.01	7.16	1.01	388.34
	Rim	210.30	307.46	43.72	188.99	36.53	8.72	34.06	5.01	30.52	6.63	17.05	2.40	16.61	2.55	910.55
pl	Core	60.78	76.59	11.18	49.24	9.21	2.49	8.53	1.32	7.59	1.67	4.40	0.60	4.11	0.59	238.30
cop	Core	54.85	72.31	11.13	47.58	9.20	2.51	8.32	1.23	7.15	1.49	3.98	0.55	3.63	0.54	224.48
	Rim	74.11	97.56	14.57	62.94	12.33	3.05	11.61	1.65	9.51	2.07	5.56	0.73	4.97	0.68	301.35
cop	Core	53.01	71.63	10.47	43.19	8.39	2.13	7.79	1.17	6.95	1.46	3.81	0.53	3.72	0.50	214.74
	Rim	55.19	71.77	10.76	44.78	7.74	1.97	8.16	1.18	6.55	1.58	4.13	0.58	3.74	0.58	218.70
Average		176.96	235.79	35.34	154.59	29.28	7.39	29.03	4.07	23.09	4.99	12.74	1.69	10.75	1.55	727.26
SD		143.97	202.62	30.97	138.79	26.39	6.58	26.66	3.55	19.40	4.05	9.86	1.25	7.41	1.05	620.84
Lower sub-layer																
gl	Core	72.48	78.38	11.56	50.73	9.04	2.34	9.03	1.32	7.18	1.69	4.15	0.55	3.55	0.53	252.52
	Rim	112.44	119.22	17.86	80.58	14.04	3.70	15.50	2.04	12.14	2.81	7.08	0.93	5.75	0.87	394.96
gl	Rim	154.69	169.15	23.50	105.12	18.84	5.01	20.56	2.87	15.94	3.66	9.50	1.26	7.68	1.06	538.84
	Core	106.31	124.68	18.28	81.61	15.63	4.21	16.46	2.25	12.89	2.66	6.97	0.90	5.96	0.80	399.61
gl	Core	71.69	98.55	15.42	71.03	13.94	3.57	13.81	1.93	10.60	2.34	6.14	0.81	4.65	0.72	315.19
pl	Core	89.89	111.52	16.85	72.47	13.56	3.80	14.56	2.23	14.35	3.34	9.62	1.36	9.98	1.56	365.09
	Rim	143.69	200.22	32.05	139.40	29.33	7.27	29.58	4.55	27.80	6.42	17.35	2.47	17.50	2.52	660.15
pl	Core	60.75	65.07	9.94	43.26	8.08	2.12	8.34	1.30	8.12	1.93	5.65	0.75	5.26	0.85	221.41
	Rim	71.59	73.43	12.36	54.62	10.46	2.61	11.07	1.69	10.86	2.49	6.72	1.02	6.85	1.04	266.81
pl	Core	77.47	94.41	13.35	57.48	10.33	2.68	10.35	1.63	9.18	2.11	5.77	0.85	5.78	0.88	292.26
cop	Core	69.78	94.24	14.18	60.40	11.51	3.08	11.29	1.69	9.04	2.09	5.66	0.74	4.85	0.73	289.28
	Rim	72.47	100.74	14.89	64.98	12.09	3.49	11.69	1.75	9.87	2.10	5.55	0.77	4.71	0.69	305.79
cop	Core	84.17	110.13	16.74	69.97	13.37	3.80	13.06	1.90	11.26	2.44	6.45	0.86	5.71	0.82	340.69
Average		91.34	110.75	16.69	73.20	13.86	3.67	14.25	2.09	12.25	2.78	7.43	1.02	6.79	1.01	357.12
SD		29.66	37.64	5.77	25.44	5.45	1.35	5.67	0.85	5.28	1.23	3.35	0.49	3.60	0.52	122.18

The LREE/HREE ratios exhibit variation within the range of 5 to 8, indicating an enrichment of light rare earth elements (LREEs: La to Eu) compared to heavy rare earth elements (HREEs: Gd to Lu). The element yttrium (Y) displays high contents, with concentrations reaching 312 ppm in pellets, up to 298 ppm in coprolites, and up to 533 ppm in glauconites. Yttrium content tends to be higher in the main sub-layer in comparison with the upper sub-layer, while the lower sub-layer displays the lowest recorded Y concentrations.

Phosphorites have been recognized for their remarkable enrichment of Rare Earth Elements (REE) compared to other marine sedimentary rocks, as evidenced by various studies (Altschuler, 1980; Altschuler et al., 1967; McKelvey, 1950). The concentrations of REEs in phosphorites are mainly influenced by many factors such as depositional and redox conditions, detrital input, pH, water depth, and geological age, as indicated in previous research (Picard et al., 2002; Baioumy, 2011; Khan et al., 2012; Khan et al., 2016). Porewater, along with seawater, significantly impacts the rare earth element (REE) composition of authigenic carbonate fluorapatite (francolite) found in marine sediments (Zhu and Jiang, 2017). Francolite, the primary phosphatic mineral, is renowned for its capacity to accumulate REEs by replacing Ca^{2+} ions (Emsbo et al., 2015; Jarvis et al., 1994; Piper, 1999).

Glauconite is found throughout the Bled El Hadba phosphorites and occurs in the three sub-layers of the deposit. However, its abundance increases from the bottom to the top of the whole phosphorite layer. In-depth analysis using *in-situ* Laser Ablation ICP-MS reveals that glauconite samples from the main sub-layer have higher concentrations of rare earth elements (REE) compared to those from the upper and lower sub-layers. Specifically, the glauconite samples from the main sub-layer exhibit higher REE contents, reaching 2050 ppm, while those from the upper sub-layer range up to 1055 ppm, and those from the lower sub-layer range between 252 and 538 ppm. In contrast, glauconites exhibit a higher concentration of rare earth elements (REE) compared to pellets and coprolites as a whole. The glauconites of the lower,

main, and upper sub-layers show average REE contents of 346 ppm, 399 ppm, and 375 ppm, respectively. A recent study conducted by Kechiched et al. (2018) on Djebel El Kouif and Kef Essenoun phosphorite deposits supports this finding. These researchers observed that glauconites contain the highest contents of REE compared to co-existing phosphatic particles such as pellets, coprolites, and bioclasts.

The incorporation of rare earth elements, in conjunction with phosphate ion (PO_4^{3-}), into the glauconite mineral structure involves substitution for REE and adsorption onto the mineral surface for PO_4^{3-}. This phenomenon is facilitated by the high porosity of glauconite. Conversely, in pellets and coprolites, these mechanisms are linked to the formation of carbonate fluorapatite (CFA), where the replacement of Ca^{2+} by REEs is favored due to their similar ionic radii. Previous research (Elderfeld et al., 1981; Fleet and Pan, 1995; Ilyin and Ratnikova, 1976; McLennan et al., 1979) has emphasized the significance of ionic charge in this context (Altschuler et al., 1967; Fleet and Pan, 1995).

Yttrium (Y) is positioned between Dysprosium (Dy) and Holmium (Ho) in the rare earth element series within phosphorites, because of its similar ionic radius and behaviour. This arrangement has been documented in research conducted by Bau and Dulski (1996), as well as Zhang et al. (1994). In the context of REE-enriched glauconites from Bled El Hadba phosphorites, Yttrium is also more abundant in glauconite minerals compared to pellets and coprolites, although the concentrations are slightly lower (Fig. 49). An overall increase in Y contents is accompanied by an increase in ΣREE contents within all phosphorite particles, indicating a shared behaviour for both REE and Y.

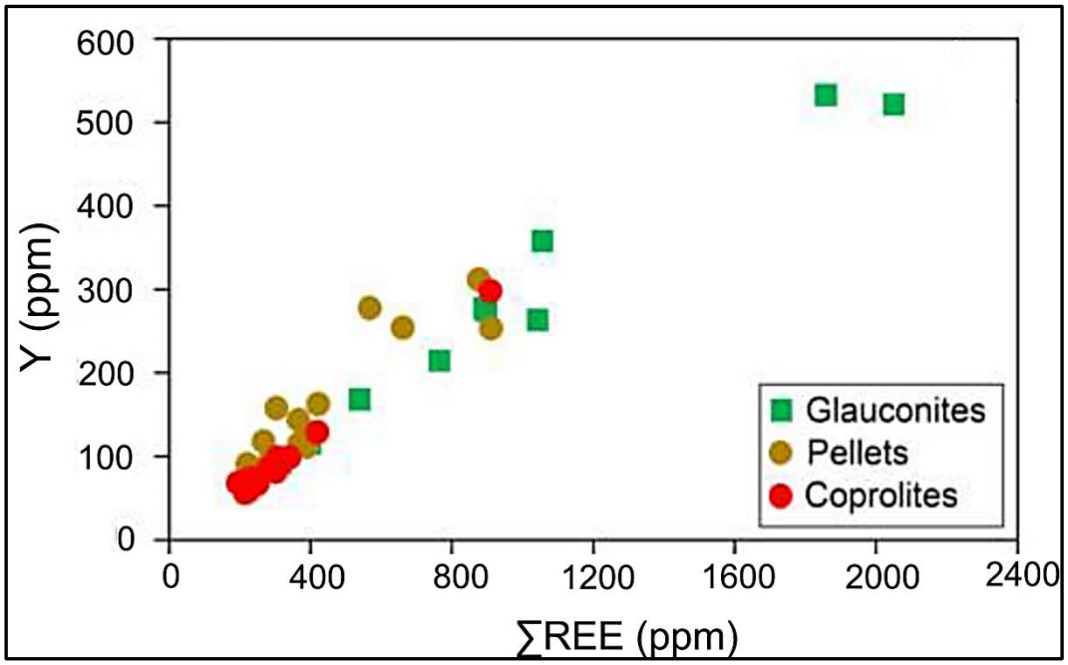

Fig. 49: REE vs. Y variations in particles from the Bled El Hadba phosphorite exhibiting significant positive correlation.

The concentration of rare earth elements (REE) within individual grains exhibits a gradual increase from the core to the rim, as indicated by the geochemical data. Jiang et al. (2007) and Zhu and Jiang (2017) have attributed this increase in REE concentrations to the susceptibility of the phosphatized particle rims to alteration by diagenetic fluids, resulting in the incorporation of higher amounts of REEs during this process. This enrichment in REEs is accompanied by a concurrent increase in glauconitization, characterized by an increase in the SiO_2, Al_2O_3, $Fe_2O_{3(t)}$, and MgO contents, which provide further evidence of the occurrence of diagenetic processes.

Conclusion:

The analysis of both whole-rock samples and individual particles reveals a comparatively low concentration of P2O5 in contrast to the compositions found in Kef Essenoun. In contrast, the particles under study exhibit higher concentrations of trace elements and REE + Y compared to particles from previously examined sites in the region.

The highest REEs concentrations are found in particles from the main and upper sub-layers, particularly in glauconites. Across all analyzed grains, the rims generally exhibit higher contents of REE + Y compared to the cores, suggesting that the uptake of REE and certain trace elements, such as Cr, Co, V, Ni, and Zn, occurred during early diagenesis as pore waters transitioned from oxic to sub-oxic conditions.

The major mechanisms that control the absorption of rare earth elements (REEs) and trace elements, such as strontium (Sr) and uranium (U), involve substitutions with Ca^{2+} existing in phases like "francolite" and other elements of glauconite minerals, in addition to adsorption. Conversely, chromium (Cr), cobalt (Co), nickel (Ni), and vanadium (V) are closely tied to the glauconitization processes.

CHAPTER V

DEPOSITIONAL ENVIRONMENT AND REDOX CONDITIONS

CHAPTER V

DEPOSITIONAL ENVIRONMENT AND REDOX CONDITIONS

For quite some time, REEs have been used as markers to characterize the paleoenvironment of phosphorite deposition, as well as the redox conditions of authigenic, biogenic, and reworked phosphorites. This approach involves tracking and interpreting different Normalized-REE patterns characteristics along with the observed geochemical anomalies (see Grandjean and Albarède, 1989; German and Elderfield, 1990; Grandjean-Lécuyer et al., 1993; Reynard et al., 1999; Vennemann et al., 2001; Morad and Felitsyn, 2001; Kocsis et al., 2007; Kalvoda et al., 2009; Garnit et al., 2012). A number of authors have extensively explored this subject, investigating the REE behaviors in various contexts (e.g., Alibo and Nozaki, 1999; Reynard et al., 1999; Bau and dulski, 1996; Ounis et al., 2011; Garnit et al., 2012; Kechiched et al., 2016; Kocsis et al., 2016; Kechiched et al., 2020; Ferhaoui et al., 2022).

V.1. Methodology:

Standard material values are essential for interpreting REE+Y patterns and normalizing the data. Yttrium is commonly classified as a REE due to its chemical characteristics closely resembling those of most REEs. Its ionic radius, which is comparable to the heavy rare earth elements (HREEs), often put between Dy and Ho in the REE series (e.g., Zhang et al., 1994; Bau, 1996; Bau and Dulski, 1996). The rock reference for sedimentary materials, particularly phosphorites, is known as "The Post Archean Australian Shale" or "PAAS." This rock reference has been widely used in various studies, including those conducted by Sholkovitz (1995), Bau and Dulski (1996), Hannigan and Sholkovitz (2001), Haley et al. (2004), Picard et al. (2002), Lécuyer et al. (2004), Ounis et al. (2008, 2012), Garnit et al. (2012), and Kocsis et

al. (2016). McClennan (1989) provided the PAAS values in Table 6, with Y's PAAS value set at 27 ppm for the purpose of element normalization in research.

Table. 6: Post Archean Australian Shale (PAAS) REEs contents (McClennan, 1989)

La	Ce	Pr	Nd	Sm	Eu	Gd	Tb	Dy	Ho	Er	Tm	Yb	Lu
38.2	79.6	8.83	33.9	5.55	1.08	4.66	0.77	4.68	0.99	2.85	0.4	2.82	0.43

The process of normalization is simple, as it is obtained by dividing the value of the element being analyzed by the value of the corresponding PAAS element. The results of REY (REE+Y) normalization are commonly depicted in graphs, with the X-axis showing the elements and the Y-axis showing the normalized values in a logarithmic scale. This visual representation enables a clear understanding of the normalized values of various elements, facilitating the comparison and examination of their relative abundances or concentrations.

V.2. PAAS-normalized REE + Y patterns and depositional environment

Two sets of PAAS-normalized REEs patterns have been identified in phosphorite deposits: (1) seawater-like patterns featuring negative Ce anomalies and HREE enrichment (e.g., Jiang et al., 2007; Pi et al., 2013; Xin et al., 2016; Zhu et al., 2014) and (2) hat-shaped patterns characterized by MREEs enrichment and depleted HREEs (e.g., Bau and Dulski, 1996; Zhu et al., 2014). Both seawater-like and hat-shaped patterns can be observed in the REE patterns of the Bled El Hadba phosphorites, with a slight enrichment of MREE (Fig. 50). These two pattern types share certain common features, including (a) negative Ce anomalies, (b) positive Eu anomalies, and (c) positive Y anomalies in all analyzed phosphorite particles.

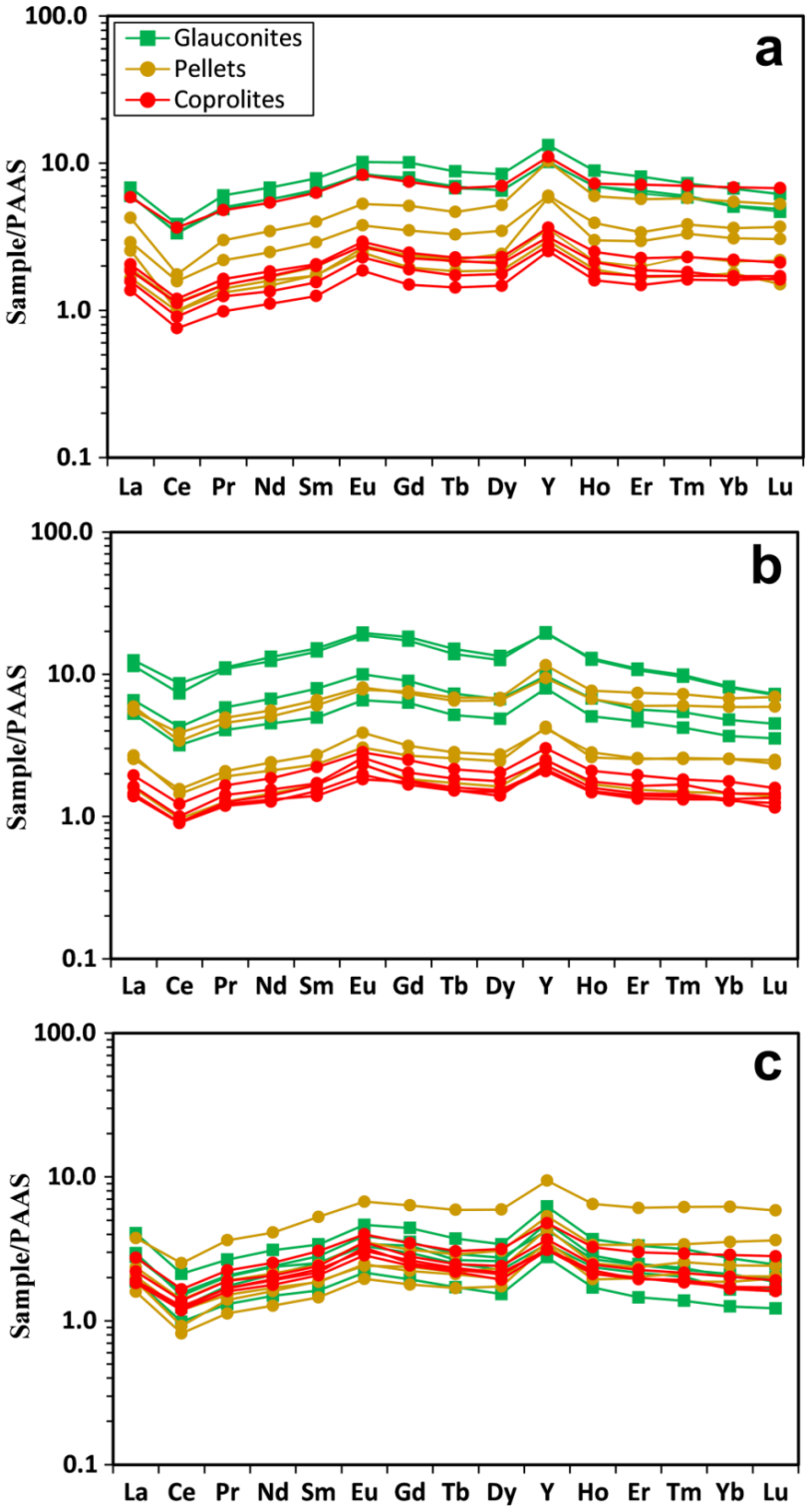

Fig. 50: The PAAS-normalized patterns of REE + Y (McLennan, 1989) of the Bled El Hadba phosphorite analysed particles. (a) upper sub-layer, (b) main sub-layer and (c) lower sub-layer.

The Bled El Hadba glauconites exhibit distinct patterns. Specifically, the three sub-layers display a hat-shaped pattern, which is attributed to the enrichment of MREEs. On the

other hand, the pellets display subtle patterns resembling those of seawater-like, indicating a relative enrichment of HREEs. Interestingly, the coprolites exhibit a combination of both hat-shaped patterns in the lower and main sub-layers, and seawater-like patterns in the upper sub-layer. Within the glauconites, the $\Sigma MREE_N$ (Sm_N to Dy_N) exhibits relatively high values (mean = 28.42 ± 19.38, n = 12), whereas the other particles show lower values (mean = 12.26 ± 6.89, n = 30). The MREE/MREE* ratios in the glauconites are notably higher, with an average of 0.63 ± 0.04, in contrast to pellets and coprolites (average of 0.56 ± 0.05). Through one-way ANOVA analysis, it is evident that both MREE/MREE* and MREEN values of glauconites significantly differ from those observed in pellets and coprolites (p-values: < 0.0001 and 0.0002, respectively). The disparity in MREE signatures for glauconite displays a notable significance when comparing different levels (p-value = 0.001). This finding is substantiated by the $(Sm/Pr)_N$ vs $(Sm/Yb)_N$ (Fig. 51) diagram, illustrating hat-shaped REE patterns for glauconites across various sub-layers and coprolites of lower and main sub-layers, indicating MREE enrichment attributed to strong pore-water influence. Conversely, pellets from all sub-layers and coprolites from upper sub-layer exhibit seawater-like patterns, showing HREEs enrichment most likely influenced by seawater.

The differences in REE + Y patterns are significantly associated with sedimentation processes, particularly phosphatization of organic particles during reworking and transoprt from deep seawater upwards by upwellings followed by early diagenetic processes that shaped the present pellets and coprolites (rounded to sub-rounded pellets; cf. chapter III). This caused the high Sr contents and P_2O_5 enrichment, along with the relatively low REE contents in pellets and coprolites (average ΣREE = 373 ± 205 ppm, n = 30 spots), compared to glauconites (average ΣREE = 872 ± 579 ppm, n = 12 spots). The difference between these two groups was found to be statistically significant based on one-way ANOVA results (p-value = 0.0002).

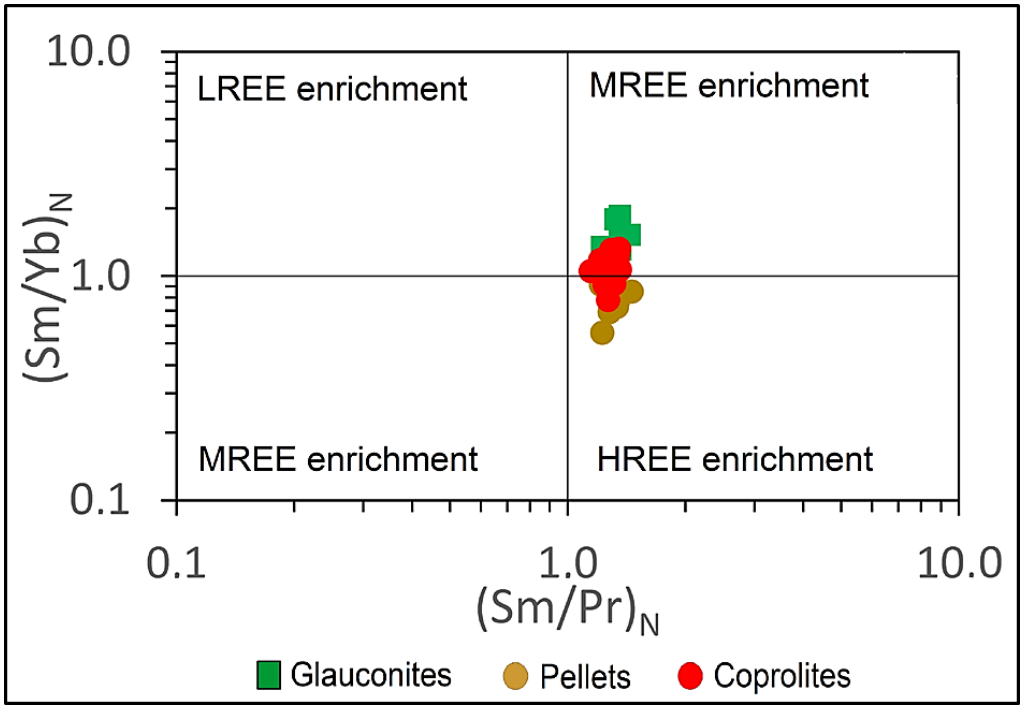

Fig. 51: $(Sm/Pr)_N$ vs. $(Sm/Yb)_N$ diagram (after Kechiched et al., 2016; Samala et al., 2018)

The glauconitization is most likely occurred in the early stages of diagenesis, following the phosphatization processes. This is evident from the higher concentrations of rare earth elements (REE) observed, which can be attributed to diagenetic uptake from pore-water, as suggested by Shields and Webb (2004). Additionally, glauconites exhibit lower strontium (Sr) contents. The findings are further supported by the $(La/Sm)_N$ vs. $(La/Yb)_N$ diagram developed by Reynard et al. (1999), where glauconites are situated within the early diagenetic field (Fig. 52). Moreover, the $(La/Yb)_N$ ratios observed in the glauconites (ranging between 1.0 and 1.5), the pellets (0.6 to 1.1), and the coprolites (0.8 to 1.1) are notably higher than those found in seawater (0.2 to 0.5; Reynard et al., 1999). This implies that the uptake of REE occurred during the early diagenesis phase, while the $(La/Sm)_N$ ratios remained unaltered (e.g., Fazio et al., 2007; Kechiched et al., 2020; Reynard et al., 1999).

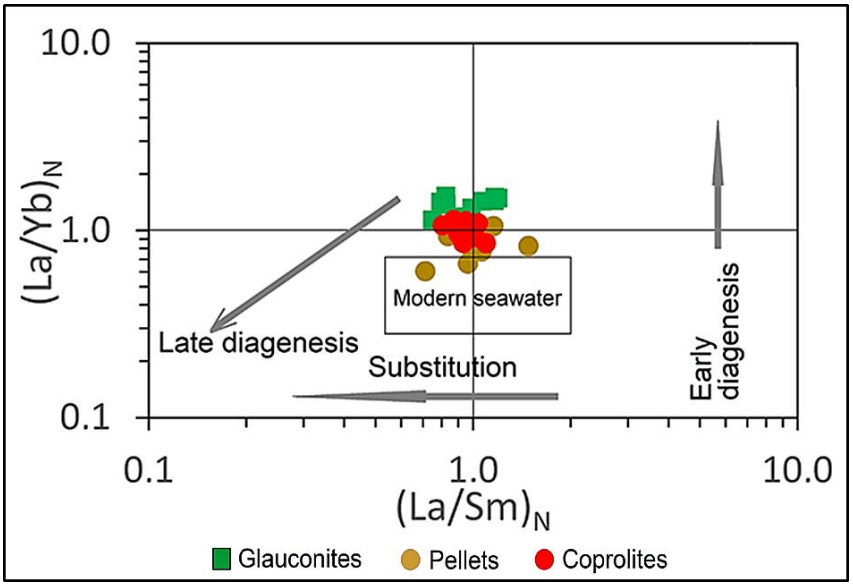

Fig. 52: $(La/Yb)_N$ vs. $(La/Sm)_N$ diagram (after Reynard et al., 1999)

V.3. Investigation on redox conditions

The determination of redox conditions often relies on the interpretation of REE anomalies, specifically Ce, Eu, and Y, which can be calculated and manifest in PAAS-normalized REE + Y patterns. Furthermore, the presence of certain trace elements, such as V, Cr, Ni, and Co, also contributes to this assessment. Understanding the behavior of these elements under different reduction/oxidation conditions is essential in gaining insights into the redox environment during the precipitation of phosphorite.

The values for Ce/Ce* and the Cerium anomaly Ce_{an} can derived from the equations: $Ce/Ce^* = 3Ce_N/(2La_N + Nd_N)$ and Ce_{an} = log Ce/Ce* (Wright et al., 1987). Similarly, the calculation for Eu/Eu* is obtained using the equation $Eu/Eu^* = Eu_N/(Sm_N + Gd_N)^{0.5}$ (Taylor and McLennan, 1985). The equation for Pr/Pr* is calculated as $2Pr_N/(Ce_N + Nd_N)$ (Bau and Dulski, 1996). Finally, the calculation of Y/Y* is obtained using the equation $2Y_N/(Dy_N + Ho_N)$ (Fazio et al., 2007).

V.3.1. Cerium anomaly

In the presence of oxygen, cerium (Ce) undergoes a chemical transformation into its tetravalent form, Ce^{4+} (Moffett, 1990, 1994; Tanaka et al., 2010). This oxidation process occurs when Mn-oxides and hydroxides absorb Ce^{4+}, resulting in a decrease in the concentration of cerium in seawater, which is indicated by a negative Ce anomaly (Bau and Dulski, 1996; Tachikawa et al., 1999). As a result, the Ce anomaly serves as a valuable indicator for assessing the redox conditions of seawater (Al-Bassam et al., 2021; Baioumy and Farouk, 2022; Gao et al., 2023; German and Elderfield, 1990; Gundogar and Sasmaz, 2022; Ling et al., 2013; Shields and Stille, 2001). Nevertheless, it is important to consider that Ce anomaly values can be influenced by various other factors, such as high La contents. To address the possibility of over-estimation of Ce anomalies, Bau and Dulski (1996) proposed the use of a Pr/Pr* vs. Ce/Ce* diagram. By referring to this diagram (see Fig. 53), It becomes apparent that the predominant number of Bled El Hadba samples aligns with the IIIb field. This observation confirms the presence of a negative Ce anomaly and further validates its utility as an indicator of redox conditions (Kechiched et al., 2020).

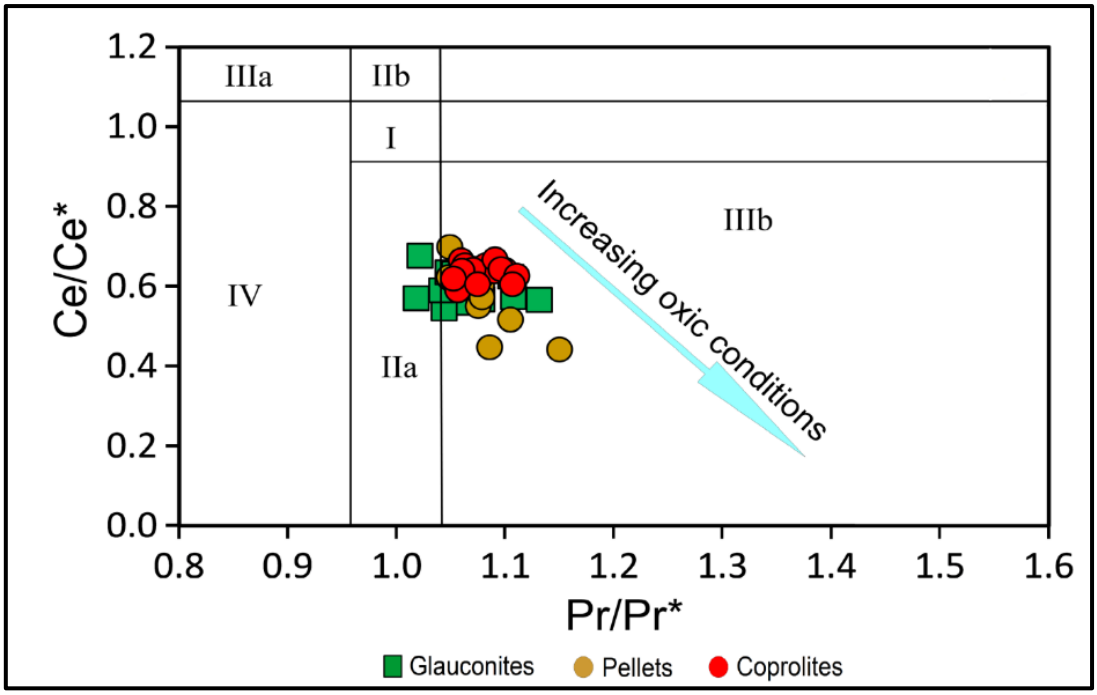

Fig. 53: The Pr/Pr* versus Ce/Ce* diagram, (after Bau and Dulski, 1996) illustrates a progression towards more oxic conditions, transitioning from glauconite to coprolites and pellets (Field I: no anomaly; Field IIa: positive La anomaly causing apparent negative Ce anomaly; Field IIb: negative La anomaly causing apparent positive Ce anomaly; Field IIIa: real positive Ce anomaly; Field IIIb: real negative Ce anomaly; Field IV: positive La anomaly disguising positive Ce anomaly); nearly all examined samples are situated in field IIIb, indicating the existence of real negative cerium anomalies.

Anomalies of cerium values in the separated phosphate particles under investigation show an average of -0.22 in the lower sub-layer, -0.20 in the main sub-layer, and -0.24 in the upper sub-layer, as displayed in Table 7. While all samples display similar cerium anomaly values indicative of sub-oxic conditions, there is a clear increase of relatively reducing conditions from the lower sub-layer to the main sub-layer, characterized by a higher presence of glauconite particles and subsequent REE contents, followed by a decline in the upper sub-layer with diminishing glauconite and REE contents. This observation indicates that glauconitization involves a higher degree of reducing conditions compared to the conditions present during phosphatization processes. This is also supported by the presence of pyrite in the main sub-layer (cf. Fig. 44).

Table. 7: Ce and Eu anomalies of the three sub-layers of the Bled El Hadba phosphorite particles (gl: glauconite, pl: pellet, cop: coprolite).

Particle	Spot posit.	Ce/Ce*	Eu/Eu*	Ce Anom.
Upper sub-layer				
gl	Rim	0.57	2.40	-0.25
	Core	0.57	2.19	-0.25
gl	Core	0.57	2.24	-0.24
pl	Core	0.62	1.33	-0.21
	Rim	0.57	1.49	-0.24
pl	Core	0.45	1.31	-0.35
	Rim	0.44	1.75	-0.36
pl	Core	0.62	1.29	-0.21
cop	Core	0.59	1.12	-0.23
	Rim	0.64	2.24	-0.19
cop	Core	0.62	1.32	-0.21
	Rim	0.60	1.38	-0.22
cop	Core	0.60	1.23	-0.22
Average		0.57	1.64	-0.24
SD		0.06	0.46	0.05
Main sub-layer				
gl	Core	0.63	1.95	-0.20
	Rim	0.68	3.38	-0.17
gl	Core	0.64	2.42	-0.19
	Rim	0.62	3.34	-0.21
pl	Core	0.58	1.36	-0.24
	Rim	0.60	2.11	-0.22
pl	Core	0.62	1.60	-0.20
	Rim	0.70	2.17	-0.16
pl	Core	0.62	1.23	-0.21
cop	Core	0.64	1.25	-0.20
	Rim	0.64	1.30	-0.19
cop	Core	0.67	1.10	-0.18
	Rim	0.64	1.03	-0.19
Average		0.64	1.86	-0.20
SD		0.03	0.80	0.02
Lower sub-layer				
gl	Core	0.56	1.15	-0.25
	Rim	0.54	1.42	-0.26
gl	Rim	0.57	1.66	-0.24
	Core	0.59	1.55	-0.23
gl	Core	0.64	1.41	-0.20
pl	Core	0.61	1.49	-0.21
	Rim	0.65	1.97	-0.19
pl	Core	0.55	1.09	-0.26
	Rim	0.52	1.17	-0.29
pl	Core	0.62	1.23	-0.21
cop	Core	0.65	1.34	-0.18
	Rim	0.66	1.49	-0.18
cop	Core	0.64	1.54	-0.19
Average		0.60	1.42	-0.22
SD		0.05	0.24	0.04

The Nd contents *vs* Ce anomaly shown on Figure 54, not only indicates the sub-oxic conditions for the deposition of the Bled El Hadba glauconite-rich phosphorites but also indicates a relatively slow sedimentation rate. This is associated with glauconitization processes, Nd- and REE-enrichment. These observations are consistent with similar data obtained from particles separates from the Kef Essenoun and El Kouif phosphorite deposits located in the northern basin, as reported by Kechiched et al. (2018). Wright et al. (1987) further suggested that Nd contents can serve as a proxy for sedimentation rates, with higher Nd contents indicating slower rates typical of deep-water sediments and facilitating a greater uptake of REEs.

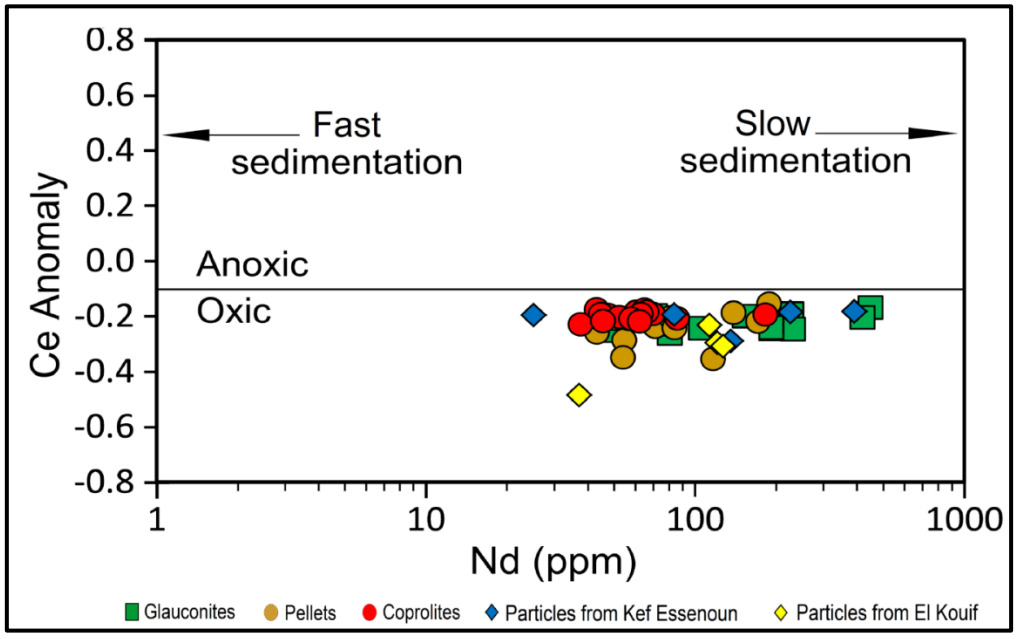

Fig. 54: The Ce anomaly vs. Nd diagram (after Wright et al., 1987)

V.3.2. Europium anomaly

The trivalent Eu^{3+} can be converted into a divalent Eu^{2+} ion under reducing conditions prevalent in near-surface systems (Brookins, 1989; Shields and Stille, 2001). Nevertheless, the manifestation of a positive Eu anomaly could be attributed to multiple factors beyond a reducing environment, such as hydrothermal fluids, pH levels, and temperature fluctuations

(He et al., 2022). Moreover, the presence of Ba is acknowledged for its potential to create irregularities in Eu readings when conducting ICPMS assessments, primarily due to the spectroscopic overlap between BaO+ and BaOH+ ions, as discussed by Shields and Stille (2001). To circumvent this challenge, Taylor (2001) recommended the application of dry plasma in laser ablation procedures for sample examinations. Consequently, the Eu anomalies identified in this study remain unaffected by potential sources of interference. Elevated temperatures and hydrothermal processes have the capacity to induce positive Eu anomalies by promoting the reduction of Eu^{3+} to Eu^{2+}, as evidenced in previous research (e.g., Bau et al., 2010; Michard et al., 1983; Schmidt et al., 2007; Stalder and Rozendaal, 2004). The precise contribution of hydrothermal fluids to generate positive Eu anomalies in phosphorite formation within marine sedimentary rocks remains uncertain (Zhu et al., 2014; Joosu et al., 2015). Positive Eu anomalies in phosphorites are, therefore, a result of highly reducing conditions during diagenesis, as stated by Kidder et al. (2003). Conversely, Soyol-Erdene and Huh (2013) argued against the presence of Eu anomalies under extreme reducing conditions during diagenesis. The coexistence of positive Eu anomalies and negative Ce anomalies has been attributed to upwelling and mixing between oxic shallow seawaters and organic-rich anoxic seawaters (Abedini and Calagari, 2017), as well as the 'tetrad' effect proposed by McLennan (1994).

In the studied Bled El Hadba phosphorites, positive anomalies in Eu are observed in the different phosphorite sub-layers, with mean values of 1.42 ± 0.24 in the lower sub-layer, 1.86 ± 0.80 in the main sub-layer, and 1.64 ± 0.46 in the upper sub-layer (see Table 7). These values exhibit consistently higher values in the rims of the phosphorite particles compared to the cores. Furthermore, there is a significant positive correlation between Eu/Eu* and ΣREE (r = 0.98, $p < 0.0001$) (Fig. 55). This suggests a strong relationship between positive Eu anomaly values and REE enrichment.

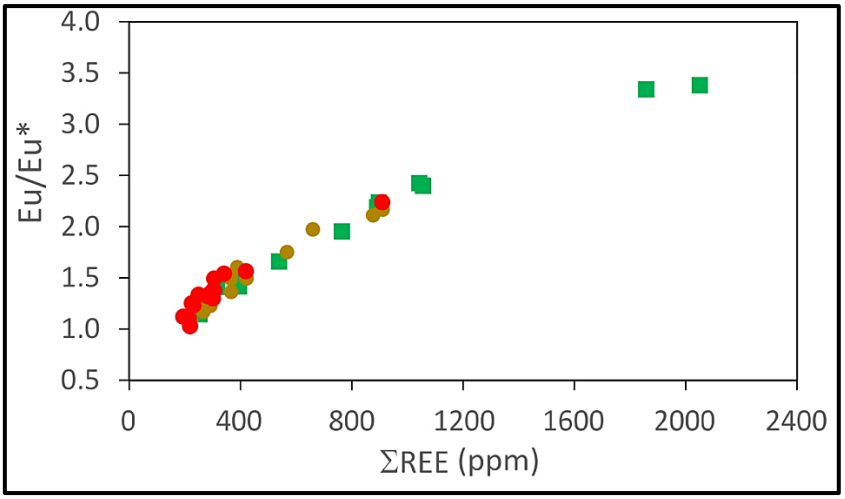

Fig. 55: REE vs. Eu/Eu* variations in the Bled El Hadba phosphorite particles indicating very strong positive correlation.

Moreover, the highest Eu anomaly values are observed in glauconites, along with the highest REE contents. This indicates that, despite both phosphatization and glauconitization processes occurring just before and during early diagenesis, the latter occurred after phosphatization and developed under relatively reducing conditions. Given that phosphorites are expected to have formed under oxic conditions resulting in negative Eu anomalies, the shift towards positive anomalies in Bled El Hadba phosphorite particles is more likely due to the accumulation environment (early diagenesis) rather than the formational conditions, especially when considering this deposit as a reworked phosphorite, akin to certain Tethyan phosphorites in northern Africa (e.g., Tunisian and Egyptian deposits; Baioumy and Farouk, 2022).

V.3.3. Yttrium anomaly

The positive anomalies of Y and high La/Nd ratios in seawater remain unaffected by variations in redox conditions. Nevertheless, their values can be employed as valuable indicators to evaluate the influence of diagenesis in the depositional environment (Bau, 1996; Fazio et al., 2007; Shields and Stille, 2001; Zhang et al., 1994). Shields and Stille (2001) have reported that the Y/Y* and La/Nd ratios in contemporary seawater range from 1.5 to 2.3 and 0.8 to 1.3, respectively. The Bled El Hadba phosphorites exhibit Y/Y* ratios ranging from 1.41

to 2.16 (mean: 1.63), while the La/Nd ratios display variation between 1.01 and 1.80 (mean: 1.28). Analysis of Figure 56 reveals a clear positive correlation between the Y anomaly and La/Nd ratios (r = 0.86, p < 0.0001), suggesting that Y and La exhibit similar behavior in pore waters. Furthermore, the Ce anomaly also demonstrates negative correlations with both parameters (rCe/Ce* vs. Y/Y* = -0.84; rCe/Ce* vs. La/Nd = -0.73; p < 0.0001) as depicted in Figure 56a and b. These trends consistently indicate early diagenesis. Although the Y/Y* and La/Nd ratios fall within the range observed in seawater (Fig. 56c), the analyzed particles mainly plot in the lower part of the seawater field, indicating progressive evolution towards early diagenesis.

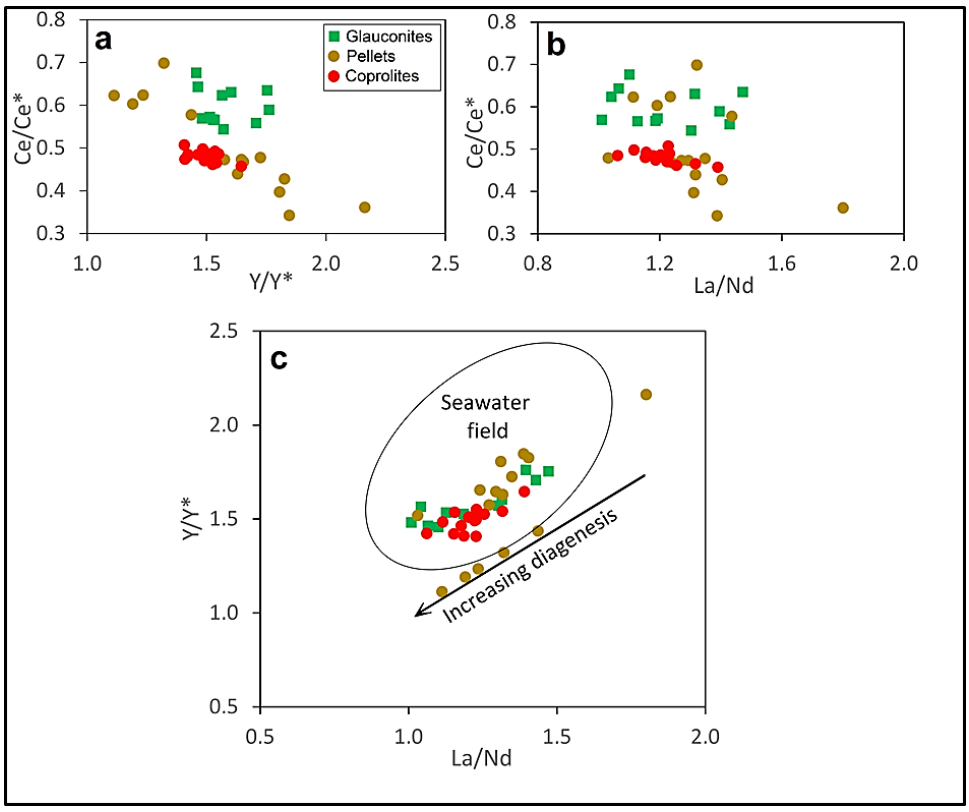

Fig. 56: Binary diagrams of (a) Y/Y* vs. Ce/Ce*, (b) La/Nd vs. Ce/Ce*, and (c) La/Nd vs. Y/Y* (Fazio et al., 2007).

V.4. Trace elements as redox trackers

The solubility of V and Cr in water is observed under oxic conditions, leading to their accumulation in sediments deposited in reducing environments (Piper, 1994). The data presented in Table 2 (cf. chapter IV) show that the Bled El Hadba phosphorites exhibit an enrichment of V and Cr, where their concentrations display significant ranges of variation, from 42.41 to 186.85 ppm and 138.15 to 319.51 ppm, respectively. Furthermore, the data presented in Table 4 (cf. chapter IV) clearly indicate that the glauconite particles of the phosphorites exhibit a higher enrichment of these two elements. The substitution of Cr for Al in glauconites is evidenced by the strong positive correlation between Cr and Al_2O_3 ($r = 0.94$, $p < 0.0001$) (Fig. 57a). On the other hand, V is likely to be associated with organic matter due to the incorporation of V^{4+} into porphyrins, and exhibits a relatively weaker positive correlation with Al_2O_3 ($r = 0.76$, $p = 0.0042$) (Fig. 57b). Furthermore, the deposition of sediments under reducing conditions results in the concentration of V. This is supported by previous studies conducted by Emerson and Huested (1991) and Shaw et al. (1990). Additionally, the enrichment of Cr and V contents are accompanied by REE enrichment in the studied phosphorite particles, with glauconites displaying the highest enrichment levels (Fig. 57c, d).

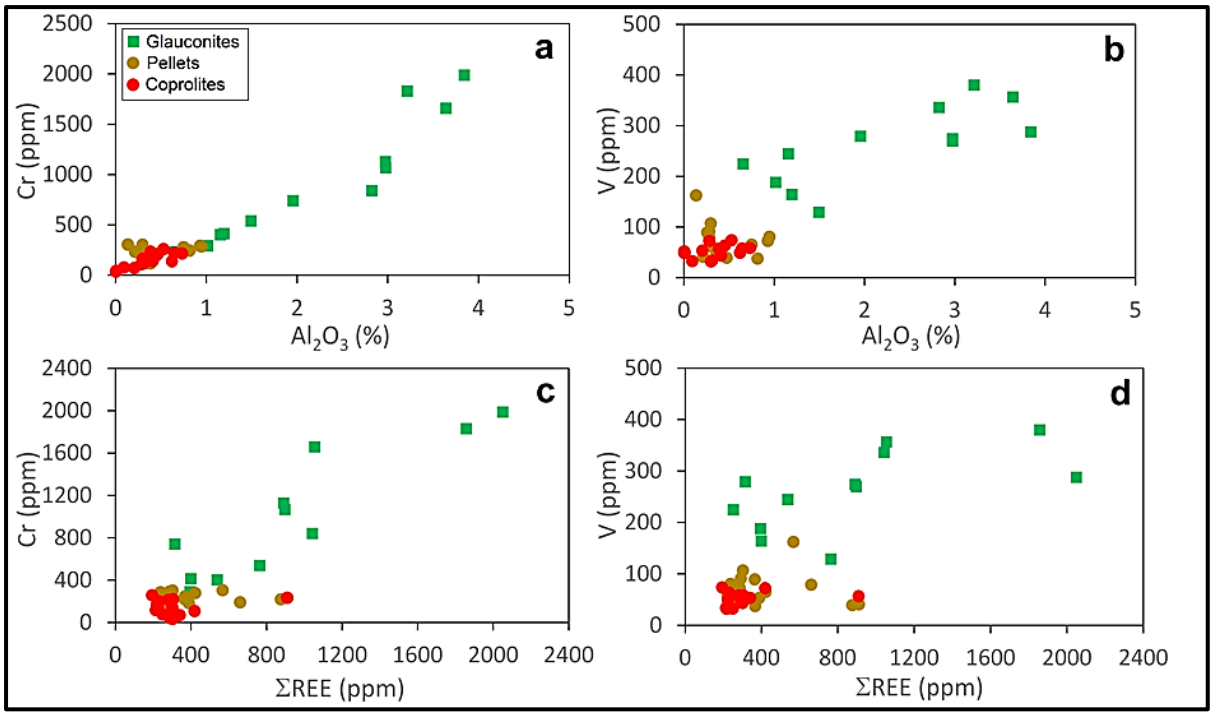

Fig. 57: Al_2O_3 vs. Cr and Al_2O_3 vs. V diagrams (a and b respectively) and ΣREE vs. Cr and ΣREE vs. V diagrams (c and d respectively).

Piper (1994) emphasized the significance of the V/Cr ratio in seawater, which is about 0.12, suggesting potential variations in redox conditions. Sediments accumulating under mildly denitrifying conditions may exhibit significantly higher ratios. This observation support to the idea that glauconitization likely occurred in a more reducing environment compared to the formation conditions of pellets and coprolites.

Glauconite particles are characterized by higher concentrations of Ni and Co compared to pellets and coprolites, as shown in Table 4 (cf. chapter IV). The Ni/Co ratio is used as a redox proxy, as discussed by Dill (1986). High Ni/Co values (>7) indicate reducing conditions, while ratios between 5 and 7 suggest a sub-oxygen-rich environment, and values <5 indicate an oxic environment (Gao et al., 2023). The Ni/Co ratios in glauconites range from 9.97 to 44.8, whereas in pellets and coprolites, they vary from 1.47 to 9.22. This disparity clearly indicates that glauconites formed in a more reducing environment.

Conclusion

The REE + Y normalized patterns demonstrate that glauconite particles, represented by hat-shaped patterns, display a notable enrichment in MREE when compared to coprolites and pellets. In contrast, the latter exhibit only a slight enrichment in HREE. This disparity suggests that the glauconite particles reflect the influence of pore water, while the coprolites and pellets reflect a seawater influence, as evidenced by their seawater-like patterns.

The Bled El Hadba phosphorites reveal an evolutionary trajectory in their deposition and diagenesis, transitioning from oxic to sub-oxic conditions. This is substantiated by the presence of negative Ce anomalies, modestly positive Eu anomalies, and distinctly positive Y

anomalies. Moreover, the concentrations of trace elements that are sensitive, specifically V, Cr, Ni, and Co, provide additional support for this transition.

CHAPTER VI

RARE EARTH ELEMENTS ECONOMY

CHAPTER Ⅵ

RARE EARTH ELEMENTS ECONOMY

Over the past few years, the global economy has encountered numerous economic shortages concerning the supply risk of different raw materials, particularly rare earth elements (REE). This risk has been exacerbated by the significant demand for REE, driven by their diverse applications in advanced technologies and sustainable energy, as well as various geostrategic concerns. Additionally, current economic projections suggest a possible disparity between demand and supply by the year 2100 (Wang et al., 2020). The dominant sources of typical REE-minerals, such as monazite and bastnasite, play a crucial role in the production of REEs from significant deposits in China, including Bayan Obo and ionadsorption clay-type (e.g., Humphries, 2010; Xiao et al., 2016; Wang et al., 2017; Long et al., 2010; Emsbo et al., 2015). Nevertheless, with the current state of the REE market, all potential resources of REEs, including those with lower concentrations, are now under scrutiny for research and development.

VI.1. REEs global production and reserves

Over the course of 25 years, the mining output of rare earths has almost tripled, increasing from 80,000 tonnes in 1995 to 213,000 tonnes in 2019. This sector exhibits a notable level of concentration, with a Herfindahl-Hirschman Index (HHI) of 4,199. China stands out as the primary producer, accounting for 62% of the total output, while the United States follows with 12%, Russia with almost 10.5%, and Myanmar, a recent entrant to the market, holds a 10% share. Excluding China, the main group of countries does not mirror the distribution of reserves, which are mainly concentrated in three countries - China, Brazil, and Vietnam -

holding over three quarters of the total reserves estimated at 120 million tonnes by USGS (fig. 58). This distribution is not as consolidated as the mining production of rare earths, which has an HHI of 2,317. Russia and India also possess substantial reserves.

In recent times, there has been a significant shift in the industry. This transformation has been primarily driven by the revival of exploration projects that were initiated in the early 2010s, a period marked by concerns over a potential scarcity of rare earths in the global market. A total of 98 million tonnes of rare earth oxide equivalents have been discovered in Canada, Greenland, as well as in four African nations (Kenya, Tanzania, Malawi, South Africa) (Paulick and Machacek, 2017). The year 2018 saw Burundi making its start in the rare earth market, emerging as the first – and currently the sole – producer of these elements in Africa. The United States has shown a keen interest in Greenland, as evidenced by a notable purchase offer. This interest could potentially lead to a diversification of rare earth supply sources. In June 2019, the US State Department announced a partnership with the Greenlandic Ministry of Mineral Resources and Labor to encourage investment and mining exploration in the Gadar province, an area rich in various metals, including rare earth elements.

VI.2. Phosphorites as REEs resources

Coal and phosphorites, for instance, are being seriously considered as alternative REE sources (Balaram, 2022) and have garnered increased attention due to the diminishing traditional deposits, environmental issues, and supply constraints (e.g., Long et al., 2010; Emsbo et al., 2015). The North Africa region is home to a considerable number of resources, with an estimated 69 billion metric tons of phosphorites (USGS, 2020). Globally, phosphorites typically contain an average of 0.046 wt% of rare earth elements (Li, 2000). The rare earth element content in phosphorite deposits varies significantly depending on their geographic distribution and stratigraphic positions (Ferhaoui et al., 2022).

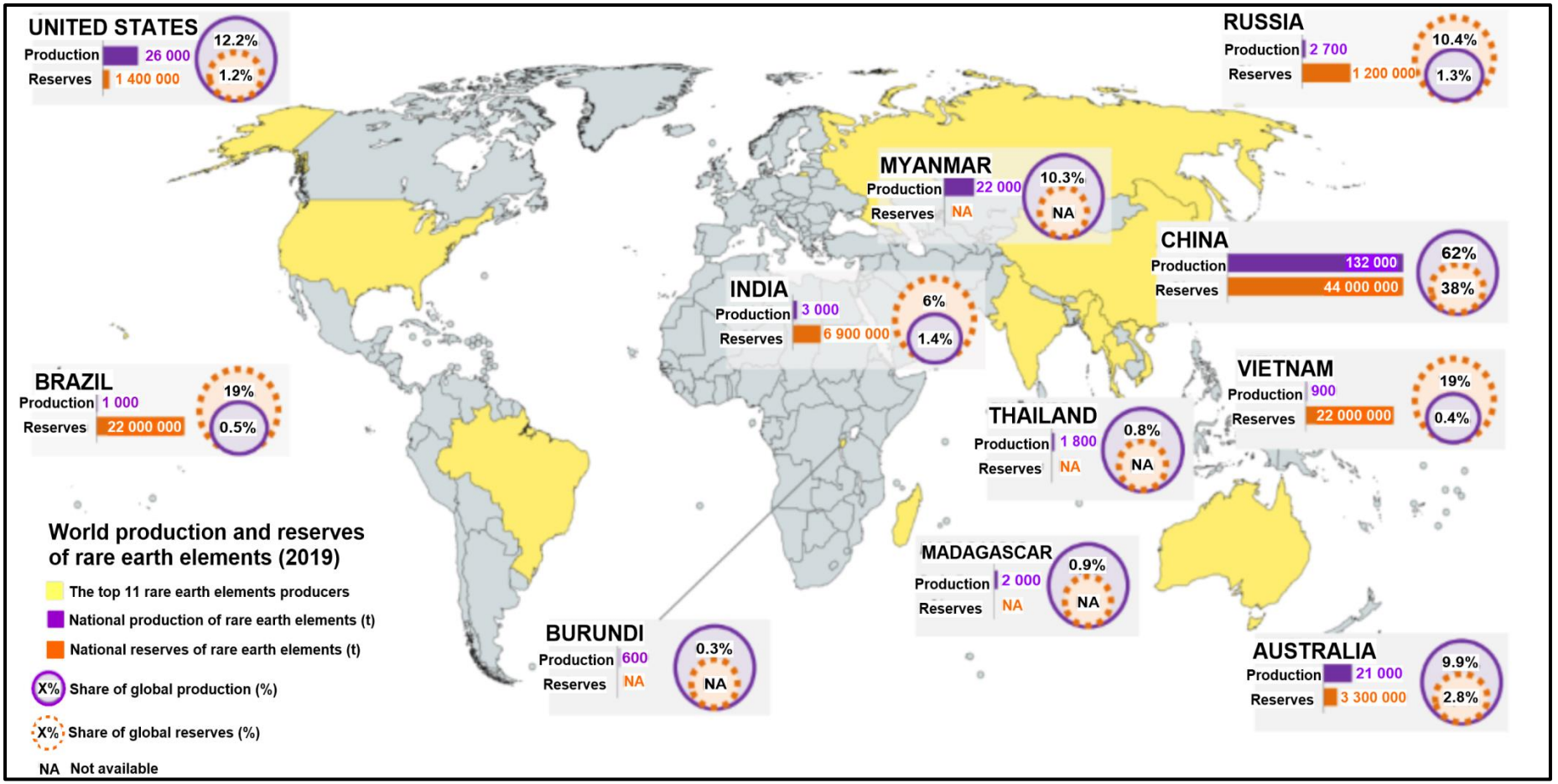

Fig. 58: World production and reserves of Rare Earth Elements (2019) **(**U.S.G.S, 2020**).**

Phosphorite deposits within the Algerian-Tunisian region are characterized by their high enrichment in rare earth elements (Buccione et al., 2021). Previous studies on phosphorites containing rare earth elements (REEs) by various researchers (e.g., Emsbo et al., 2015; Valetich et al., 2022; Baioumy and Farouk, 2022; Ferhaoui et al., 2022; Ahmed et al., 2022) have identified a promising REE reserve suitable for extraction. The calculation of the outlook coefficient (Coutl) for REEs can be achieved through the utilization of the formula of Seredin (2010). This formula involves dividing the sum of Nd, Eu, Tb, Dy, Er, and Y by the sum of Ce, Ho, Tm, Yb, and Lu. Several recent studies conducted by Buccione et al. (2021), Valetich et al. (2022), Ahmed et al. (2022), and Ferhaoui et al. (2022) have demonstrated the significant potential of phosphorites as phosphate ores for the extraction of REEs. These findings provide strong evidence supporting the notion that phosphorites hold great promise in the realm of REE extraction.

VI.3. Perspectives and recommendations

The present study of the Bled El Hadba phosphorite deposit shows that glauconites contain the highest ΣREE concentrations (minimum = 252 ppm; maximum = 2050, average = 872 ± 555 ppm) when compared to the co-existing particles (pellets and coprolites). These glauconites are also identified as the most enriched particles within Tethyan deposits (Fig. 59a).

A notable characteristic of the Bled El Hadba deposit, which displays relatively low P_2O_5 levels, is its hosting of the most glauconite-rich phosphorites among all documented deposits in the Algeria-Tunisian region. Furthermore, aside from the high concentrations of Rare Earth Elements (REE), the phosphate particles derived from this particular deposit exhibit C_{outl} values ranging from 1.46 to 2.69, with the percentage of critical elements in ΣREE + Y varying from 41.88% to 52.64% (Table 8). These findings, as indicated by Seredin (2010) (Fig. 59b), suggest promising REE resources.

The relatively high iron contents in glauconites (~4 to ~8%) could potentially serve as an advantage for facilitating magnetic separation and REE extraction processes. It is strongly advised to conduct an estimation of the quantity of glauconitized particles, along with their REE content, in the Bled El Hedba raw phosphorites through the use of geostatistical modeling.

Table 8: Coutl and REY def (%) parameters of the three sub-layers of Bled El Hadba phosphorite phosphate particles (gl: glauconite, pl: pellet, cop: coprolite).

Particle	Spot posit.	Coutl	REYdef (%)
Upper sub-layer			
gl	Rim	1.97	47.35
	Core	1.84	45.61
gl	Core	1.80	45.30
pl	Core	1.73	45.31
	Rim	1.95	47.75
pl	Core	2.52	51.31
	Rim	2.69	52.64
pl	Core	1.70	44.92
cop	Core	1.77	45.70
	Rim	1.70	45.39
cop	Core	1.67	44.47
	Rim	1.73	45.26
cop	Core	1.71	44.78
Average		1.91	46.60
SD		0.33	2.58
Main sub-layer			
gl	Core	1.53	42.36
	Rim	1.50	42.65
gl	Core	1.53	42.51
	Rim	1.72	44.85
pl	Core	1.67	43.71
	Rim	1.82	46.30
pl	Core	1.62	43.88
	Rim	1.50	43.30
pl	Core	1.59	43.43
cop	Core	1.54	42.68
	Rim	1.55	42.89
cop	Core	1.46	41.88
	Rim	1.54	42.97
Average		1.58	43.34
SD		0.10	1.17
Lower sub-layer			
gl	Core	1.66	42.90
	Rim	1.81	44.78
gl	Rim	1.68	43.36
	Core	1.65	43.36
gl	Core	1.73	45.56
pl	Core	1.93	48.39
	Rim	1.97	49.30
pl	Core	2.05	48.43
	Rim	2.29	50.53
pl	Core	1.65	44.38
cop	Core	1.59	43.88
	Rim	1.56	43.64
cop	Core	1.60	43.77
Average		1.78	45.56
SD		0.22	2.64

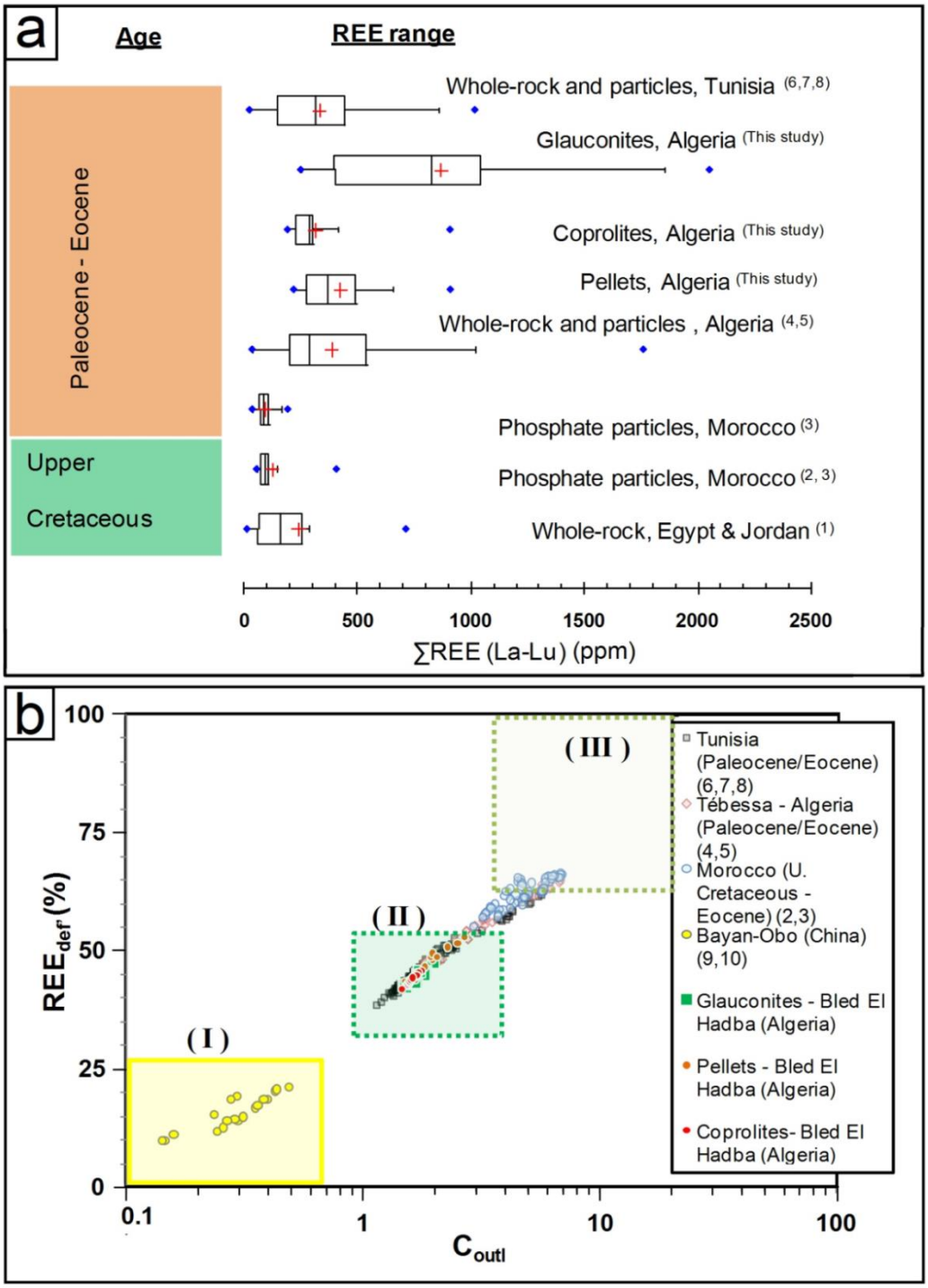

Fig. 59: (**a**): comparative analysis of the REE concentrations in Bled El Hedba phosphorite particles relative to those found in both individual particles and whole-rock samples from various Tethyan phosphorite deposits. (**b**): classification of rare earth elements (REEs) found in phosphorite deposits is achieved through the examination of the outlook coefficient (Coutl) compared to the percentage of critical elements within the total REE content (REEdef) (Seredin, 2010). **I**: unpromising, **II**: promising, and **III**: highly promising. Data are from: (1) Baioumy (2011), (2) McArthur and Walsh (1984), (3) Kocsis et al. (2016), (4) Kechiched et al. (2018), (5) Kechiched et al. (2020), (6): Ounis et al. (2008), (7): Garnit et al. (2012), (8): Garnit et al. (2017), (9): Zhang et al. (2017), (10): Hou et al. (2020).

CONCLUSION

CONCLUSION

The Bled El Hadba phosphorite deposit is located in the Djebel Onk region, which constitutes part of the Tebessa region within the Eastern Saharan Atlas. The Tebessa region, known for its complex geological structures, emerges as a captivating area for investigation. The region is mainly composed of Mesozoic-Cenozoic formations, exhibiting the influence of a significant tectonic system characterized by Triassic uplift through overlying formations (diapirism), subsidence, a network of faults, collapse basins, and considerable folding. These tectonic processes contribute to the creation of NE-SW-oriented anticline and syncline structures.

In the south of this region, the Djebel Onk anticline is characterised by a stratigraphic sequence of rock layers spanning the Cretaceous to the Quaternary periods. Of particular interest, the Upper Thanetian stage represents the deposition of significant phosphorite sediments with about 30 meters in thickness, and exhibits a continuous stratigraphic layer from Kef Essenoun in the west region to Bled El Hadba in the east of Djebel Onk region.

The geological structure of the Bled El Hadba deposit shares remarkable similarities with that of Kef Essenoun and Djemi-Djema, encompassing stratigraphic formations from the Paleocene to the quaternary period. The upper thanetian phosphatic layer at Bled El Hadba displays morphological features that closely resemble those observed in other deposits, such as those of Kef Essenoun and Djemi Djema. This phosphatic layer is sub-divided into three distinct sub-layers: (1) the lower sub-layer is distinguished by its high hardness, dominated by dolomitic matrix; (2) The main sub-layer is relatively friable due to the presence of clayey along with the scarce carbonaceous matrix; (3) The upper sub-layer is exceptionally hard,

attributed to the dolomitic cement that gives a grayish, beige, and dark gray color to this phosphorite sub-layer.

The petrographic study of the Bled El Hadba phosphorites shows several characteristics: (1) the dominant phosphatic particles are pellets, followed by coprolites and rare gloconites; (2) the lower and upper sub-layers exhibit lower contents of phosphatic particles compared to the main sub-layer; (3) the lower and upper sub-layers contain carbonaceous cement, mainly composed of dolomite and/or calcite, which contributes to their notable hardness. In contrast, the main sub-layer displays a combination of a clayey matrix and carbonaceous cement, resulting in a relatively friable texture; (4) there is a gradual increase in the presence of glauconite from the lower to upper sub-layers.

The X-ray diffraction (XRD) examination shows that: (1) the main minerals consist of fluorapatite, hydroxylapatite, and dolomite, whereas calcite, gypsum, and quartz are minor components; (2) the principal sub-layer exhibits a greater abundance of apatite minerals (fluorapatite and hydroxylapatite) compared to the lower and upper sub-layers, where dolomite prevails.

The geochemical data show that: (1) the Bled El Hadba phosphorites display a relatively lower P_2O_5% in comparison to Kef Essenoun and Djemi Djema; (2) There is a notable abundance of trace and rare earth elements, indicating high levels of substitution and adsorption mechanisms of these elements; (3) rare earth elements (REEs) are more enriched in glauconites than in co-existing particles (pellets and coprolites), exceeding 2000 ppm; (4) In the grain structure, there is a marked disparity in the concentration of these chemical elements between the rims and cores, with a clear trend of decreasing contents from the rims towards the cores. On the other hand, the P_2O_5 content shows an opposite pattern, being more abundant in the cores and decreasing towards the rims. Based on these observations, it can be inferred that phosphatization occurred prior to glauconitization, offering an explanation for these outcomes.

The patterns obtained from normalizing the REE+Y data reveal (1) a notable enrichment of MREE in glauconite particles, which is evideced by their distinctive hat-shaped patterns. In contrast, coprolites and pellets exhibit lower HREE contents. Consequently, the former can be attributed to the influence of pore water uptake, while the latter exhibit patterns resembling those found in seawater, indicating a seawater influence in their REE uptake; (2) The Ce anomalies show negative values, while the Eu anomalies display slight positive values, and the Y anomalies show a significant positive trend. These values, along with the sensitive trace elements, such as Cr, V, Ni, and Co, contents indicate a transition from oxic to sub-oxic environments during the formation and diagenesis of the Bled El Hadba phosphorites.

The significance of exploring phosphorites as potential substitutes for rare earth elements (REE) has grown due to the depletion of conventional deposits, environmental concerns, and supply limitations. Notably, phosphorite deposits in the Algerian-Tunisian region contain a substantial amount of rare earth elements (REEs). Previous studies by many researchers have successfully identified a promising reserve of REEs within phosphorites, highlighting their potential for extraction. This assertion is further supported by the current investigation, which reveals that the phosphatic particles of the Bled El Hadba phosphorites exhibit C_{outl} values ranging from 1.46 to 2.69, and the proportion of essential elements in ΣREE+Y fluctuates between 41.88% and 52.64%. These data indicate potentially promising REE resources.

REFERENCES

REFERENCES

Aba-Hussain, A., Al-Bassam, K., Al-Rawi, Y., 2010. Rare earth elements geochemistry of some Paleocene carbonate fluorapatites from Iraq. Iraqi Bullet. Geol. Mining 6, 81–94.

Abed, M., Jaber, O., Alkuisi, M., Sadaqah, R., 2016. Rare earth elements and uranium geochemistry in the Al-Kora phosphorite province, Late Cretaceous, northwestern Jordan. Arab. J. Geosci. 9, 1–19. https://doi.org/10.1007/s12517-015-2135-6.

Abedini, A., Calagari, A.A., 2017. REEs geochemical characteristics of lower Cambrian phosphatic rocks in the Gorgan-Rasht Zone, northern Iran: implications for diagenetic effects and depositional conditions. J. Afr. Earth Sci. 135, 115–124. https://doi.org/10.1016/j.jafrearsci.2017.08.018.

Abou El-Anwar, E.A., Mekky, H.S., Abd El Rahim, S.H., Aita, S.K., 2017. Mineralogical, geochemical characteristics and origin of late cretaceous phosphorite in Duwi formation (Geble Duwi mine), Red Sea region, Egypt. Egypt. J. Pet. 26, 157–169. https://doi.org/10.1016/j.ejpe.2016.01.004.

Abu-Eishah S. I., Muthaker M. et Touqan N. (1991): A new technique for the beneficiation of low-grade carbonate-rich phosphate rocks by digestion with dilute acetic acid solutions: pilot plant testing results. Minerals Engineering, Vol. 4, No. 5/6, pp. 573-586.

Ahmed, H.A., Aseri, A.A., Ali, K.A., 2022. Geological and geochemical evaluation of phosphorite deposits in northwestern Saudi Arabia as a possible source of trace and rare-earth elements. Ore Geol. Rev. 144, doi : 104854.oregeorev.2022.104854.

Al-Bassam, K., Rambousek, P., ˇCech, S., 2021. REE-rich Turonian phosphates in the Bohemian Cretaceous basin, Czech Republic: Assessment as source of critical elements and implications for future exploration. Minerals 11, 246. https://doi.org/ 10.3390/min11030246.

Al-Hobaib, A.S., Baioumy, H.M., Al-Ateeq, M.A., 2013. Geochemistry and origin of the Paleocene phosphorites from the Hazm Al-Jalamid area, northern Saudi Arabia. J. Geochem. Explor. 132, 15–25. https://doi.org/10.1016/j.gexplo.2013.04.001.

Altschuler, Z.S., 1980. The geochemistry of trace elements in marine phosphorites, part I. Characteristics abundances and enrichment. Soc. Econ. Paleontol. Miner. Spec. Publ. 29, 19–30. https://doi.org/10.2110/pec.80.29.0019.

Altschuler, Z.S., Berman, S., Cuttita, F., 1967. Rare earths in phosphorites-geochemistry and potential recovery. In: U.S. G. S. Professional Paper, 575B, pp. B1–B9. https://doi.org/10.3133/ofr663.

Auer, G., Markus, R., Christoph, A.H., Werner, E.P., 2017. The impact of transport processes on rare earth element patterns in marine authigenic and biogenic phosphates. Geochim. Cosmochim. Acta 203, 140–156. https://doi.org/10.1016/j. gca.2017.01.001.

Baioumy H.M. (2005): Preliminary data on cadmium and arsenic geochemistry for some phosphorites in Egypt. Journal of African Earth Sciences 41, pp. 266–274.

Baioumy, H., Farouk, S., 2022. The geochemical and economic significance of REE in the Upper Cretaceous-Eocene Tethyan phosphorites. J. Afr. Earth Sci. 194, 104635 https://doi.org/10.1016/j.jafrearsci.2022.104635.

Baioumy, H.M., 2011. Rare earth elements and sulfur and strontium isotopes of upper Cretaceous phosphorites in Egypt. Cretac. Res. 32, 368e377. https://doi.org/ 10.1016/j.cretres.2011.01.008.

Balaram, V., 2022. Rare earth element deposits - sources, and exploration strategies. J. Geol. Soc. India 98, 1210–1216. https://doi.org/10.1007/s12594-022-2154-3.

Banu M., 2005. Mise en forme d‘apatites nanocristallines : céramiques et ciments. Thèse de Doctorat. Institut National Polytechnique de Toulouse, France, 183p.

Baturin, G. N., 1982. Phosphorites on the sea floor: Origin, composition and distribution. Elsevier, Amsterdam, 343p

Baturin G.N. et A. V. Kochenov (2000) : Uranium in Phosphorites. Lithology and Mineral Resources, Vol. 36, No. 4, 2001, pp. 303–321. Translated from Litologiya I Poleznye Iskopaemye, No. 4, 2001, pp. 353–373.

Bau, M., 1996. Controls on fractionation of isovalent trace elements in magmatic and aqueous systems: evidence from Y/Ho, Zr/Hf and lanthanide tetrad effect. Contrib. Mineral. Petrol. 123, 323–333. https://doi.org/10.1007/s004100050159.

Bau, M., Dulski, P., 1996. Distribution of yttrium and rare-earth elements in the Penge and Kuruman iron-formations. Transvaal Supergroup. Precambr. Res. 79, 37–55. https://doi.org/10.1016/0301-9268(95)00087-9.

Bau, M., Balan, S., Schmidt, K., Koschinsky, A., 2010. Rare earth elements in mussel shells of the Mytilidae family as tracers for hidden and fossil high-temperature hydrothermal systems. Earth Planet. Sci. Lett. 299 (3), 310–316. https://doi.org/10.1016/j.epsl.2010.09.011.

Bechade E., 2008. Nouveaux matériaux de structure apatite : Synthèse, structure et mécanismes de conduction ionique. Thèse de Doctorat. Université de Limoges, France, 250p.

Ben Hassen, A., Trichet, J., Disnar, J.R., 2010. Pétrographie et géochimie comparées des pellets phosphatés et de leur gangue dans le gisement phosphaté de Ras-Draaa (Tunisie). Implications sur la gen`ese des pellets phosphatés. Swiss J. Geosci. 103 (3),457–473. https://doi.org/10.1007/s00015-010-0029-x.

Benabdeslam, N., Bouzidi, N., Atmani, F., Boucif, R., Sakhri, A., 2018. The effect of the parameters of the grinding on the characteristics of the deposit phosphate ore of Kef Es Sennoun, Djebel Onk-T´ebessa, Algeria. Int. J. Mater. Metall. Eng. 12 (7), 319–326. https://doi.org/10.5281/zenodo.1317342.

Benarous, S., Azbouche, A., Boumehdi, B., Chegrouche, S., Atamna, N., Khelifi, R., 2022. Establishing a pre-mining baseline of natural radionuclides distribution and radiation hazard for the Bled El-Hadba sedimentary phosphate deposits (North-Eastern Algeria). Nucl. Eng. Technol. 54 (11), 4253–4264. https://doi.org/10.1016/j.net.2022.06.006.

Bertholus M. et Defranceschi M., 2004. Les apatites des phosphates naturels. Techniques de l'Ingénieur AF 6610.

Bezzi, N., Merabet, D., Benabdeslem, N., Arkoub, H., 2001. Caracterisation physicochimique du minerai de phosphate de Bled El-Hadba - T´ebessa. Ann. Chim. Sci. Mater. 26 (6), 5–23.

Bezzi, N., Aïfa, T., Merabet, D., Pivan, J.Y., 2008. Magnetic properties of the Bled El Hadba phosphate-bearing formation (Djebel Onk, Algeria): Consequences of the enrichment of the phosphate ore deposit. J. Afr. Earth Sci. 50, 255–267. https://doi.org/10.1016/j.jafrearsci.2007.09.019.

Bezzi, N., Aïfa, T., Hamoudi, S., Merabet, D., 2012. Trace elements of Kef Es Sennoun natural phosphate (Djebel Onk, Algeria) and how they affect the various mineralurgic modes of treatment. Procedia Eng. 42, 1915–1927. https://doi.org/ 10.1016/j.proeng.2012.07.588.

Bosch, D., Hammor, D., Mechati, M., Fernandez, L., Bruguier, O., Caby, R., Verdoux, P., 2014. Geochemical study (major, trace elements and Pb-Sr-Nd isotopes) of mantle material obducted onto the North African margin (Edough Massif, North Eastern Algeria): Tethys fragments or lost remnants of the Liguro-Provençal basin? Tectonophysics 626, 53–68. https://doi.org/10.1016/j.tecto.2014.03.031.

Bouderiès A. (2008) : Etude géologique et géostatistique de l'Uranium (U) dans le gisemen de phosphate de Kef Essennoun, (Algérie Orientale). Mémoire Magistère, université d'Annaba, Algérie.

Boumala, D., Mavon, C., Belafrites, A., Tedjani, A., Groetz, J.E., 2018. Evaluation of radionuclide concentrations and external gamma radiation levels in phosphate ores and fertilizers commonly used in Algeria. J. Radioanal. Nucl. Chem. 317 (1), 501–510. https://doi.org/10.1007/s10967-018-5871-8.

Boumaza, B., Kechiched, R., Chekushina, T.V., 2021. Trace metal elements in phosphate rock wastes from the Djebel Onk mining area (T´ebessa, eastern Algeria): a geochemical study and environmental implications. Appl. Geochem. 127, 104910 https://doi.org/10.1016/j.apgeochem.2021.104910.

Brookins, D.G., 1989. Aqueous geochemistry of rare earth elements. In: Lipin, B.R., McKay, G.A. (Eds.), Geochemistry and Mineralogy of Rare Earth Elements, 21. Mineral. Soc. Amer., Rev. Mineral., pp. 201–225

BRGM-SOFREMINES (1993) : Étude de développement du gisement de phosphate de Djebel Onk (Algérie). Rapport d'expertise géologique. Auteur ; BRIAN J.P.avec la collaboration de PH.CORTIAL.

Buccione, R., Kechiched, R., Mongelli, G., Sinisi, R., 2021. REEs in the north Africa Pbearing deposits, paleoenvironments, and economic perspectives: a review. Minerals 11, 214. https://doi.org/10.3390/min11020214.

Burollet, P.F., Oudin, J.L., 1980. Paleocène et Eocène en Tunisie - pétrole et phosphate. In: Géologie comparée des gisements de phosphate et de pétrole. Memoires BRGM n◦ 24, pp. 205–216.

Capdecomme, L,. 1952. les phosphates alumineux de la region de Thiès (Senegal). CR. Ac. Sc. Paris, t. 235, n° 2, pp. 187-189,

Chaabani, F., 1995. Dynamique de la partie orientale du bassin de Gafsa au Crétacé et au Paléogéne : Etude minéralogique et géochimique de la série phosphatée Eocène. Université Tunis II, Tunisie, Tunisie méridionale. Thèse Doctorat d'Etat.

Chabou-Mostefai, S., 1987. ´Etude de la série phosphatée tertiaire du Djebel Onk. Thèse Doctorat. Université de Droit, d'Economie et des Sciences d'Aix-Marseille, France, Algérie, Stratigraphie, Pétrographie, Minéralogie et Analyse Statistique, p. 376.

Chaïrat C., 2005. Etude expérimentale de la cinétique et des mécanismes d'altération de minéraux apatitiques. Application au comportement d'une céramique de confinement d'actinides mineurs. Thèse de Doctorat, université de Toulouse III, France, 266 p.

Champetier, Y. et Joussemet, R. (1979): Découverte de nubéculaires et d'oncolithes en tant qu'éléments phosphatés. C. R. Acad. Sci. Paris, t. 288, D, n°7, p. 673- 67.

Cielensky., Benchernine. – EREM , 1987. Travaux de prospection et d'évaluation des phosphates dans la région de Bir El Ater. Rapport interne, EREM, 80p.

Cielensky, S., Benchernine, N., Watkowski, T., 1988. Travaux de prospection et d'évaluation des phosphates dans la région de Bir El Ater. Internal rapport, EREM, 103 p.

Cook, P. J., McElhinny, M. W., 1979. A reevaluation of the spatial and temporal distribution of sedimentary phosphate deposits in the light of plate tectonics. Economic Geology, 74 (2) 315-330 doi:10.2113/gsecongeo.74.2.315.

Cook, P.J. (1984): Spatial and temporal controls on the formation of phosphate deposits – a review. Phosphate Miner., 242–274.

Dassamiour M., 2006. Evaluation de la quantité du produit marchand à l'aide de méthodes géostatistiques dans les blocs d'exploitation du gisement de phosphate de Kef Es –Senoun (Algérie Orientale). Mém. de magister. Université Badj – Mokhtar. Annaba. 110 p.

Dassamiour, M ; Mezgahche, H ; Bouderies, A. (2010): Répartition des éléments en traces – Uranuim et Cadnuim, dans les minerais de phosphate de Djbel Onk. 1er Colloque international sur la géologie du Sahara algérien : ressources minérales, en hydrocarbure et en eau, Ourgla 2010.

Dassamiour, M., 2012. Eléments en traces et valorisation des minerais de phosphate du gisement de Kef Essennoun - Dj. Onk (Algérie Orientale). thèse de doctorat. Université Badji Mokhtar-Annaba- Algérie. 185 pages.

Dill, H., 1986. Metallogenesis of early Palaeozoic graptolite shales from the Graefenthal Horst (northern Bavaria - Federal Republic of Germany). Econ. Geol. 81, 889–903. https://doi.org/10.2113/gsecongeo.81.4.889.

Drummond, J.B.R., Pufahl, P.K., Porto, C.G. and Carvalho, M. (2015) Neoproterozoic peritidal phosphorite from the Sete Lagoas Formation (Brazil) and the Precambrian phosphorus cycle. Sedimentology, 62, 1978–2008.

Dussert, M.D., 1924. Les gisements Algériens de phosphate de chaux. Annales des mines, Dunodéd., Paris 12, 298 p.

E.RE.M. (1985 – 1987) : Travaux de prospection et d'évaluation des phosphates dans la région de Bir El Ater. Rapport EREM, 2 tomes : géologie, 50p. Prospection d'évaluation, 53p.

El Bamiki, R,. 2020. Étude géologique des occurrences phosphatées du Haut-Atlas Marocain : Compréhension des contrôles géologiques sur l'accumulation du phosphate. Autre. Université Montpellier ; Université Cadi Ayyad (Marrakech, Maroc), 2020. Français. NNT : 2020MONTG075.

Elderfield, H., Hawkesworth, C.J., Greaves, M.J., Calvert, S.E., 1981. Rare earth elements geochemistry of oceanic ferromanganese nodules. Geochim. Cosmochim. Acta 45, 513–528. https://doi.org/10.1016/0016-7037(81)90184-8.

Elliott J. C., 1994. Structure and chemistry of the Apatites and Other Calcium Orthophosphates, Elsevier, Amstedam,. Novembre 1980.

Emerson, S.R., Huested, S.S., 1991. Ocean anoxia and the concentrations of molybdenum and vanadium in seawater. Mar. Chem. 34, 177–196. https://doi.org/10.1016/ 0304-4203(91)90002-E.

Emsbo, P., Patrick, I., McLaughlin, P.I., Breit, G.N., Du Bray, E.A., Koenig, A.E., 2015. Rare earth elements in sedimentary phosphate deposits: solution to the global REE crisis? Gondwana Res. 27, 776–785. https://doi.org/10.1016/j.gr.2014.10.008.

FAO (2004): Use of Phosphate Rocks for Sustainable Agriculture. Fertilizer and plant nutrition bulletin 13. Food and agriculture organization of the united nations, Rome, 2004.

Fazio, A.M., Scasso, R.A., Castro, L.N., Carey, S., 2007. Geochemistry of rare earth elements in early-diagenetic miocene phosphatic concretions of Patagonia, Argentina: phosphogenetic implications. Deep-Sea Res. II 54, 1414–1432. https:// doi.org/10.1016/j.dsr2.2007.04.013.

Ferhaoui, S., Kechiched, R., Bruguier, O., Sinisi, R., Kocsis, L., Mongelli, G., Bosch, D., Ameur-Zaimeche, O., Laouar, R., 2022. Rare earth elements plus yttrium (REY) in phosphorites from the T´ebessa region (Eastern Algeria): Abundance, geochemical distribution through grain size fractions, and economic significance. J. Geochem. Explor. 241, 107058 https://doi.org/10.1016/j.gexplo.2022.107058.

Fernandez, F., Bosch, D., Bruguier, O., Hammor, D., Caby, R., Moni´e, P., Arnaud, N., Toubal, A., Galland, B., Douchet, C., 2016. Permo-Carboniferous and early Miocene geological evolution of the internal zones of the Maghrebides - new insights on the western Mediterranean evolution. J. Geodyn. 96, 146–173. https://doi.org/ 10.1016/j.jog.2015.10.001.

Fertilizers International 460, (2014). Phosphore: Fiche d'information minérale. Table Régionale de Concertation Miniere (TRCM) du Saguenay─Lac-Saint-Jean, 555, boul. de l'Université Chicoutimi, Qc, G7H 2B1 (418) 545-5011, poste 2509.

Fisher A.G. et Jérom D. (1973): Geochimistry of minerals containing phosphorus, in Environmental Phosphorus Handbook, 141p – John Wiley and Sons. New-York, London, Sydney, Toronto.

Flandrin, J. (1948). Contribution à l'étude stratigraphique du Nummulitique Algérien. Bull. Serv. Carte géol. Algérie, 2e série, n°19, 340p.

Fleet, M.E., Pan, Y., 1995. Site preference of rare earth elements in fluorapatite. Am. Mineral. 80, 329–335. https://doi.org/10.2138/am-1995-3-414.

Gao, L., Yang, R., Wu, T., Luo, C., Xu, H., Ni, X., 2023. Studies on geochemical characteristics and biomineralization of Cambrian phosphorites, Zhijin, Guizhou Province, China. PLoS One 18 (2), e0281671. https://doi.org/10.1371/journal. pone.0281671.

Gao, S., Liu, X., Yuan, H., Hattendorf, B., Günther, D., Chen, L., Hu, S., 2002. Determination of forty-two major and trace elements in USGS and NIST SRM glasses by laser ablation-inductively coupled plasma-mass spectrometry. Geostand. Newslett. 26, 181–196.

Garnit, H., Bouhlel, S., Barca, D., Chtara, C., 2012. Application of LA-ICP-MS to sedimentary phosphatic particles from Tunisian phosphorite deposits: insights from trace elements and REE into paleo-depositional environments. Chem. Erde 72, 127–139. https://doi.org/10.1016/j.chemer.2012.02.001.

Garnit, H., Bouhlel, S., Jarvis, I., 2017. Geochemistry and depositional environments of Paleocene–Eocene phosphorites: Metlaoui Group, Tunisia. J. Afr. Earth Sci. 134, 704–736. https://doi.org/10.1016/j.jafrearsci.2017.07.021.

German, C.R., Elderfield, H., 1990. Application of the Ce anomaly as a paleoredox indicator: the ground rules. Paleoceanography 5, 823–833. https://doi.org/10.1029/PA005i005p00823.

Gilinskaya, L.G., 1990. A new type of PO2□ 3 center in apatite. J. Struct. Chem. 31, 892–898. https://doi.org/10.1007/BF00752159.

Gilinskaya, L.G., Tybulewicz, A., 1993. Stable paramagnetic Pb3+ (2 S 1/2) centers in natural Ca5 (PO4)3 (F,Cl,OH) apatites. Phys. Solid State 35, 35–37.

Gilinskaya, L.G., Zanin, Y.N., 1983. EPR study of VO2+ isomorphous admixture in phosphorite apatite. Dokl. Akad. Nauk SSSR 273 (6), 1463–1466.

Gilinskaya, L.G., Zanin, Y.N., Knubovets, R.G., Korneva, T.A., Fadeeva, V.P., 1993. Organophosphorus radicals in natural apatites Ca2(PO4)3(F,OH). J. Struct. Chem. 33, 859–870. https://doi.org/10.1007/BF00745608.

Glenn, R.C., Follmi, K.B., Riggs, S.R., Baturin, G.N., Grimm, K.A., Trappe, J., Abed, A.M., Galli-Olivier, C., Garrison, R.E., Ilyin, A., Jehl, C., Roharlich, V., Sadaqah, R.M., Schidlowski, M., Sheldon, R.E., Siegmund, H., 1994. Phosphorus and phosphorites: sedimentology and environments of formation. Eclogae Geol. Helv. 87, 747–788.

Gnandi, K., Tobschall, H.J., 2003. Distribution patterns of rare-earth elements and uranium in tertiary sedimentary phosphorites of Hahoto´e Kpogam´e, Togo. J. Afr. Earth Sci. 37, 1–10. https://doi.org/10.1016/j.jafrearsci.2003.08.002.

Gong, X.X., Wu, S.W., Xia, Y., Zhang, Z.W., He, S., Xie, Z.J., Xiao, J., Yang, H., Tan, Q., Huang, Y., Yang, Y., 2021. Enrichment characteristics and sources of the critical metal yttrium in Zhijin rare earth-containing phosphorites, Guizhou Province, China. Acta Geochim. 40, 441–465. https://doi.org/10.1007/s11631-021-00460-8.

Grandjean, P., Albaréde, F., 1989. Ion probe measurement of rare earth elements in biogenic phosphates. Geochim. Cosmochim. Acta 53, 3179–3183. https://doi.org/ 10.1016/0016-7037(89)90097-5.

Grandjean-L´ecuyer, P., Feist, R., Albarede, F., 1993. Rare earth elements in old biogenic apatites. Geochem. Cosmochim. Acta 57, 2507–2514. https://doi.org/10.1016/ 0016 7037(93)90413-Q.

Gundogar, D.Y., Sasmaz, A., 2022. Geochemical approach to determine the possible precipitation parameters of the Coniacian–Santonian Mazıda˘gı phosphates, Mardin, Turkey. Minerals 12, 1544. https://doi.org/10.3390/min12121544.

Günther, D., Jackson, S.E., Longerich, H.P., 1999. Laser ablation and arc/spark solid sample introduction into inductively coupled plasma-mass spectrometers. Spectrochim. Acta 54B, 381–409.

Haley, B.A., Klinkhammer, G.P., McManus, J., 2004. Rare earth elements in pore waters of marine sediments. Geochem. Cosmochim. Acta 68 (6), 1265–1279.

He, S., Xia, Y., Xiao, J., Gregory, D., Xie, Z., Tan, Q., Yang, H., Guo, H., Wu, S., Gong, X., 2022. Geochemistry of REY-Enriched Phosphorites in Zhijin Region, Guizhou Province, SW China: Insight into the Origin of REY. Minerals 12 (4), 408. https:// doi.org/10.3390/min12040408.

Henchiri, M., 2007. Sedimentation, depositional environment and diagenesis of Eocene biosiliceous deposits in Gafsa basin (southern Tunisia). J. Afr. Earth Sci. 49, 187–200. https://doi.org/10.1016/j.jafrearsci.2007.09.001.

Hezzi, I., 2014. Caractérisation géophysique de la plateforme de Sahel, Tunisie nordorientale et ses conséquences géodynamiques. Doct. Thesis, 1. Univ. Rennes, France, 316 p.

Holland, H.D. (2006). The oxygenation of the atmosphere and of the oceans. Phil. Trans. R. Soc., 903–915.

Hou, X.Z., Yang, Z.F., Wang, Z.J., 2020. The occurrence characteristics and recovery potential of middle-heavy rare earth elements in the Bayan Obo deposit, Northern China. Ore Geol. Rev. 126, 103737.

Humphries, M., 2010. Rare Earth Elements: The Global Supply Chain. Diane Publishing. Ilyin, A.V., Ratnikova, G.I., 1976. Rare earths distribution in the Hobso Gol phosphorites (Mongolia). Geochem. Int. 13, 53–56.

Jamoussi, F., Abbés, C., Fakhfakh, E., Bédir, M., Kharbachi, S., Soussi, M., Zargouni, F., L´opez-Galindo, A., 2001. Découverte de l'Eocéne continental autour de l'archipel de Kasserine, aux Jebels Rhéouis, Boudinar et Chamsi en Tunisie centro-méridionale: nouvelles implications paléogéographiques. C. R. Acad. Sci. Ser. IIA Earth Planet. Sci. 333, 329–335. https://doi.org/10.1016/S1251-8050(01)01657-3.

Jarvis, I., Burnett, W.C., Nathan, Y., Almbaydin, F.S.M., Attia, A.K.M., Castro, L.N., Flicoteaux, R., Hilmy, M.E., Husain, V., Qutawnah, A.A., Serjani, A., Zanin, Y.N., 1994. Phosphorite geochemistry—state-of-the-art and environmental concerns. Eclogae Geol. Helv. 87, 643–700.

Jasiński, M.. 2020. Identyfikacja podejść do strategii w przedsiębiorstwach w sektorze produktów spo-żywczych FMCG. Ujęcie metodyczne (PhD thesis). Wroclaw: Wroclaw University of Economics and Business

Jiang, S.Y., Zhao, H.X., Chen, Y.Q., 2007. Trace and rare earth element geochemistry of phosphate nodules from the Lower Cambrian black shale sequence in the Mufu mountain of Nanjing, Jiangsu Province, China. Chem. Geol. 244, 584–604. https://doi.org/10.1016/j.chemgeo.2007.07.010.

Joleau, L. (1908) : Sur les faunes de l'Eocène inférieur et moyen du sud Algérien et Tunisien. Bull.soc. géol. France, (4), 8, p. 295 – 297.

Jones, B., Manning, D.A.C., 1994. Comparison of geochemical indices used for the interpretation of palaeoredox conditions in ancient mudstones. Chem. Geol. 111, 111–129. https://doi.org/10.1016/0009-2541(94)90085-X.

Joosu, L., Lepland, A., Kirsimae, K., Romashkin, A.E., Roberts, N.M.W., Martin, A.P., Crne, A.E., 2015. The REE-composition and petrography of apatite in 2 Ga Zaonega Formation, Russia: the environmental setting for phosphogenesis. Chem. Geol. 395, 88–107.

Kadri, A., Essid, E.M., Merzeraud, G., 2015. Kasserine Island" boundaries variations during the Upper Cretaceous-Eocene (central Tunisia). J. Afr. Earth Sci. 111, 244–257. https://doi.org/10.1016/j.jafrearsci.2015.07.027.

Kato, Y., Fujinaga, K., Nakamura, K., Takaya, Y., Kitamura, K., Ohta, J., Toda, R., Nakashima, T., Iwamori, H., 2011. Deep-sea mud in the Pacific Ocean as a potential resource for rare-earth elements. Nat. Geosci. 4, 535–539. https://doi.org/10.1038/ ngeo1185.

Kazakov, A. V. (1930): The phosphate facies: origin of the phosphorites and the geologic factors of formation the deposits. Proc. Sci. Inst. Fertilizers and insectofungicides, 145 p.

Kechiched, R. (2011). Typologie géochimique et géostatistique des minerais de phosphates du gisement de Bled El Hadba – Djebel Onk (Algérie). Université Badji Mokhtar, Annaba. 175p.

Kechiched, R., Laouar, R., Bruguier, O., Salmi-Laouar, S., Ameur-Zaimeche, O., Foufou, A., 2016. Preliminary data of REE in algerian phosphorites: a comparative study and paleo-redox insights. Procedia Eng. 138, 19–29. https://doi.org/10.1016/ j.proeng.2016.02.048.

Kechiched, R., 2017. Les phosphates du nord de tébessa (dyr et elkouif) : étude sédimentologique, gîtologique et géochimique. Thèse de doctorat. Université Badji Mokhtar-Annaba- Algérie. 225 pages.

Kechiched, R., Laouar, R., Bruguier, O., Salmi-Laouar, S., Kocsis, L., Bosch, D., Foufou, A., Ameur-Zaimeche, O., Larit, H., 2018. Glauconite-bearing sedimentary phosphorites from the Tébessa region (eastern Algeria): evidence of REE enrichment and geochemical constraints on their origin. J. Afr. Earth Sci. 145, 190–200. https://doi.org/10.1016/j.jafrearsci.2018.05.018.

Kechiched, R., Laouar, R., Bruguier, O., Kocsis, L., Salmi-Laouar, S., Bosch, D., Ameur-Zaimeche, O., Foufou, A., Larit, H., 2020. Comprehensive REE+Y and sensitive redox trace elements of Algerian phosphorites (T´ebessa, eastern Algeria): a geochemical study and depositional environments tracking. J. Geochem. Explor. 208, 106396 https://doi.org/10.1016/j.gexplo.2019.106396.

Khan, K.F., Dar, S.A., Khan, S.A., 2012. Rare earth element (REE) geochemistry of phosphorites of the Sonrai area of paleoproterozoic Bijawar basin, Uttar Pradesh, India. J. Rare Earths 30, 507–514. https://doi.org/10.1016/S1002-0721(12)60081-7.

Khan, S.A., Khan, K.F., Dar, S.A., 2016. REE geochemistry of early Cambrian phosphorites of Masrana and Kimoi blocks, Uttarakhand, India. Arab. J. Geosci. 9, 1–10. https://doi.org/10.1007/s12517-016-2477-8.

Khater, A.E.M., Galmed, M.A., Nasr, M.M., El-Taher, A., 2016. Uranium and rare earth elements in Hazm El-Jalamid phosphate, Saudi Arabia: concentrations and geochemical patterns comparison. Environ. Earth Sci. 75, 1261. https://doi.org/ 10.1007/s12665-016-6063-x.

Kidder, D., Krishnaswamy, R., Mapes, R.H., 2003. Elemental mobility in phosphatic shales during concretion growth and implication for provenance analysis. Chem. Geol. 198, 335–353. https://doi.org/10.1016/S0009-2541(03)00036-6.

Kocsis, L., Vennemann, T.W., Fontignie, D., 2007. Migration of sharks into freshwater systems during the Miocene and inplications for Alpine paleoelevation. Geology 35, 451–454. https://doi.org/10.1130/G23404A.1.

Kocsis, L., Ounis, A., Baumgartner, C., Pirkenseer, C., Harding, I.C., Adatte, T., Chaabani, F., Mohamed, S., 2014. Paleocene – Eocene palaeoenvironmental conditions of the main phosphorite deposits (Chouabine Formation) in the Gafsa Basin, Tunisia. J. Afr. Earth Sci. 100, 586–597. https://doi.org/10.1016/j. jafrearsci.2014.07.024.

Kocsis, L., Gheerbrant, E., Mouflih, M., Cappetta, H., Ulianov, A., Chiaradia, M., Bardet, N., 2016. Gradual changes in upwelled seawater conditions (redox, pH) from the late Cretaceous through early Paleogene at the northwest coast of Africa: negative Ce anomaly trend recorded in fossil bio-apatite. Chem. Geol. 421, 44-54. https://doi.org/10.1016/j.chemgeo.2015.12.001.

Lacout J-L., 1983. Contribution à l'étude de l'extraction par vapo-métallurgie du manganèse et du vanadium des apatites, Thèse de Doctorat, INP Toulouse (France).

Laffitte, R., 1939. Étude géologique de l'Aurès (Algérie). Bulletin du Service de la Carte Géologique de l'Algérie, 2e série - stratigraphie - descriptions régionales. Univ de Paris., 1939, 484 pages.

Lakehal, C., Ramdhane, M., Boucenna, A., 2010. Natural radionuclide concentrations in two phosphate ores of East Algeria. J. Environ. Radioact. 101 (5), 377–379. https:// doi.org/10.1016/j.jenvrad.2010.02.008.

Larouci M., 1988. Etude de la caractérisation et de la valorisation du minerai de phosphate de Djebel Onk – Algérie- thèse de doctorat ingénieur. Université orléans. 1 vol texte, 194p.

Lehr J.R., MC-Clellan G.H., Smith J.P., Frazier A.W., 1967. Characterization of apatites in commercial phosphate rocks. In Colloque international sur les phosphates minéraux solides. Toulouse, 16-20 février 1967, pp. 29-44.

Li, Y.H., 2000. A Compendium of Geochemistry: From Solar Nebula to the Human Brain. Princeton University Press, Princeton, NJ, p. 475.

Ling, H.F., Chen, X., Li, D., 2013. Cerium anomaly variations in Ediacaran-earliest Cambrian carbonates from the Yangtze Gorges area, South China: implications for oxygenation of coeval shallow seawater. Precambrian Res. 225, 110–127. https://doi.org/10.1016/j.precamres.2011.10.011.

Long, K.R., Van Gosen, B.S., Foley, N.K., Cordier, D., 2010. The Principal Rare Earth Elements Deposits of the United States - A Summary of Domestic Deposits and a Global Perspective (U.S.G.S. Scientific Investigations Report 2010–5220.).

Longerich, H.P., Jackson, S.E., Günther, D., 1996. Laser ablation inductively coupled plasma-mass spectrometric transient signal data acquisition and analyte concentration calculation. J. Anal. At. Spectrom. 11, 899–940.

Lucas, J., Prévôt-Lucas, L., 1996. Tethyan phosphates and bioproductites. In: Nairn, A.E. M., Ricou, L.-E., Vrielynck, B., Dercourt, J. (Eds.), The Tethys Ocean. Springer, Boston, MA, pp. 367–391. https://doi.org/10.1007/978-1-4899-1558-0_12.

Lucas, J., El Faleh, E.M., Prévôt, L., 1990. Experimental study of the substitution of Ca by Sr and Ba in synthetic apatites. In: Notholt, A.J.G., Jarvis, I. (Eds.), Phosphorite Research and Development, 52. Geol. Soc. (Spec. Pub.), London, pp. 33–47. https://doi.org/10.1144/GSL.SP.1990.052.01.04.

McArthur, J.M., 1978. Systematic variations in the contents of Na, Sr, CO_3 and SO_4 in marine carbonate-Fluorapatite and their relation to weathering. Chem. Geol. 21, 89–112. https://doi.org/10.1016/0009-2541(78)90008-6.

McArthur, J.M., 1985. Francolite geochemistry - compositional controls during formation, diagenesis, metamorphism and weathering. Geochim. Cosmochim. Acta 49, 23–35. https://doi.org/10.1016/0016-7037(85)90188-7.

McArthur, J.M., Walsh, J.N., 1984. Rare-earth geochemistry of phosphorites. Chem. Geol. 47, 191–220.

McArthur, J.M., Coleman, M.L., Bremner, J.M., 1980. Carbon and oxygen isotopic composition of structural carbonate in sedimentary francolite. J. Geol. Soc. Lond. 137, 669–673. https://doi.org/10.1016/0016-7037(85)90188-7.

McArthur, J.M., Benmore, R.A., Coleman, M.L., Soldi, C., Yeh, H.W., O'Brien, G.W., 1986. Stable isotopic characterisation of francolite formation. Earth Planet. Sci. Lett. 77, 20–34. https://doi.org/10.1016/0012-821X(86)90129-9.

McKelvey, V.E., 1950. Rare Earths in Western Phosphate Rocks. U.S.G.S., Trace Element Memorandum Report, 6. https://doi.org/10.1016/0012-821X(86)90129-9.

McLennan, S.M., 1989. Rare earth elements in sedimentary rocks: influence of provenance and sedimentary processes. In: Lipin, B.R., McKay, G.A. (Eds.), Geochemistry and Mineralogy of Rare Earth Elements. Rev. Mineral, 21, pp. 169–200.

McLennan, S.M., 1994. Rare earth element geochemistry and the "tetrad" effect. Geochim. Cosmochim. Acta 58, 2025–2033.

McLennan, S.M., Fryer, B.J., Yong, G.M., 1979. The geochemistry of the carbonate-rich Espanola Formation (Horonian) with emphasis on the rare earth elements. Can. J. Earth Sci. 16, 230–239. https://doi.org/10.1139/e79-022.

McRae, S.G., 1972. Glauconite. Earth Sci. Rev. 8, 397–440.

Mezghache H. (1991): Détermination, localisation et estimation globale des différents types de minerai de phosphate dans le gisement de Kef Essennoun – Djebel Onk – Algérie. Rapport E. N. Ferphos, 42 p.

Mezghache H. & Toubal A. Bouima T. & Bouarroudj M.T. (2000): Localisation des différents types de minerai à l'aide de méthodes statistiques multivariables dans le gisement de phosphate de Kef Essennoun – Djebel Onk – Algérie. 5th international conference on the geology of the Arab word. Cairo University, Egypte.

Mezghache H., et Hani A., 2002. Typologie chimique des phosphates du gisement de Djemi-Djema, bassin de Djebel Onk (Algérie orientale). Géologie Méditerranéenne. Tome XXVII n°1/2, pp. 95-106.

Mezghache, H., Toubal, A., Bouima, T., 2004. Typology of phosphate ores in deposits of the Djebel Onk mining basin (eastern Algeria). Phosphorus Res. Bull. 15, 5–20. https://doi.org/10.3363/prb1992.15.0_5.

Michard, A., Albarede, F., Michard, G., Minster, J.F., Charlou, J.L., 1983. Rare-earth elements and uranium in high-temperature solutions from East Pacific rise hydrothermal vent field (13 degree N). Nature 303, 795–797.

Moffett, J.W., 1990. Microbially mediated cerium oxidation in sea water. Nature 345, 421–423. https://doi.org/10.1038/345421a0.

Moffett, J.W., 1994. A radiotracer study of cerium and manganese uptake onto suspended particles in Chesapeake Bay. Geochim. Cosmochim. Acta 58 (2), 695–703. https://doi.org/10.1016/0016-7037(94)90499-5.

Montel G., Bonel G., Trombe J-CH., Heughebaert J-C., Rey Ch., 1980. Progrès dans le domaine de la chimie des composes phosphores solides à structure d'apatite. Application à la biologie et au traitement des minerais. Pure & Appi. Chem., Vol.52, pp. 973-987.

Morad, S., Felitsyn, S., 2001. Identification of primary Ce-anomaly signatures in fossil biogenic apatite: implication for the Cambrian oceanic anoxia and phosphogenesis. Sediment. Geol. 143, 259–264. https://doi.org/10.1016/S0037-0738(01)00093-8.

Nathan, Y., Benalioulhaj, N., Prévôt, L. and Lucas, J. (1996) The geochemistry of cadmium in the phosphate-rich and organic-rich sediments of the Oulad-abdoun and Timahdit basins (Morocco). J. African Earth Sci., 22, 17–27.

Njahi-Derbali, Z., Touir, J., 2019. Sedimentology and sequence stratigraphy of the middle and upper Eocene succession from Jebel Kabbara (central Tunisia). J. Afr. Earth Sci. 160, 103599 https://doi.org/10.1016/j.jafrearsci.2019.103599.

Notholt, A.J.G., 1980. Economic phosphatic sediments: mode of occurrence and stratigraphical distribution. J. Geol. Soc. Lond. 137, 793–805. https://doi.org/10.1144/gsjgs.137.6.0793.

Notholt A.J.G., 1985. Phosphorite resources in the Mediterranean (Tethyan) phosphogenic province: a progress report. In: Phosphorites. Sixth International Field-Workshop and Seminar on Phosphorites. I.G.C.P. 156. Maroc-Sénégal, oct.-nov. 1983. Strasbourg: Institut de Géologie – Université Louis-Pasteur, 1985. pp. 9-17. (Sciences Géologiques. Mémoire, 77).

Notholt, A.J.G., Sheldon, R.P., Davidson, D.F., 1989. Phosphate Deposits of the World, Vol. 2. Cambridge University Press, Cambridge, p. 566.

ORGM, 2012-2014. Rapport final sur les résultats des travaux d'exploration des phosphates du gisement de Bled El-Hadba , p 58.

Ounis, A., Kocsis, L., Chaabani, F., Pfeifer, H.R., 2008. Rare earth elements and stable isotope geochemistry (δ13C and δ18O) of phosphorite deposits in the Gafsa Basin, Tunisia. Palaeogeogr. Palaeoclimatol. Palaeoecol. 268, 1–18. https://doi.org/10.1016/j.palaeo.2008.07.005.

Papineau, D. (2010) Global Biogeochemical Changes at Both Ends of the Proterozoic: Insights from Phosphorites. Astrobiology, 10, 165–181.

Perthuisot, V., 1994. Structures et géométrie des diapirs maghrébins. Essai de synthése. Mém. Serv. Géol. Algérie 6, 153–159.

Pi, D.H., Liu, C.Q., Graham, A., 2013. Trace and rare earth element geochemistry of black shale and kerogen in the Early Cambrian Niutitang Formation in Guizhou province, South China: constraints for redox environments and origin of metal enrichments. Precambrian Res. 225, 218–229. https://doi.org/10.1016/j.precamres.2011.07.004.

Picard, S., Lecuyer, C., Bah'at, J., Garciad, J., Dromart, G., Sheppard, S.M.F., 2002. Rare earth element contents of Jurassic fish and reptile teeth and their potential relation to seawater composition (Anglo-Paris Basin, France and England). Chem. Geol. 186, 1–16. https://doi.org/10.1016/S0009-2541(01)00424-7.

Piper, D.Z., 1994. Seawater as the source of minor elements in black shales, phosphorites and other sedimentary rocks. Chem. Geol. 114, 95–114. https://doi.org/10.1016/0009-2541(94) 90044-2.

Piper, D.Z., 1999. Trace Elements and Major Element Oxides in the Phosphoria Formation at Enoch Valley, Idaho-Permian Sources and Current Reactivities. U.S.G. S. Open-file Report, pp. 99–163.

Prian, J.P., Cortiel, Ph., 1993. Etude de d´eveloppement du gisement de phosphate de Djebel Onk (Alg´erie). Geological expertise report, BRGM-FERPHOS, Tebessa, Algeria, p. 288.

Pufahl, P.K. and Hiatt, E.E. (2012) Oxygenation of the Earth's atmosphere-ocean system: A review of physical and chemical sedimentologic responses. Mar. Pet. Geol. 32:1–20.

Pufahl, P.K. and Groat, L.A. (2017) Sedimentary and igneous phosphate deposits: Formation and exploration: An invited paper. Econ. Geol., 112, 483–516.

Raguin, E., 1961. Geologie des Gites Minéraux. compte-rendu.

Ranchin, G. (1963, a). Les phosphates de chaux sédimentaires de la région de djebel Onk (Algérie).S.E.R.E.M. Paris, 85p.

Ranchin, G. (1963, b). Les phosphates de chaux sédimentaires de la région de Djebel Onk. Étude géologique et minière de Djemi – Djema (Algérie). S.E.R.M. Paris, 2 vol.

Rao, V.P., Michard, A., Naqvi, S.W.A., Bottcher, M.E., Krishnaswamy, R., Thamban, M., Natarajan, R., Borole, D.V., 2002. Quaternary phosphorites of the southeast coast of India. Chem. Geol. 182, 483e502. https://doi.org/10.1016/S0009-2541(01)00336-9.

Reynard, B., L´ecuyer, C., Grandjean, P., 1999. Crystal-chemical controls on rare earth element concentrations in fossil biogenic apatites and implications for paleoenviromental reconstructions. Chem. Geol. 155, 233–241. https://doi.org/10.1016/S0009-2541(98)00169-7.

Rudowicz, I. (1975). Application de la radiométrie aéroportée pour la recherche des phosphates. Rapport SONAREM, Alger.

Samala, W., Khirekesh, Z., Amini, A., Bafti, B.S., 2018. Diagenetic evolution of the upper Devonian phosphorites, Alborz Mountain Range, northern Iran. Sediment. Geol. 376, 90–112. https://doi.org/10.1016/j. sedgeo.2018.08.001.

SAMEC, (1965). Contribution à l'étude des échangeurs d'ions de structure apatitique, Thèse Université. Toulouse.

Sassi, S., 1974. La sedimentation phosphat´ee au Pal´eoc`ene dans le Sud et le Centre-Ouest de la Tunisie. Universit´e Paris Sud Orsay, France, Th`ese Doctorat, p. 292.

Sassi S. (1980): Contexte paléogéographique des dépôts phosphatés en Tunisie – in Géologie comparée des gisements de phosphate et de pétrole. Mém. BRGM, n°116.

Sassi A. B. et Sassis S. (1999) : Le cadmium associé aux dépôts phosphatés en Tunisie méridionale. Journal of African Earth Sciences, Vol. 29, No. 3, pp. 501-513.

Schmidt, K., Koschinsky, A., Garbeschonberg, D., Decarvalho, L., Seifert, R., 2007. Geochemistry of hydrothermal fluids from the ultramafic-hosted Logatchev hydrothermal field, 158N on the Mid-Atlantic Ridge: temporal and spatial investigation. Chem. Geol. 242 (1–2), 1–21. https://doi.org/10.1016/j. chemgeo.2007.01.023.

Seredin, V.V., 2010. A new method for primary evaluation of the outlook for rare earth element ores. Geol. Ore Deposits 52 (5), 428–433.

Shaw, T.J., Gieskes, J.M., Jahnke, R.A., 1990. Early diagenesis in differing depositional environments: the response of transition metals in pore water. Geochim. Cosmochim. Acta 54, 1233–1246. https://doi.org/10.1016/0016-7037(90)90149-F.

Sheldon, R.P., 1987. Association of phosphatic and siliceous marine sedimentary deposits. In: Hein, J.R. (Ed.), Siliceous Sedimentary Rock-hosted Ores and Petroleum. Van Norstrand Reinhold Co, New York, pp. 58–80.

Shields, G., Stille, P., 2001. Diagenetic constraints on the use of cerium anomalies as palaeoseawater redox proxies: an isotopic and REE study of Cambrian phosphorites. Chem. Geol. 175, 29–48. https://doi.org/10.1016/S0009-2541(00)00362-4.

Shields, G., Webb, G., 2004. Has the REE composition of seawater changed over geological time? Chem. Geol. 204 (1–2), 103–107. https://doi.org/10.1016/j. chemgeo.2003.09.010.

Slansky M., 1980. Géologie des phosphates sédimentaires; Mémoire du B.R.G.M ; N°114. France, 92p.

Smirnov V. I,. 1982. Géologie des minéraux utiles. Editions Mir, 1982 - 623 pages.

SO.NA.RE.M (1976 - 1978) : Rapport sur les travaux de prospection et d'évaluation sur les phosphates dans le district minier du Djebel Onk.

Soukeur, A., Szymczyk, A., Berbar, Y., Amara, M., 2021. Extraction of rare earth elements from waste products of phosphate industry. Sep. Purif. Technol. 256, 117857 https://doi.org/10.1016/j.seppur.2020.117857.

Soyol-Erdene, T.-O., Huh, Y., 2013. Rare earth cycling in the pore waters of the Bering Sea Slope (IODP Exp. 323). Chem. Geol. 358, 75–89. https://doi.org/10.1016/j.chemgeo.2013.08.047.

Stalder, M., Rozendaal, A., 2004. Apatite nodules as an indicator of depositional environment and ore genesis for the Mesoproterozoic Broken Hill-type Gamsberg Zn–Pb deposit, Namaqua Province, South Africa. Mineral. Deposita 39 (2), 189–203. https://doi.org/10.1007/s00126-003-0394-8.

Straaten P.V., 2002. Rocks for Corps; Agro Minerals of Sub-Sahara Africa, ICRAF: Nairobi, Kenya, pp 7-24, 338.

Tachikawa, K., Jeandel, C., Vangriesheim, A., Dupr´e, B., 1999. Distribution of rare earth elements and neodymium isotopes in suspended particles of the tropical Atlantic Ocean (EUMELI site). Deep Sea Res. Part 1 Oceanogr. Res. Pap. 46 (5), 733–755.

Tahri, T., Bouzenzana, A., Bezzi, N., 2019. Characterization and homogenization of Bled El-Hadba phosphate ore, case of Djebel Onk (Algeria). Nauk. Visnyk NHU 2, 28–35. https://doi.org/10.29202/nvngu/2019-2/4.

Tanaka, K., Tani, Y., Takahashi, Y., Tanimizu, M., Suzuki, Y., Kozai, N., Ohnuki, T., 2010. A specific Ce oxidation process during sorption of rare earth elements on biogenic Mn oxide produced by Acremonium sp. strain KR21-2. Geochim. Cosmochim. Acta 74 (19), 5463–5477. https://doi.org/10.1016/j.gca.2010.07.010.

Taylor, H., 2001. Inductively Coupled Plasma-Mass Spectrometry Practices and Techniques. Academic Press, San Diego, p. 80.

Taylor, S.R., McLennan, S.M., 1985. Continental Crust: Its Composition and Evolution. Blackwell, Oxford, p. 311.

Tooms, J.S., Summerhayes, C.P., Cronan, D.S., 1969. Geochemistry of marine phosphate and manganese deposits. Oceanogr. Mar. Biol. Annu. Rev. 1, 49–100.

Tostevin, R., Shields, G.A., Tarbuck, G.M., He, T., Clarkson, M.O., Wood, R.A., 2016. Effective use of cerium anomalies as a redox proxy in carbonate-dominated marine settings. Chem. Geol. 438, 146–162. https://doi.org/10.1016/j.chemgeo.2016.06.027.

Turekian, K.K., 1969. The oceans, streams, and atmosphere. In: Wedepohl, K.H. (Ed.), Handbook of Geochemistry, 1. Springer, Heidelberg Berlin, pp. 297–323.

U.S.G.S (2020). Mineral Commodity Summaries 2020: U.S. Geological Survey, 200 p. https://doi.org/10.3133/mcs2020 (Accessed date: 11/12/ 2021).

Valetich, M., Zivak, D., Spandler, C., Degeling, H., Grigorescu, M., 2022. REE enrichment of phosphorites: an example of the Cambrian Georgina Basin of Australia. Chem. Geol. 588, 120654 https://doi.org/10.1016/j.chemgeo.2021.120654.

Van Achterberg, E., Ryan, C.G., Jackson, S.E., Griffin, W., 2001. Data reduction software for LA-ICP-MS. In: Sylvester, P. (Ed.), Laser Ablation ICP-MS in the Earth Science, vol. 29. Mineralogical Association of Canada, pp. 239–243.

Visse, L. (1951). Le gisement de phosphate de chaux de Djebel Onk. Rapport interne Soc. Dj. Onk, 152 p, 32 pl., 10 pl. h.t.

Visse, L., 1952. Genesis of the southeasterly Algerian-Tunisian phosphatic deposits. In: XIX International Geological Congress, Set 1 (27). Algeria, Algiers, 60 p.

Wang, J., Guo, M., Liu, M., Wei, X., 2020. Long-term outlook for global rare earth production. Res. Policy 65, 101569. https://doi.org/10.1016/j.resourpol.2019.101569.

Wang, L., Huang, X., Yu, Y., Zhao, L., Wang, C., Feng, Z., Cui, D., Long, Z., 2017. Towards cleaner production of rare earth elements from bastnaesite in China. J. Clean. Prod. 165, 231–242.

Winnock, E., 1980. Les dépots de l'Eocène au Nord de l'Afrique: aperçu paléogéographique de l'ensemble. In: Géologie comparée des gisements de phosphates et de pétrole, Colloque International, Orléans, Document du BRGM, N◦24, pp. 219–243.

Wright, 1969. Contribution à l'étude de l'influence des substitutions cationiques sur les propriétés d'échangeurs d'ions des apatites, Thèse Doctorat, Univ. Toulouse.

Wright, J., Seymour, R.S., Shaw, H.F., 1984. REE and Nd isotopes in conodont apatite: variations with geological age and depositional environment. In: Clark, D.L. (Ed.), Conodont Biofacies and Provincialism, 196. Geol. Soc. Amer. Spec. Paper, pp. 325–340. https://doi.org/10.1130/SPE196-p325.

Wright, J., Schrader, H., Holser, W.T., 1987. Paleoredox variations in ancient oceans recorded by rare earth elements in fossil apatite. Geochim. Cosmochim. Acta 51, 631–644. https://doi.org/10.1016/0016-7037(87)90075-5.

Xiao, Y., Feng, Z., Huang, X., Huang, L., Chen, Y., Liu, X., Wang, L., Long, Z., 2016. Recovery of rare earth from the ion-adsorption type rare earths ore: II. Compound leaching. Hydrometallurgy 163, 83–90.

Xin, H., Jiang, S., Yang, J., Wu, H., Pi, D., 2016. Rare earth element geochemistry of phosphatic rocks in Neoproterozoic Ediacaran Doushantuo Formation in hushan section from the Yangtze Gorges area, South China. J. Earth Sci. 27, 204–210. https://doi.org/10.1007/s12583-015-0653-5.

Younes, H., Mahanna, H., El-Etriby, H.K., 2019. Fast adsorption of phosphate (PO_4^{3+}) from wastewater using glauconite. Water Sci. Technol. 80, 1643–1653. https://doi.org/10.2166/wst.2019.410.

Zaïer, A., B´eji-Sassi, A., Sassi, S., Moody, R.T.J., 1998. Basin evolution and deposition during the early Paleocene in Tunisia. In: Macgregor, D.S., Moody, R.T.J., Clark- Lowes, D.D. (Eds.), Petroleum Geology of North Africa, 132. Geol. Soc. London Spec. Publ., pp. 375–393. https://doi.org/10.1144/GSL.SP.1998.132.01.21

Zhang, J., Amakawa, H., Nosaky, Y., 1994. The comparative behavior of Y and lanthanides in seawater on the North Pacific. Geophys. Res. Lett. 21, 2677–2680. https://doi.org/10.1029/94GL02404.

Zhang, S.H., Zhao, Y., Liu, Y., 2017. A precise zircon Th-Pb age of carbonatite sills from the world's largest Bayan Obo deposit: Implications for timing and genesis of REE-Nb mineralization. Precambrian Res. 291, 202–219.

Zhu, B., Jiang, S.Y., 2017. A LA-ICP-MS analysis of rare earth elements on phosphatic grains of the Ediacaran Doushantuo phosphorite at Weng'an, South China: implication for depositional conditions and diagenetic processes. Geol. Mag. 154, 1381–1397. https://doi.org/10.1017/S001675681700022X.

Zhu, B., Jiang, S.Y., Yang, J.H., 2014. Rare earth element and Sr-Nd isotope geochemistry of phosphate nodules from the Lower Cambrian Niutitang Formation, NW Hunan province, South China. Palaeogeogr. Palaeoclimatol. Palaeoecl. 398, 132–143. https://doi.org/10.1016/j.palaeo.2013.10.002.

Zouaghi, T., Bédir, M., Inoubli, M.H., 2005. Structuration profonde des dépots de l'Albien-Maastrichtien en Tunisie centrale : nouvelle limite de l'archipel de Kasserine et implications géodynamiques. C. R. Geosci. 337, 685–693. https://doi.org/10.1016/j.crte.2005.02.006.